Turbulent transport in rotating tokamak plasmas

by

Francis James Casson

Thesis

Submitted to the University of Warwick

for the degree of

Doctor of Philosophy

Department of Physics

March 2011

THE UNIVERSITY OF
WARWICK

Contents

Acknowledgments

The greatest share of the thanks must go to my supervisor Arthur Peeters, whose guidance has been indispensable throughout the work of this thesis. His ideas, insight, and humour have always been dispensed in a timely and encouraging manner, whilst his scientific ability and integrity have been a model to aspire to.

The development of the GKW code has been a team effort, which I have enjoyed being a part of. I have benefited a huge amount from interaction with the other team members Yann Camenen, Will Hornsby, Andrew Snodin and Gabor Szepesi, both as friends and colleagues. The same applies to Walter Guttenfelder (occasionally on loan to the team), who deserves additional thanks for his contribution to Chapter 4. I have also profited from useful discussions with C. Angioni, C. S. Brady, W. Dorland, P. deVries, A. R. Field, G. W. Hammett, P. Hill, K. G. McKlements, C. M. Roach, A. A. Schekochihin and B. D. Scott; this list is by no means exhaustive.

This work was made possible by financial support from EPSRC and CCFE. Simulations were performed using the resources of the CSC at Warwick, the HPC-FF machine in Jülich, and the HECTOR national resource.

Outside academia, I owe a large debt to my parents and siblings for their unreserved love and support throughout my education. I am grateful to my friends Thomas and Tim for showing enough interest in this thesis to proof read some parts. I also want to thank Sir Hugh Munro, and all my friends at Warwick and elsewhere, for giving me a life beyond work. A special thanks is reserved for Catherine for her companionship, which has helped me to keep some sanity over the last three years.

This thesis was typeset by the author using LaTeX 2ε, BibTeX, and Zotero on GNU/Linux.
Figures were created by the author using Matlab, OpenOffice.org Draw, and VisIt.

Declaration

I declare that the work presented in this thesis is my own except where stated otherwise, and was carried out at the University of Warwick during the period of October 2007 to March 2011, under the supervision of Prof. A.G. Peeters.

The research reported here has not been submitted, either wholly or in part, at this or any other academic institution for admission to a higher degree. Some parts of the work reported in this thesis have been published in peer reviewed journals, as listed below:

1. F. J. Casson, A. G. Peeters, C. Angioni, Y. Camenen, W. A. Hornsby, A. P. Snodin, and G. Szepesi. *Gyrokinetic simulations including the centrifugal force in a rotating tokamak plasma.* Phys. Plasmas, **17**, 102305, (2010).
2. A. G. Peeters, Y. Camenen, F. J. Casson, W. A. Hornsby, A. P. Snodin, D. Strintzi, and G. Szepesi. *The nonlinear gyro-kinetic flux tube code GKW.* Comp. Phys. Commun. **180**, 2650, (2009).
3. F. J. Casson, A. G. Peeters, Y. Camenen, W. A. Hornsby, A. P. Snodin, D. Strintzi, and G. Szepesi. *Anomalous parallel momentum transport due to ExB flow shear in a tokamak plasma.* Phys. Plasmas **16**, 092303, (2009).
4. A. G. Peeters, D. Strintzi, Y. Camenen, C. Angioni, F. J. Casson, W. A. Hornsby, and A. P. Snodin. *Influence of the centrifugal force and parallel dynamics on the toroidal momentum transport due to small scale turbulence in a tokamak.* Phys. Plasmas, **16**, 042310, (2009).

Publication 1 in the above list is the basis of some of Chapter 2 of this thesis, and most of Chapter 6. Publication 2 is the basis of Chapter 3, and I explicitly acknowledge that I am not the primary author of this material. The individual sections of Chapter 3 to which I am not primary author are made explicit at the start of that chapter. Publication 3 in the above list is the basis of Chapter 6. Some parts of publication 4 are used in Chapter 2. Figures 1.1, 1.6 and 4.11 were not created by me and are used with permission, with attribution indicated in the captions.

Other related work not reported in detail this thesis has been published in peer reviewed journals, as listed below:

1. A. G. Peeters, C. Angioni, Y. Camenen, F. J. Casson, W. A. Hornsby, A. P. Snodin, and D. Strintzi. *The influence of the self-consistent mode structure on the Coriolis pinch effect.* Phys. Plasmas, **16**, 062311, (2009).
2. C. M. Roach, I. G. Abel, R. J. Akers, W. Arter, M. Barnes, Y. Camenen, F. J. Casson, G. Colyer, J. W. Connor, S. C. Cowley, D. Dickinson, W. Dorland, A. R. Field, W. Guttenfelder, R. J. Hastie, E. Highcock, N. F. Loureiro, A. G. Peeters, M. Reshko, S. Saarelma, A. Schekochihin, M. Valovic, and H. R. Wilson. *Gyrokinetic simulations of Spherical Tokamaks.* Plasma Phys. Control. Fusion **51**, 124020, (2009).
3. Y. Camenen, A. G. Peeters, C. Angioni, F. J. Casson, W. A. Hornsby, A. P. Snodin, and D. Strintzi. *Transport of Parallel Momentum Induced by Current-Symmetry Breaking in Toroidal Plasmas.* Phys. Rev. Lett., **102**, 125001, (2009).
4. Y. Camenen, A. G. Peeters, C. Angioni, F. J. Casson, W. A. Hornsby, A. P. Snodin, and D. Strintzi. *Intrinsic rotation driven by the electrostatic turbulence in up-down asymmetric toroidal plasmas.* Phys. Plasmas, **16**, 062501, (2009).
5. Y. Camenen, A. G. Peeters, C. Angioni, F. J. Casson, W. A. Hornsby, A. P. Snodin, and D. Strintzi. *Impact of the background toroidal rotation on particle and heat turbulent transport in tokamak plasmas.* Phys. Plasmas, **16**, 012503, (2009).
6. Y. Camenen, A. Bortolon, B.P. Duval, L. Federspiel, A.G. Peeters, F. J. Casson, W.A. Hornsby, A.N. Karpushov, F. Piras, O. Sauter, A. P. Snodin, G. Szepesi and the TCV Team, *Experimental demonstration of an up-down asymmetry effect on intrinsic rotation in the TCV tokamak.* Plasma Phys. Control. Fusion, **52** 124037, (2010).
7. Y. Camenen, A. Bortolon, B. P. Duval, L. Federspiel, A. G. Peeters, F. J. Casson, W. A. Hornsby, A. N. Karpushov, F. Piras, O. Sauter, A. P. Snodin, and G. Szepesi. *Experimental evidence of momentum transport induced by an up-down asymmetric magnetic equilibrium in toroidal plasmas.* Phys. Rev. Lett., **105**, 135003, (2010).
8. W. A. Hornsby, A. G. Peeters, A. P.Snodin, F. J. Casson, Y. Camenen, G. Szepesi, M. Siccinio, and E. Poli. *The nonlinear coupling between gyroradius scale turbulence and mesoscale magnetic islands in fusion plasmas.* Phys. Plasmas, **17**, 092301, (2010).
9. W. A. Hornsby, A. G. Peeters, E. Poli, M. Siccinio, A. P. Snodin, F. J. Casson, Y. Camenen, and G. Szepesi. *On the nonlinear coupling between micro turbulence and mesoscale magnetic islands in a plasma.* Europhysics Lett, **91**, 45001, (2010).
10. W. A. Hornsby, M. Siccinio, A. G. Peeters, E. Poli, A. P. Snodin, F. J. Casson, Y. Camenen, G. Szepesi, *Interaction of turbulence with magnetic islands: Effect on bootstrap current.* Plasma Phys. Control. Fusion, **53**, 054008, (2011).
11. A. G. Peeters, C. Angioni, A. Bortolon, Y. Camenen, F. J. Casson, B. Duval, L. Fiederspiel, W. A. Hornsby, Y. Idomura, N. Kluy, P. Mantica, F. I. Parra, A.P. Snodin, G. Szepesi, D. Strintzi, T. Tala, G. Tardini, P. de Vries, J. Weiland *Overview of anomalous toroidal momentum transport.* Nuc. Fusion, submitted, (2011).

Abstract

Small scale turbulence in a magnetically confined fusion plasma drives energy and particle transport which determine the confinement. The plasma in a tokamak experiment has a toroidal rotation which may be driven externally, but can also arise spontaneously from turbulent momentum transport. This thesis investigates the interaction between turbulence and rotation via nonlinear numerical simulations, which use the gyrokinetic description in the frame that corotates with the plasma. A local gyrokinetic code is extended to include both the centrifugal force, and the stabilising effect of sheared equilibrium flow.

Sheared flow perpendicular to the magnetic field suppresses the turbulence, and also breaks a symmetry of the local model. The resulting asymmetry creates a turbulent residual stress which can counteract diffusive momentum transport and contribute to spontaneous rotation. The competition between symmetry breaking and turbulence suppression results in a maximum in the nondiffusive momentum flux at intermediate shearing rates. Whilst this component of the momentum transport is driven by the sheared flow, it is also found to be suppressed by the shearing more strongly than the thermal transport. The direction of the residual stress reverses for negative magnetic shear, but also persists at zero magnetic shear.

The parallel component of the centrifugal force traps particles on the outboard side of the plasma, which destabilises trapped particle driven modes. The perpendicular component of the centrifugal force appears as a centrifugal drift which modifies the phase relation between density and electric field perturbations, and is stabilising for both electron and ion driven instabilities. For ion temperature gradient dominated turbulence, an increased fraction of slow trapped electrons enhances the convective particle pinch, suggesting increased density peaking for strongly rotating plasmas. Heavy impurities feel the centrifugal force more strongly, therefore the effects of rotation are significant for impurities even when the bulk ion Mach number is low. For ion driven modes, rotation results in a strong impurity convection inward, whilst a more moderate convection outward is found for electron driven modes.

Chapter 1

Introduction

1.1 Motivation

In today's global geopolitical and environmental context, the prospect of unlimited clean energy promised by fusion power seems more urgent than ever. This hope has motivated physicists in over sixty years of research, resulting in substantial and impressive progress, but not yet the final goal.

The most accessible fusion reactions occurs when a plasma of deuterium and tritium fuel is heated to ultra-high temperatures. Achieving the energy confinement necessary for these nuclear reactions presents many scientific and technical challenges, and a number of different approaches have been explored. Confining the plasma using magnetic fields has proved a promising approach, since it creates the possibility of continuous fusion power. The tokamak is the leading concept for a magnetic confinement device, and has produced the best confinement to date.

Since the first tokamak experiments over fifty years ago, great progress has been made in controlling, heating, diagnosing and understanding the plasma; temperatures hotter than the core of the Sun have been achieved, and fusion reactions have been demonstrated [1]. The next stage tokamak, named ITER[1], is a grand international project that plans to demonstrate the scientific and technical feasibility of a fusion reactor on the scale needed for a commercial powerplant; it aims, for the first time, to produce sustained fusion power ten times greater than the input power. If successful, knowledge gained from ITER will be used to build the first demonstration fusion powerplant.

The magnetic field in a tokamak holds the plasma in a quasi-equilibrium subject to a zoo of plasma instabilities over a large range of spatial and temporal scales. Macroscale instabilities can cause a complete loss of plasma control, whilst small

---

[1] ITER stands for International Thermonuclear Experimental Reactor, but the Latin meaning "The way" (or "journey") is now often used in place of the acronym.

scale instabilities drive turbulent transport of energy out from the core, degrading confinement. Early research focused on avoiding the large scale instabilities, leading to an understanding of the operational limits set by them. With this knowledge came the ability to avoid large scale disruptions and an effective mastery which now allows efforts to be focused on minimising the undesirable small scale microturbulence. The plasma physics describing tokamak microturbulence is nonlinear and highly complex, with a high dimensionality that makes numerical modelling a formidable challenge. Despite these difficulties, the development of a gyrokinetic description, coupled with computational advances has made simulations of these phenomena increasingly tractable in the last two decades.

Plasma rotation is known to play an important role in quenching transport through the stabilisation of turbulence. In particular, it is believed that sheared flows allow the formation of transport barriers responsible for higher confinement operating regimes (H-mode). It is also becoming clear that turbulence and rotation co-exist in a symbiotic relationship, with interactions in both directions allowing the formation of feedback loops. In recent years, the observation of spontaneous plasma rotation in the absence of an external torque has led to a focus on the mechanisms by which the turbulence can transport plasma angular momentum. Thus, the understanding of the interaction between equilibrium plasma flow and microturbulence is progressing on two fronts: *First*, the effect of rotation on turbulent transport, and *second*, the effect of turbulence on the rotation.

This thesis details advances in our understanding in both of the above categories: We describe the extension of the gyrokinetic model to the case of strongly rotating plasmas, namely through the inclusion of the centrifugal force. Using this extension, we examine the effect of strong rotation on turbulent transport of heat and particles. We also examine the effect of sheared flow on angular momentum transport, a case which falls into both categories, since the angular momentum transport will itself play a part in setting the sheared flow.

Clearly, the two categories delineated above cannot be considered in isolation in a self consistent description of plasma transport. This thesis addresses pieces of the puzzle that will be needed if they are to be unified in a comprehensive description of plasma transport and rotation. Understanding and controlling the processes of rotation and transport in future fusion reactors will allow optimisation which will contribute to their eventual viability.

The remainder of this chapter introduces the fundamental concepts necessary to understand this thesis. An emphasis is placed on intuitive physical descriptions over detailed mathematical formalism (which is developed in later chapters).

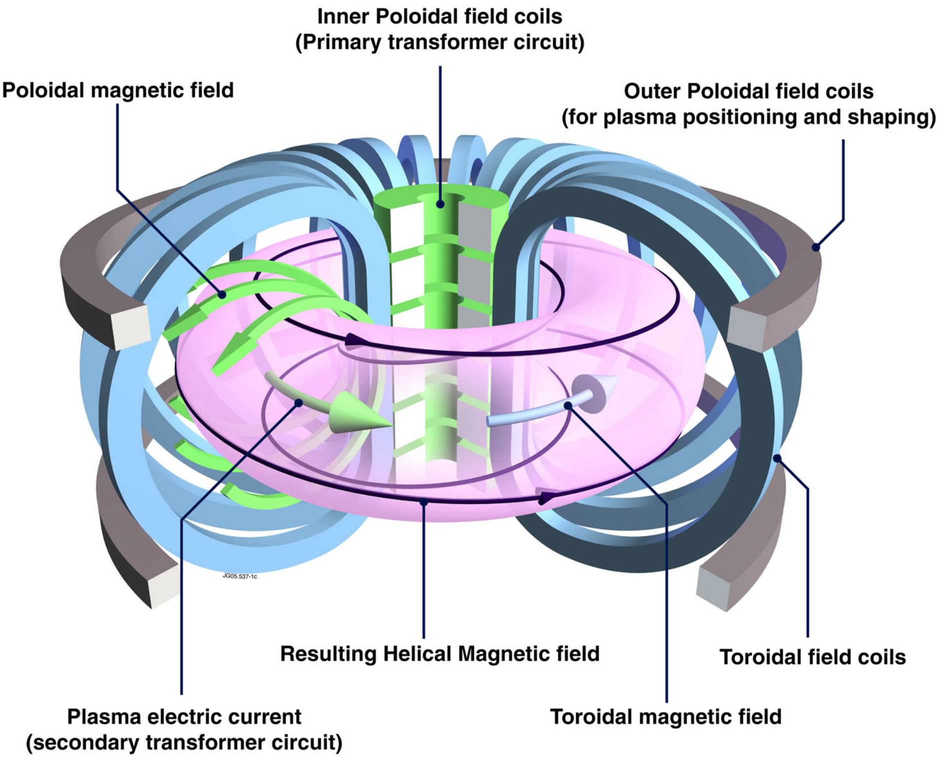

Figure 1.1: Schematic diagram of a tokamak, showing the origin of the toroidal and poloidal magnetic fields. The toroidal direction is the long way around the torus and the poloidal direction is the short way around. The toroidal magnetic field is imposed by external toroidal field coils (blue). The poloidal magnetic field is produced by an inductive transformer (green): A constantly increasing magnetic flux through the primary circuit drives a toroidal current in the plasma, which forms the secondary circuit. Image: EFDA-JET [2].

1.2 Tokamak equilibrium

In a tokamak, the plasma is confined in a torus, with a toroidal magnetic field imposed by external coils (Fig. 1.1). The plasma and the fields are symmetric to any rotation about the central axis of the torus, a property known as 'toroidal axisymmetry'. The solution of Ampere's law for a toroidal solenoid dictates that this toroidal magnetic field must have a radial variation $B \sim 1/R$ (where R is the major radial coordinate of the torus). A consequence of the gradient and curvature of the toroidal magnetic field is that no equilibrium can exist without an additional poloidal magnetic field. The poloidal field in a tokamak is provided by driving a toroidal current in the plasma, primarily induced from the changing magnetic field of a central solenoid. The superposition of the poloidal and toroidal fields results in helical magnetic field lines that wind around the torus, mapping out nested toroidal

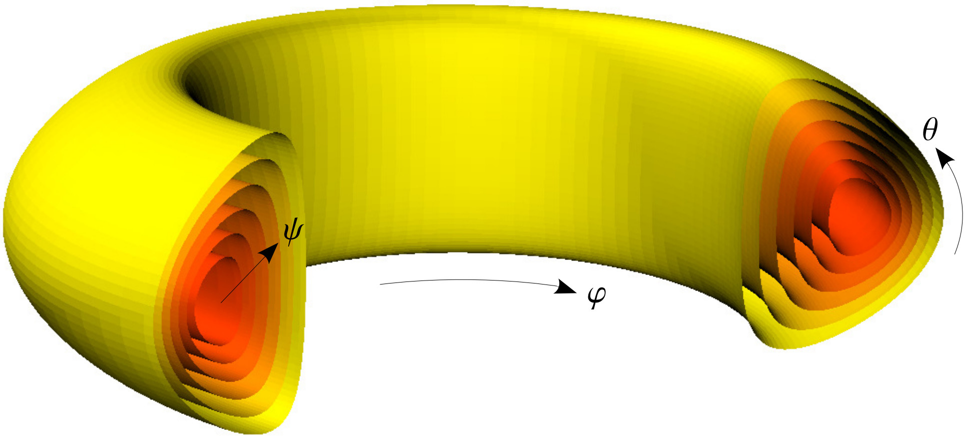

Figure 1.2: Illustration of the nested toroidal flux surfaces in a tokamak, indicating toroidal (φ) and poloidal (θ) angles and flux surface label (ψ), which form a generalised toroidal coordinate system.

surfaces, known as 'flux surfaces' (Fig. 1.2).

Inductive current drive is the simplest way to drive the toroidal current, but inherently limits the tokamak to pulsed operation, since the current in central solenoid cannot keep increasing indefinitely. The use of additional non-inductive methods of current drive can extend the pulse length, and in some highly optimised scenarios can enable the tokamak to achieve a steady state.

The plasma is held in equilibrium by the balance of the pressure force (∇p), centrifugal force, and the Lorentz force ($\mathbf{J} \times \mathbf{B}$), which in terms of magnetohydrodynamics (MHD, in which the plasma is considered as a conducting fluid) is written as [3]

$$\mathbf{J} \times \mathbf{B} = \nabla p + \varrho(\mathbf{u} \cdot \nabla)\mathbf{u}, \tag{1.1}$$

where $\mathbf{J}$ is the current density vector, ϱ is the mass density and $\mathbf{u}$ is the plasma fluid velocity. The second term on the right hand side is often neglected, since it only becomes important for strongly rotating plasmas with Mach numbers approaching unity. Neglecting the second term in the limit of low Mach number, it is clear that $\mathbf{B} \cdot \nabla p = 0$, with the result that the flux surfaces must be surfaces of constant pressure. Furthermore, $\mathbf{J} \cdot \nabla p = 0$, indicating that current must also lie in the flux surfaces defined by the magnetic field lines. The fast thermal motion of particles over the flux surfaces ensures that equilibrium (thermalised) plasma quantities (temperature T, angular velocity ω_φ, density n) are constant on a flux surface, such that the equilibrium is toroidally axisymmetric.

These ‘flux functions’ may be conveniently parametrised by a single quantity ψ which uniquely labels the flux surfaces. In a simplified equilibrium model with circular flux surfaces, the minor radius r may be used as a flux surface label, but for non circular flux surfaces a flux surface label is used as a generalised ‘minor radial’ coordinate[2] (Fig. 1.2). In this thesis, the radial coordinate is a geometric distance $\psi = (R_{\max} - R_{\min})/2R_A$ which corresponds to the minor radius in simplified geometries and scales with the square root of the poloidal flux ($\psi \sim \sqrt{\Psi_p}$).

In the generalisation to the strongly rotating case [4], the temperature and angular velocity remain flux functions, but the density and pressure vary over a flux surface (discussed further in Chapter 2). The surfaces of constant pressure and density do not depart very far from the flux surfaces, except for the density of heavy impurity ions [5].

The helicity of a magnetic field line is measured by the ‘safety factor’ $q(\psi)$, the number of toroidal turns for each poloidal turn, while its radial derivative is described by the ‘magnetic shear’ $\hat{s}(\psi) = (\psi/q)\mathrm{d}q/\mathrm{d}\psi$. The safety factor must be greater than one in order to avoid macroscale instabilities (kink mode), although in practice q may drop slightly below one in the core, since internal kink modes (sawteeth) can be tolerated and managed effectively. The q profile is determined by the current profile, which for a typical plasma results in $\hat{s} > 0$, with $q \sim 3 - 5$ just inside the last closed flux surface[3], decreasing to $q \sim 1$ at the plasma core.

The dimensionless ratio of the kinetic plasma pressure $p = nT$ and the magnetic field pressure $B^2/2\mu_0$,

$$\beta = \frac{p_{\text{central}}}{B_{\text{coil}}^2/2\mu_0}, \tag{1.2}$$

parametrises the efficiency of the magnetic field in confining the plasma. Here, B_{coil} is the vacuum toroidal field at the coil. A plasma with $\beta > 1$ cannot be confined by a magnetic field, since the kinetic pressure is not balanced by the magnetic pressure. In a conventional tokamak, however, it is the poloidal field B_p that is responsible for most the confinement (in Eq. (1.1), $|B_p J_t| > |B_t J_p|$), with the much larger toroidal field B_t required for stabilisation of the current driven kink instability. Since $B_t \gg B_p$, the plasma beta in a typical tokamak is only a few percent [$\beta \sim 0.01$][4], though it can reach up to 30% in some spherical devices.

---

[2] The poloidal magnetic flux Ψ_p through any toroidal loop in the surface is a constant value which for a monotonic current profile is unique to each flux surface and can be used as flux surface label.

[3] At the edge of the plasma, the magnetic field intersects a solid surface directly or has a magnetic separatrix. Beyond this point the flux surfaces are not closed.

[4] Throughout this thesis numbers in square brackets indicate approximate values of physical quantities for an ITER core deuterium plasma with $T = 10keV, n = 10^{20}m^{-3}, B = 5.2T, R = 6m, a = 2m$. Temperature is always expressed as an energy, i.e. $T = k_B T_{\text{Kelvin}}$. A full list of symbols and notation appears at the end.

1.3 Single particle motion

In a tokamak plasma, the equilibrium fields vary on length scales large compared to the ion-cyclotron (Larmor) gyroradius $\rho_i = m_i v_{\mathrm{th}}/ZeB \sim [4mm]$, and slowly compared to the ion-cyclotron frequency $\omega_{ci} \equiv eB/m_i \sim [250\mathrm{MHz}]$. Fluctuations on the equilibrium fields are small, which allows single particle motion to be accurately decomposed into the fast cyclotron rotation around the magnetic field line, and a slower motion of its guiding centre. In this model, each particle acts as a gyroscope with conserved magnetic moment $\mu = mv_\perp^2/2B$, such that a general force $\mathbf{F}$ acting on it will cause the gyrocentre to drift in a direction perpendicular to the magnetic field with velocity

$$\mathbf{v}_{\mathrm{D}} = \frac{\mathbf{F} \times \mathbf{b}}{ZeB}, \tag{1.3}$$

where $\mathbf{b}$ is the unit vector in the direction of the magnetic field. In a tokamak, the largest drifts in the guiding centre position $\mathbf{X}$ are due to the curvature of the magnetic field and the presence of electric fields. The drifts due to the curvature of the magnetic field have the form[5]

$$\mathbf{v}_d = \frac{1}{ZeB}\left[mv_\parallel^2 \mathbf{b} \times (\mathbf{b} \cdot \nabla)\mathbf{b} + \mu \mathbf{b} \times \nabla B\right]. \tag{1.4}$$

The term proportional to $v_\parallel^2$ is caused directly by the curvature of magnetic field, which causes a centrifugal force on an individual particle as it follows the field curvature. The term proportional to μ is caused by the magnetic field gradient which is a consequence of the curvature: The gradient causes a net imbalance in the Lorentz force over the course of a gyro-orbit, which is expressed as the magnetic gradient force $\mathbf{F} = -\mu \nabla B$.

The presence of an electric field results in the $E\times B$ drift

$$\mathbf{v}_E = \frac{\mathbf{E} \times \mathbf{b}}{B}, \tag{1.5}$$

which is due to the electrostatic force. Unlike the other drifts, the $E\times B$ drift has the same magnitude and direction for both ions and electrons and thus does not promote charge separation. In addition, if the electric field is time varying, a correction to the $E\times B$ drift over the course of a cyclotron orbit results in the polarisation drift

$$\mathbf{v}_p = \frac{m}{eB^2}\frac{d\mathbf{E}}{dt}. \tag{1.6}$$

---

[5] In the low beta limit the approximation $\mathbf{b} \times (\mathbf{b} \cdot \nabla)\mathbf{b} \approx \mathbf{b} \times \nabla B/B$ may also be used.

The complete guiding centre velocity is then given by

$$\frac{\mathrm{d}\mathbf{X}}{\mathrm{d}t} = v_\parallel \mathbf{b} + \mathbf{v}_d + \mathbf{v}_E + \mathbf{v}_p. \tag{1.7}$$

A consequence of the assumptions made about the field gradients is the result that the drift velocities are small as compared to the thermal v_{th} and parallel velocities. This idea is central to the guiding centre description, and can be formalised by the small parameter $\rho_* = \rho_i/R \ll 1$ with $v_D \sim \rho_* v_{\mathrm{th}}$. In Chapter 2, ρ_* and other small parameters will be further examined, quantified and utilised in the construction of the gyrokinetic model of the plasma dynamics, with the guiding centre description as its basis.

The conservation of the magnetic moment μ (also known as the first adiabatic invariant), together with the conservation of kinetic energy $(m/2)(v_\parallel^2 + v_\perp^2)$, means that as a particle moves to a region of higher magnetic field, its perpendicular velocity increases and its parallel velocity decreases. The force responsible for the parallel deceleration is the parallel component of the magnetic gradient force $\mathbf{F} = -\mu\nabla B$, often termed the 'mirror force' due to its ability to reflect particles with small parallel velocity. These particles, which bounce in the region of high magnetic field are termed 'trapped particles', whilst those possessing enough parallel velocity to not bounce are termed 'passing particles'. A trapping condition can be derived from energy conservation for particles on the limit between trapped and passing

$$\mu B_H = \frac{1}{2} m v_{\parallel,L}^2 + \mu B_L, \tag{1.8}$$

where the H and L subscripts denote values at the points of highest and lowest magnetic field respectively. In a tokamak with circular flux surfaces, $B \sim 1/R$ with the highest and lowest magnetic fields occurring at $R = R_A - r$ and $R = R_A + r$ respectively, where R_A is the major radius of the magnetic axis[6]. The energy conservation equation can then be rearranged to show that particles are trapped if their velocity satisfies

$$v_\perp^2 > \left(\frac{1-\epsilon}{2\epsilon}\right) v_\parallel^2, \tag{1.9}$$

where $\epsilon = r/R_A$ is the inverse aspect ratio of the flux surface. In Chapter 2 we return to this trapping condition, and show how it is modified by the centrifugal force in a strongly rotating plasma.

---

[6] The magnetic axis defines the core of the tokamak, it is the innermost flux "surface" which is a single toroidal field line.

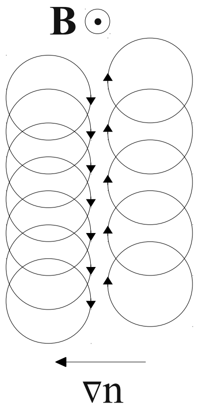

Figure 1.3: Diamagnetic velocity of ions in the presence of a density gradient.

1.4 Plasma diamagnetism

Magnetised plasma is naturally diamagnetic, since the magnetic moment generated by each particle executing cyclotron motion is oriented to oppose the applied magnetic field. In a plasma with a density gradient, greater plasma magnetisation in regions of higher density limits the penetration of an external magnetic field (and sets the theoretical upper limit of $\beta = 1$). The presence of a density gradient results in a collective fluid velocity for each species

$$\mathbf{v}_{\mathrm{dia}} = \frac{\mathbf{b} \times \nabla p}{Zen_0 B} \qquad \sim [100ms^{-1}]. \tag{1.10}$$

This diamagnetic velocity can be understood by reference to Fig. 1.3, in which it can be seen that the net imbalance of ions moving upwards and downwards results in an average motion downwards due to the density gradient. Since the diamagnetic motion of the ions and electrons is in opposite directions, a perpendicular (mostly poloidal) diamagnetic current results, creating the induced magnetic field which opposes the applied field.[7] The diamagnetic velocity is a collective plasma motion resulting from the gyro-motion and should not be confused with the guiding centre picture for single particles described above. The equilibrium fluid motion of a single plasma species can be written as

$$\mathbf{v}_{\mathrm{fluid}} = \mathbf{v}_{\mathrm{dia}} + \mathbf{v}_E + \mathbf{v}_d. \tag{1.11}$$

---

[7] A low beta tokamak can also be paramagnetic if the poloidal field pressure exceeds the kinetic pressure, because the poloidal part of the inductive current reinforces the toroidal field.

1.5 Plasma drift waves

Since the early tokamak experiments it has been clear that the energy and particle confinement times achieved are generally worse by an order of magnitude than those predicted by neoclassical theory (collisional transport in toroidal geometry). This transport, historically termed ‘anomalous transport’, is now widely believed to be a result of ‘drift wave’ microturbulence driven by the energy and temperature gradients in the plasma. Here we introduce only some fundamental properties of drift waves; for a complete discussion see Ref. [6].

Drift waves are modes of collective plasma oscillation that arise in magnetised plasmas, as a consequence of disparate electron and ion dynamics. These independent dynamics interact through the electrostatic force, conspiring to ensure that plasma ‘quasineutrality’ is always maintained. The concept of quasineutrality is fundamental to understanding the drift wave (and plasmas in general), and gives rise to a rich variety of complex behaviour, including many types of drift wave.

Quasineutrality expresses the idea that whilst ions and electrons in a plasma are free to move independently, any large scale separation of charge is prevented by the huge electric fields that would occur if this were to happen. At the smallest spatial or temporal scales, however, charge imbalance can occur. The limits beyond which quasineutrality must be satisfied are characterised by: a) The Debye length $\lambda_D \equiv \sqrt{\epsilon_0 T / n_0 e^2} \sim [0.076\text{mm}]$, and b) the plasma frequency $\omega_p \equiv \sqrt{n_0 e^2 / m \epsilon_0}$, where $\omega_{pe} \sim [560\text{GHz}]$ and $\omega_{pi} \sim [9\text{GHz}]$. Drift waves occur well within the realm of quasineutrality, with structures large compared to the Debye length and evolution on timescales long compared to the Langmuir wave; indeed, the mechanisms which maintain quasineutrality are those that give birth to the drift wave. Drift waves are often called ‘low frequency’ waves, because they evolve on timescales long compared to the ion-cyclotron period $\omega \ll \omega_{ci} \equiv eB/m_i \sim [250\text{MHz}]$, and it is this property that makes the guiding centre decomposition useful in describing drift waves. Since independent electron and ion dynamics is the essential characteristic of all drift waves, it is clear that each species must be treated independently, and that a single conducting fluid (MHD) model cannot describe a drift wave.

The simplest drift wave can be illustrated by considering the ion fluid with an ‘adiabatic’ electron response to the electrostatic potential; we consider an ion density perturbation (acoustic wave) in the presence of a ‘radial’ density gradient, in a slab of plasma in a homogeneous field. Here we assume a magnetic field $\mathbf{B} = B\mathbf{e}_z$, a perturbation wavevector $\mathbf{k} = k\mathbf{e}_y$, and a density gradient with lengthscale L_n such that $\nabla n_0 / n_0 = -\mathbf{e}_x / L_n$ and $\mathbf{v}_{\text{dia,e}} = (T_e / eBL_n)\mathbf{e}_y$. The ion continuity equation is

$$\frac{\partial N_i}{\partial t} + \nabla \cdot (N_i \mathbf{v}_{\text{fluid}}) = 0, \tag{1.12}$$

where $\nabla \cdot [N_i \mathbf{v}_{\text{dia}}] = 0$ and $\mathbf{v}_d = 0$ in the slab limit. This continuity equation is linearised by assuming a small perturbation to the density $N_i = n_0 + \tilde{n}_i$ with $|\tilde{n}_i| \ll n_0$, where the tilde indicates a time dependent quantity. The equilibrium density n_0 is constant in time and over a flux surface ($\nabla_\parallel n_0 = 0$). Since the plasma must remain neutral, n_0 represents the unperturbed density for both the electrons and the ions. The perturbation may then be written in the form

$$\tilde{n}_i(\mathbf{x}, t) = \bar{n}_i \exp(i[\mathbf{k} \cdot \mathbf{x} - \bar{\omega} t]), \tag{1.13}$$

where $\bar{\omega} = \omega + i\gamma$ may in general be complex, consisting of both a frequency ω and growth rate γ. The perturbed potential $\tilde{\phi}$ is also written in harmonic form, with

$$\tilde{\mathbf{v}}_E = \frac{\mathbf{b} \times \nabla \tilde{\phi}}{B} = -\frac{ik\tilde{\phi}}{B} \mathbf{e}_x. \tag{1.14}$$

The linearisation of the continuity equation ($\bar{n}_i \ll n_0$) then gives

$$\frac{\partial \tilde{n}_i}{\partial t} = -\tilde{\mathbf{v}}_E \cdot \nabla n_0, \tag{1.15}$$

and substitution of the harmonic form of the perturbations into the derivatives gives

$$-i\omega \bar{n}_i = -\frac{ik\phi}{B} \frac{n_0}{L_n}. \tag{1.16}$$

Assuming an isotropic plasma and neglecting friction (collisions), the parallel electron dynamics obey the force balance

$$m_e N_e \frac{\partial v_{\parallel,e}}{dt} = -\nabla_\parallel p_e + e N_e \nabla \phi. \tag{1.17}$$

Considering the fast parallel thermal motion of the electrons, it can be assumed (as a reasonable first approximation) that they equilibrate 'instantaneously' as compared to the ion dynamics. Assuming a uniform temperature, the parallel force balance can then be written as

$$T_e \nabla N_e = e N_e \nabla \phi, \tag{1.18}$$

which on integration gives the Boltzmann relation

$$N_e = n_0 \exp(e\phi/T_e) \Rightarrow \bar{n}_e = n_0 \left[\exp(e\phi/T_e) - 1\right]. \tag{1.19}$$

where the constraint $N_e = n_0$ when $\phi = 0$ was used. Again linearising ($\bar{n}_e \ll n_0$), the adiabatic electron response is written as

$$\bar{n}_e = n_0 e\phi/T_e, \tag{1.20}$$

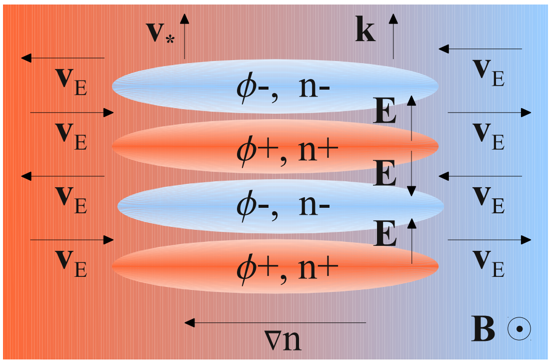

Figure 1.4: Conceptual picture of a simple drift wave with $k_x \ll k_y$ in a slab: Electrons stream away from an initial density perturbation ($n+/n-$) faster than the ions, generating a potential perturbation ($\phi+/\phi-$) in phase with the density perturbation. The resulting electric field causes an $E \times B$ drift for the ions around the contours of constant potential, with the net $E \times B$ drifts aligned with the density gradient. This causes denser plasma to be brought into the region above the region of higher density, and rarer plasma to be bought into the region below. The perturbation thus propagates upwards, in the electron diamagnetic direction.

where the exponential is reduced using its Taylor series.[8] Finally, quasineutrality is imposed by requiring $n_i = n_e$, eliminating ϕ from Eq. (1.16) to obtain the frequency of the drift wave

$$\bar{\omega} = \frac{kT_e}{eBL_n} \equiv \omega_* . \tag{1.21}$$

Since the phase velocity $v_\mathrm{ph} = v_* = \omega_*/k$ for this wave is the same as the previously introduced diamagnetic velocity, the frequency ω_* is referred to as the diamagnetic frequency. It can be seen that although the diamagnetic effect and the propagation of the drift wave are distinct processes, both are collective plasma motions due to the density gradient. The mechanisms of this simplified picture are summarised in Fig. 1.4, which begins with a density perturbation and proceeds with a chain of cause and effects. Whilst pictorial descriptions such as this offer insight, the chain of cause and effect can be misleading. In reality, it is necessary to consider all the processes acting simultaneously to together maintain persistent quasineutrality.

Since this simple drift wave has a purely real frequency, it propagates without growth or decay, with the perturbations in the potential and density propagating in phase. It can be seen from Fig. 1.4, however, that if a certain phase shift between the potential and density waves is introduced, a feedback loop can occur which draws higher density plasma into the already dense region, allowing the mode to tap the

---

[8] For zonal modes with $k_y = 0$, the constraint $\{\bar{n}_e\} = 0$ is used to find the constant of integration, which leads to $\bar{n}_e = n_0 e(\phi - \{\phi\})/T_e$, where $\{\}$ represents the flux surface average [7].

free energy present in the density gradient and driving an instability that grows exponentially (the mode frequency $\bar{\omega}$ acquires an imaginary component). Such a phase shift can occur if friction is included in the electron response, in which case the instability is called a 'dissipative instability'.[9]

In a tokamak, the curvature drifts due to the toroidal field lead to a coupling between temperature and density perturbations such that a temperature gradient can drive instability even if the density and potential perturbations are in phase. These 'reactive' (or 'interchange') instabilities tend to dominate the dissipative instabilities in the tokamak core, due to the lower collisionality at hotter temperatures. At small amplitudes, these microinstabilities exhibit exponential growth, but as the amplitudes grow, nonlinear interaction between modes at competing scales causes turbulent saturation. Individual drift wave modes should therefore be viewed as abstractions, since in a tokamak they cannot be experimentally observed in their linear form. In the turbulent nonlinear phase, these linear modes provide the Fourier harmonics for a decomposition of the plasma state over sinusoidal basis functions, and serve as a powerful tool for both modelling and understanding its behaviour.

Whilst many drift waves exist, many with multiple branches, here we focus on two reactive electrostatic drift waves that are known to be the most important for determining transport under typical tokamak operating conditions: The ion temperature gradient (ITG) driven mode, and the trapped electron mode (TEM). We present the linear mechanisms which drive these instabilities, before discussing various models used to describe them.

1.5.1 Ion temperature gradient mode

The toroidal ion temperature gradient mode (ITG mode) arises when the magnetic field gradient due to the toroidal curvature is aligned with the ion temperature gradient, and is regarded to be the dominant transport mechanism in large aspect ratio tokamaks.[10]

A simple physical picture of the ITG mode is presented in figure Fig. 1.5. We consider an initial perturbation in the ion temperature $\tilde{T}_i$, radially elongated, on the outboard (low **B** field) side of the tokamak. The velocity dependence of the curvature and grad-B drifts $\mathbf{v}_d \sim (v_\parallel^2 + v_\perp^2/2)$ means that the net drift in the hotter ion region is greater than that in the cooler ion region, resulting in a compression and rarefaction of the ion density which is $\pi/2$ out of phase with the initial temperature perturbation. As discussed in the previous section, the ion density perturbation $\tilde{n}$ is coupled to a

---

[9] This type of instability, sometimes called the 'universal instability' has been closely studied and observed in the linear phase in linear confinement devices with high collisionality (relative to a tokamak).

[10] A slab branch of the ITG mode, occuring at weak toroidal coupling, is not considered here.

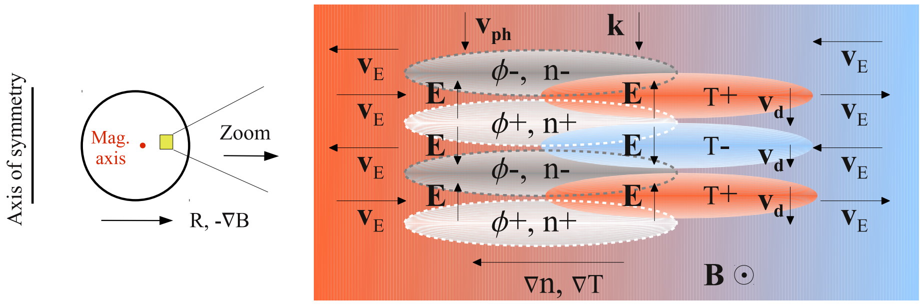

(a) Poloidal cross-section (b) Perturbation in the ions on the outboard side

Figure 1.5: Conceptual picture of the tokamak ion temperature gradient mode with $k_\psi \ll k_\theta$, indicating the directions of the $E{\times}B$ drifts which reinforce the instability. With an adiabatic electron response, the density perturbation is in phase with the potential perturbation, as in Fig. 1.4, but the temperature perturbation is $\pi/2$ out of phase. (The lateral displacement of the perturbations is for visual clarity only). Propagation is downwards, in the ion diamagnetic direction.

potential perturbation $\tilde{\phi}$ by the fast parallel motion of the electrons, and assuming an adiabatic electron response, these perturbations are in phase. With a gradient in the background temperature, one can see that the $E{\times}B$ drift of the ions around the contours of constant potential convects hot plasma from the inside into the hotter regions of the perturbation, and cooler plasma from the outside into the cooler regions. This final link in the chain closes a positive feedback loop, and shows that the instability is driven by the ion temperature gradient. In contrast to the previous simple drift wave, the perturbation propagates in the ion diamagnetic direction, because the $\mathbf{v}_d$ compression dominates. On the same flux surface on the inboard side of the tokamak, the direction of the temperature gradient is reversed and the feedback mechanism is inverted, damping the initial perturbation and preventing instability.

The time averaged radial particle flux generated by the perturbation

$$\Gamma_i = \langle\!\langle N_i \mathbf{v}_{\mathrm{fluid}} \cdot \mathbf{e}_x \rangle\!\rangle = \langle\!\langle \tilde{n}_i \tilde{\mathbf{v}}_E \cdot \mathbf{e}_x \rangle\!\rangle, \tag{1.22}$$

(the time average $\langle\!\langle\rangle\!\rangle$ of a single fluctuating quantity is zero) will always be zero, since $\tilde{\phi}$ and $\tilde{n}$ are always in phase (true for all calculations with adiabatic electrons), but can be nonzero if they go out of phase (when the electrons are modelled kinetically). However, the heat flux

$$Q_i = \langle\!\langle \tilde{T}_i \tilde{\mathbf{v}}_E \cdot \mathbf{e}_x \rangle\!\rangle, \tag{1.23}$$

will be nonzero due to the phase shift between $\tilde{T}_i$ and $\tilde{\phi}$. The instability thus transports heat down the temperature gradient, and herein lies its importance for

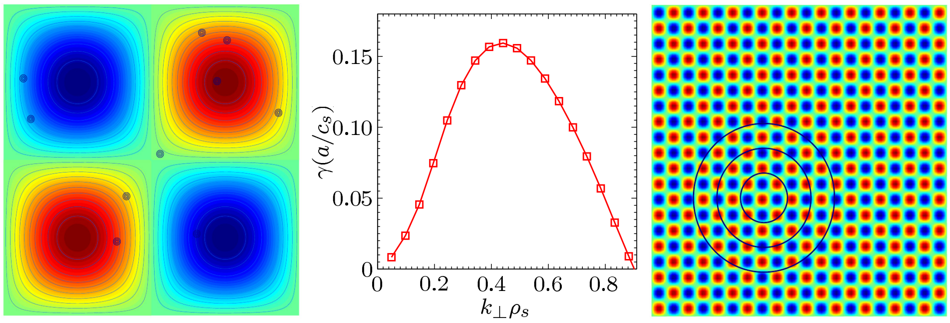

(a) $k_\perp \rho_i \ll 1$ (b) Growth rate spectrum (c) $k_\perp \rho_i \gg 1$

Figure 1.6: Illustration of the long (a) and short (c) wavelength limits for linear modes. (b) The ITG mode growth rate spectrum for the GA-STD case (see Chapter 4) with $\hat{s} = 0$ and adiabatic electrons. Figs. (a) and (c) courtesy of C.M. Roach.

the observed anomalous transport. Calculation of the magnitude of the fluxes requires knowledge of the saturation amplitude of the fluctuations, which can only be obtained from nonlinear calculations.

This ion fluid picture serves to illustrate the underlying mechanisms which drive the ITG instability, and constrains its timescales to

$$\underbrace{k_\parallel v_{\mathrm{th,i}}}_{[0.1\mathrm{MHz}]} \ll \omega \ll \underbrace{k_\parallel v_{\mathrm{th,e}}}_{[10\mathrm{MHz}]}, \tag{1.24}$$

with structures on the scale of the ion Larmor radius $1/k_\perp \sim \rho_i$ [4 mm]. A quantitative treatment using a model similar to that of the previous section finds a growth rate proportional to k_θ (the phase shift generates an imaginary part in Eq. (1.21)). However, the fluid model is only valid in the limit $k_\perp \rho_i \ll 1$, when the structures of the instability are larger than the ion gyroradius. When the structures are small compared with the ion gyroradius ($k_\perp \rho_i \gg 1$), the $E \times B$ drift averages to zero over the course of the fast gyro-orbit, and the instability is suppressed (referred to as finite (nonzero) Larmor radius (FLR) effects). These limits, and a typical ITG growth rate spectrum are illustrated in Fig. 1.6. At intermediate scales ($k_\perp \rho_i \sim 1$), the averaging of the $E \times B$ drifts over the gyro-orbit are needed to accurately determine the stability. At the smallest scales, the effects of polarisation Eq. (1.6) must also be kept for an accurate stability calculation. Gyrofluid models containing simplified FLR effects can achieve accurate results, but require calibration against a kinetic model, since the distribution of gyro-orbits couple velocity space structure to real space.

1.5.2 Trapped electron mode

Recalling the trapping condition Eq. (1.9), a subset of electrons have their parallel velocity reversed by magnetic mirror force before they can complete a full poloidal orbit. These particles are trapped on the low field side of a flux surface, where they complete so called 'banana orbits' with bounce frequency

$$\omega_{Be} = v_{\parallel} \frac{\sqrt{\epsilon/2}}{q R_{\text{axis}}} \sim [1\text{MHz}]. \tag{1.25}$$

Unlike the passing electrons, the parallel motion of trapped electrons along a field line is restricted by this confinement. For a drift wave with $\omega \ll \omega_{Be}$, the trapped electrons do not participate in the parallel dynamics that determine quasineutrality, and averaged over the bounce cycle they have no parallel motion. The dynamics of the trapped electrons therefore bears resemblance to that of the ions, and a trapped electron mode (TEM) exists analogous to the ITG mode, primarily driven by gradients in the electron temperature. In the TEM, the trapped electrons play the role of the ions in the ITG, and the passing electrons provide the parallel dynamics [8]. In models which describe both modes, the TEM in the linear phase can usually be distinguished from the ITG mode by its propagation in the electron diamagnetic direction.

Given the above, the ordering of timescales for trapped electron modes can be written as:

$$\underbrace{\omega_{Bi}}_{[0.01\text{MHz}]} < \underbrace{k_{\parallel} v_{\text{th,i}}}_{[0.1\text{MHz}]} \ll \omega \ll \underbrace{\omega_{Be}}_{[1\text{MHz}]} \sim \underbrace{k_{\parallel} v_{\text{th,e}}}_{[10\text{MHz}]} . \tag{1.26}$$

These orderings, and those for the ITG will be formalised in Chapter 2.

1.6 The gyrokinetic model

Tokamak plasmas in the core may be accurately modelled as an ideal classical plasma: They are fully ionised, the number of particles in the Debye sphere is large ($e^2 n^{1/3}/T \ll 1$), the thermal velocities are non-relativistic ($v_{\text{th}} \ll c$), and they are far from electron degeneracy conditions ($T \gg \hbar n^{2/3}/m$). These plasmas are described by the Vlasov equation [9]

$$\frac{\partial F}{\partial t} + \mathbf{v} \cdot \frac{\partial F}{\partial \mathbf{x}} + \frac{q}{m} \left[\mathbf{E}(\mathbf{x}) + \mathbf{v} \times \mathbf{B}(\mathbf{x}) \right] \cdot \frac{\partial F}{\partial \mathbf{v}} = 0, \tag{1.27}$$

for a continuum distribution function $F(\mathbf{x}, \mathbf{v})$. This equation is the kinetic extension of the continuity equation into the six dimensional phase space of position and velocity. An important kinetic property of this equation is the presence of collisionless

(Landau) damping that occurs for longitudinal waves due to a resonance between the wave phase velocity and the particles with that thermal velocity [10].

The Vlasov equation must be solved independently for each plasma species, and together with the Maxwell equations forms a system of partial differential equations capable of describing all wave phenomena in a classical plasma. In general, however, the high dimensionality and nonlinear nature of the full system mean that direct solutions describing real world plasmas are intractable, both analytically and numerically, and simplifications must be made.

The length and time scale conditions introduced with guiding centre motion suggest a reduction in dimensionality: By averaging over the fastest cyclotron motion, the velocity space may be reduced to only two dimensions $(v_\parallel, v_\perp)$. This 'gyroaveraging' process removes the fastest gyro-orbit timescales, but keeps average spatial variation over the course of the orbit [11]. The gyrokinetic equation, in modelling gyrorings, contains the finite Larmor radius (FLR) effects which cause the high-k rollover in the ITG mode spectrum (Fig. 1.6), and keeps FLR effects and length scales smaller than the gyroradius.[11] This process, described in Chapter 2, yields the gyrokinetic (Vlasov) equation. The gyrokinetic equation is suited to describing waves with frequency $\omega \ll \omega_{ci}$, such as the drift waves discussed above, but fast waves (such as the cyclotron or Langmuir waves) fall outside its domain.

Beyond the gyroaveraging procedure, the 'local' gyrokinetic model takes advantage of the properties of tokamak drift-wave turbulence to further reduce the numerical problem to a tractable level: First, the perpendicular scales of the eddies can be assumed smaller than the system length scales $(1/R \ll k_\perp \sim 1/\rho_i)$ so that the turbulence can be assumed homogeneous perpendicular to the field. This assumption, combined with the toroidal axisymmetry of the tokamak allows the simulation of a much reduced domain. By using coordinates aligned to the magnetic field, and periodic boundaries (described in Chapter 3), these properties of the turbulence allow a powerful pseudo-spectral approach to be used.[12] Second, the observation of the weak nature of drift wave turbulence $(\tilde{n}/n_0 \ll 1)$ allows the splitting of the equations into perturbed and equilibrium parts, and suggests a small parameter expansion keeping only the most important terms.

The combination of all these techniques allows nonlinear numerical solutions of the gyrokinetic equation over the timescales needed to model drift wave turbulence, on a grid size ($\sim$ 50 million grid points) which is increasingly tractable on modern high performance computing hardware.

---

[11] The drift-kinetic equation, in contrast, assumes zero Larmor radius and does not produce the high-k rollover in the ITG growth rate mode spectrum.

[12] A pseudo-spectral approach uses a Fourier decomposition and takes advantage of fast Fourier transform (FFT) algorithms to evaluate the nonlinear terms.

1.7 A brief history of tokamak transport models

The computing power necessary to tackle even the local nonlinear gyrokinetic problem has become available only relatively recently, and earlier progress was made using simplified models which grew in complexity over time. We have already seen that independent dynamics of electrons and ions is fundamental to the drift wave, which precludes a conducting fluid MHD description. However, fluid models treating the ions as a fluid and electrons with a Boltzmann response are able to correctly describe many features of drift waves, and were the primary focus of research before increased computing power led to the present state-of-the-art gyrokinetic models.

The extension of simple models such as those in Sec. 1.5 first led to 'quasilinear' fluid models, in which FLR effects, Landau damping and nonlinear saturation were included in the equation of state closure relation [8, 12–14]. These models are able to identify qualitative properties of drift waves, including 'critical gradient' stability thresholds in temperature and density, and can reproduce experimental heat diffusivity parametric trends. Above the critical temperature gradient, the turbulent transport of heat rises sharply ('profile stiffness'), with the interpretation that any temperature profile with a gradient much above the critical value would quickly relax towards it, so that equilibrium temperature profiles should exist near the critical gradient ('marginal stability').

Later, the approach of taking moments of the gyrokinetic equation led to fully nonlinear gyrofluid models [7, 15–20], which also include trapped electron effects[13], zonal flow dynamics, and more advanced closure relations. Nonlinear gyrofluid models are able to make quantitative predictions of turbulent transport, but require checking against gyrokinetic models when exploring new parameter regimes.

Local fluid and gyrofluid models of drift waves were used to calibrate a number of simpler transport models (e.g. [21–23]) which made varying predictions for scaling of energy confinement time from present devices to ITER. More advanced transport models continue to be developed, which today are calibrated against gyrokinetic simulations [24–26]. The physics of marginal stability means that accurate determination of the critical gradient is crucial to predictions of achievable confinement. In the nineties, the discrepancy between the predictions of these models was such that considerable uncertainty existed as to whether the then ITER design would meet its design criteria of reaching a burning plasma.

A major development came when it became clear that undamped zonal (poloidal) flows (Fig. 1.7) could persist in the plasma and play an important role in determining turbulent saturation [27]. Zonal flows, whilst linearly stable, may

---

[13] Trapped electron effects can be included in fluid models by adding the trapped electrons as an independent bounce averaged species.

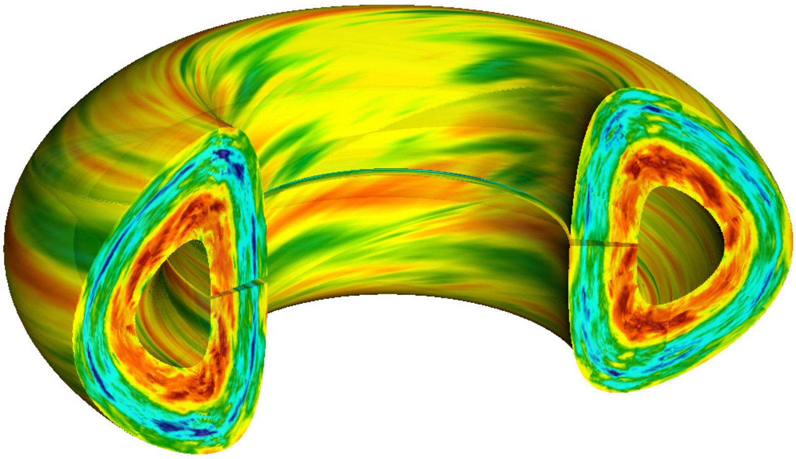

Figure 1.7: Gyrokinetic simulation by GKW showing fully developed turbulence dominated by zonal flows; $k_\theta = 0, k_\psi > 0$.

be driven by nonlinear interaction, and the associated perpendicular $E\times B$ shear can break apart the largest scale turbulent structures, limiting the $E\times B$ convective transport to smaller scales [28, 29]. Furthermore, the zonal flows themselves do not contribute to radial transport, providing a benign repository for the free energy which drives the turbulence [30].

By this time, nonlinear gyrokinetic simulations were becoming computationally accessible and it became possible to carry out a benchmark of the reduced models against gyrokinetic codes [31]. This landmark benchmark showed that the critical temperature gradient to drive turbulence in nonlinear simulations is larger than the critical gradient for linear stability, due to the suppression of turbulence by zonal flows. The gyrokinetic codes gave similar answers, in contrast to the differences between the simpler transport models.

The 'drift-wave zonal flow' paradigm, in which turbulence self-regulates via a nonlinear feedback with zonal flows has become well established in recent years [32, 33]. However, it should also be noted that zonal flows do not provide the saturation mechanism in all regimes [34] and that nonlinear saturation and secondary instabilities also have a role to play [35, 36].

It has become clear non-zonal sheared flows also have an important role to play in transport reduction (discussed further in Chapter 4), and in the formation of transport barriers in which turbulent transport is eliminated [37–39]. Transport barriers provide access to higher confinement regimes (H-mode): When strong external heating is applied to a plasma with a 'divertor' configuration, (which has a magnetic ‘X’ point in its last closed flux surface), transport in the edge region of the plasma is suppressed, leading to a steeper temperature gradient in this region, and a factor of 2 improvement in overall confinement [40]. A quantitative understanding of H-mode formation is still lacking, but turbulence suppression by sheared flow is likely to be an important part of it [39].

In the last decade, the gyrokinetic codes have expanded to include additional physical effects (collisions, magnetic fluctuations, generalised geometry, global effects) and now provide a good (although not complete) basis for predicting core heat transport for many conditions, allowing theory based predictions to provide a complimentary alternative to the zero dimensional scaling laws made from large experimental databases.

Whilst turbulent transport occurs by very different mechanisms from collisional transport, it is still driven by temperature and density gradients. Turbulent transport of heat, particles and momentum are thus often characterised in terms of diffusivities which may be written as the diagonal components of a transport matrix

$$\begin{bmatrix} \Gamma \\ Q/n \\ \Pi_\varphi/R_A n_i m_i \end{bmatrix} = \begin{bmatrix} D & \cdot & \cdot \\ \cdot & \chi & \cdot \\ \cdot & \cdot & \chi_\varphi \end{bmatrix} \begin{bmatrix} -\nabla n \\ -\nabla T \\ -R_A \nabla \omega_\varphi \end{bmatrix}, \tag{1.28}$$

where the left hand side vector describes particle, heat and angular momentum fluxes respectively, and the diagonal matrix components describe the diffusivities of each. This matrix serves as a framework often used in the interpretation and analysis of turbulent transport, but should be viewed only as schematic: The coefficients in the matrix are nonlinear functions of the gradients and depend on many plasma parameters. The off-diagonal elements, which characterise cross-coupling between transport channels, can be nonzero; for example, the density gradient might play a role in driving heat transport.

The gyrokinetic codes initially focused on predicting heat and particle transport, and the description of turbulent transport of plasma angular momentum was slower to develop. The observation of ‘spontaneous’ (or ‘intrinsic’) plasma rotation in the absence of an external torque [41–43] led to a renewed interest in plasma rotation, and a focus on rotation measurement. These measurements in turn generated theoretical attention on nondiffusive mechanisms of anomalous momentum transport, which occur through symmetry breaking in the gyrokinetic equation [44–46], and are not all easily accommodated within the paradigm of the diffusional transport matrix.

1.8 Outline

The physics presented in this chapter is intended to give the interested non-specialist reader an introduction to the concepts which form a starting point for this thesis, and is necessarily cursory. For a more in depth introduction to tokamak physics, we refer the reader to Refs. [47–52], for drift waves and tokamak transport theory to Refs. [6, 8, 17, 39, 51], and for zonal flow to Refs. [31–33].

The work of this thesis has been intimately connected with the recent development of a new nonlinear gyrokinetic code GKW (Gyrokinetics @ Warwick) for modelling drift wave turbulence. GKW solves the nonlinear gyrokinetic Vlasov equations in a toroidally symmetric geometry, using field aligned coordinates, the local approximation and pseudo-spectral methods introduced above. A distinguishing feature of GKW is that the equations are formulated in the rotating frame of reference, which allows for a natural inclusion of the effects of rotation on the turbulence. The challenging dimensionality of the nonlinear gyrokinetic problem requires an efficient parallelisation of GKW (using the message passing interface) to many processors, to allow it to take advantage of modern high performance computing clusters.

The first contribution of this thesis is the extension of the gyrokinetic model to strongly rotating plasmas: The gyrokinetic equations of GKW are extended to include the centrifugal force, and their implementation is described, the first in any gyrokinetic code. Using these new inertial terms, the effect of strong plasma rotation on heat, particle, and impurity transport are explored in both linear and nonlinear simulations.

A number of symmetry breaking mechanisms in the gyrokinetic equation can lead to turbulent momentum transport and influence the equilibrium plasma rotation profile. This is a highly active area of research, and the second contribution of this thesis is a quantitative investigation of the turbulent momentum transport due to the symmetry breaking caused by sheared background $E \times B$ flow. This work includes the theory, implementation, testing, and benchmarking of background $E \times B$ shear in GKW, and a suite of nonlinear simulations.

The model, orderings, coordinates used and equations solved in GKW are described in detail in Chapters 2 and 3. Chapter 2 describes the gyrokinetic theory in a rotating frame of reference, including the extension to strongly rotating plasmas via the inclusion of the centrifugal force. Chapter 3 describes the methods used to allow numerical solution of this equation in a local model, including geometry, normalisations and spectral representation. Chapter 4 investigates methods for consistent inclusion of a sheared background flow in a spectral model, and describes the method and implementation chosen for GKW. The remaining chapters then investigate new physics using these extensions to the code: Chapter 5 discusses mechanisms of symmetry breaking in the gyrokinetic equation which lead to turbulent momentum transport, focusing on quantification of the symmetry breaking by background $E \times B$ shear. Chapter 6 examines the consequences of strong rotation and the centrifugal force on tokamak heat, particle and impurity transport. In Chapter 7, these new contributions to the field are summarised, their consequences in the context of the field are discussed, and future directions are outlined.

Chapter 2

Gyrokinetic theory

2.1 Introduction

Early derivations of the nonlinear gyrokinetic equations [11] proceeded by separating the Vlasov equation into adiabatic (gyrophase independent) and non-adiabatic (gyrophase dependent) components [53], expanding in a small parameter $\rho_* = \rho_i/R$, and finally removing the gyrophase dependence through a gyroaveraging procedure. Modern derivations proceed by a Hamiltonian approach, in which the fast gyromotion timescale is separated from the guiding centre motion by a phase space transformation on the Lagrangian using Lie-Transform methods [54]. These modern derivations place an emphasis on preserving the conservation laws of the system, and guarantee energy and momentum conservation at each order in the expansion.

In Chapter 1 the basic principles of the gyrokinetic ordering were outlined; here we formalise the theory into its mathematical framework and present the gyrokinetic equations in the rotating frame of reference, applicable to the case of a strongly rotating plasma. The equations are derived from the starting point of the gyrocentre Lagrangian in the rotating frame [55], and presented in the local limit. Gyrokinetic theory has undergone two decades of development and intensive study, and we cannot hope to do justice here to all its literature: For established results we summarise the relevant points and point to the literature, and restrict detailed exposition to the new developments of this thesis. This derivation is a hybridisation of the work in [56–59] and is restricted to the collisionless electrostatic limit; further details of electromagnetic and collisional terms may be found in [58, 59].

2.2 Gyrokinetic Orderings

The gyrokinetic formalism exploits spatio-temporal scale separation through an asymptotic small parameter expansion, physically motivated by the properties of the drift waves introduced in Sec. 1.5. The observed properties of drift wave turbulence can be formalised into three distinct small parameters: ϵ_ω, ϵ_B, and ϵ_δ, describing time scale separation, space scale separation, and fluctuation amplitudes respectively [54]. The fundamental principle of gyrokinetics is the removal of the fast cyclotron timescale, allowing for a tractable treatment of phenomena with a low frequency ω relative to the cyclotron frequency. This central idea is expressed in the timescale ordering parameter

$$\frac{\omega}{\omega_{ce}} \sim \epsilon_\omega \ll 1. \tag{2.1}$$

The spatial variations in the background quantities $Q = \{B, T, n, \omega_\varphi\}$ are expressed in logarithmic gradient length scales $1/L_Q = |\nabla \ln Q| = |\nabla Q|/|Q|$, all of which are ordered to be on the scale of the device

$$R \sim L_n \sim L_T \sim L_B \sim L_\varphi. \tag{2.2}$$

The gyrokinetic ordering allows for perpendicular fluctuations on the scale of the gyroradius, such that the parameter $\epsilon_\perp \equiv k_\perp \rho_i \sim 1$ is not ordered small (unlike in drift kinetic theory). Fluctuations are assumed to occur on the scale of the gyroradius, which is ordered small relative to the background gradients, as expressed in the spatial scale ordering parameter

$$\frac{\rho_i}{R} \sim \frac{\rho_i}{L_T} \sim \epsilon_B \ll 1. \tag{2.3}$$

The transport timescale for evolution in the background quantities must be long compared to the turbulent fluctuations, which can be expressed as [54, 60]

$$\left| \frac{1}{\omega_{ci}} \frac{\partial \ln Q}{\partial t} \right| \sim \epsilon_B^3. \tag{2.4}$$

Finally, the small amplitude of fluctuations is described by the fluctuation parameter

$$\left| \frac{\delta n}{n} \right| \sim \frac{e\delta\phi}{T} \sim \epsilon_\delta \ll 1. \tag{2.5}$$

For the ITER core parameters and the ITG drift wave, these small parameters are estimated to be [$\epsilon_\omega \sim 0.0004$], [$\epsilon_B \sim 0.0007$], and [$\epsilon_\delta \sim 0.01$]. Unlike the other two parameters, ϵ_δ is not calculated from a simple formula from the basic plasma properties, and must be measured experimentally to validate its use as a small ordering parameter. A number of measurements in medium sized tokamaks have found $\epsilon_\delta \sim 0.001 - 0.1$, (see, for example Refs. [61–64]), and it is found to approximately scale with ϵ_B [65, 66], so should be smaller in ITER than in present devices. Values of ϵ_δ predicted by the nonlinear models provide a direct check on their validity.

Gyrokinetic equations applicable to different plasma regimes may be derived by choosing different orderings for each of the parameters $\epsilon_\omega, \epsilon_\delta, \epsilon_B$ above. For the case of large aspect ratio tokamak core turbulence, the simplest ordering $\epsilon_\omega \sim \epsilon_\delta \sim \epsilon_B$ is usually employed, and the expansion is expressed purely in terms of the normalised gyroradius

$$\rho_* \equiv \frac{\rho_i}{R} \equiv \epsilon_B. \tag{2.6}$$

To exploit the ordering of Eq. (2.5), the δf approximation may be used for core turbulence, in which the distribution function $f_{\mathrm{tot}} = F + f$ is split into a perturbed distribution f and a background distribution F with ordering

$$f \sim \rho_* F. \tag{2.7}$$

This formulation is used in GKW in conjunction with the local limit described in the next section. Turbulent timescale orderings are expressed in terms of the thermal speed $v_{\mathrm{th}} = \sqrt{(2T/m)}$, which describes the parallel streaming along magnetic field lines ($v_\parallel \sim v_{th}$). Fine scale spatial variations in the perturbed parallel structure are smoothed out by this fast parallel motion ($k_\parallel \sim 1/qR$ with $\omega \sim k_\parallel v_{\mathrm{th}}$), but perpendicular length scales may be on the scale of the gyroradius (since $\epsilon_\perp \sim 1$, and $v_D \sim \rho_* v_{th}$). The parallel and perpendicular perturbed dynamics are therefore ordered as

$$\frac{k_\parallel}{k_\perp} \sim \frac{\epsilon_\omega}{\epsilon_\perp} \sim \rho_* \ll 1. \tag{2.8}$$

which is equivalent to ordering the gradients $\nabla_\parallel = \mathbf{b} \cdot \nabla$ and $\nabla_\perp = \nabla - \nabla_\parallel$ of the perturbed distribution as

$$\nabla_\parallel f \sim \rho_* \nabla_\perp f. \tag{2.9}$$

This lengthscale ordering is necessary to describe the drift wave modes introduced in Sec. 1.5: For instabilities to exist, the perpendicular dynamics must be able to compete with the fast parallel dynamics, which is expressed in the ordering $v_\parallel \nabla_\parallel f \sim v_D \nabla_\perp f$.

For the background distribution, the ordering of Eq. (2.3) means that the perpendicular lengthscales of the background distribution are one order lower than those of the perturbed distribution

$$L_{\perp F} \sim \rho_* L_{\perp f} \Rightarrow \nabla_\perp f \sim \nabla_\perp F, \tag{2.10}$$

whilst for parallel derivatives, the lengthscales for the two distributions are equivalent

$$L_{\parallel F} \sim L_{\parallel f} \Rightarrow \nabla_\parallel f \sim \rho_* \nabla_\parallel F. \tag{2.11}$$

The perpendicular guiding centre drifts of Eq. (1.4) are one order smaller than the thermal speed ($v_D \sim \rho_* v_{\text{th}}$), but the plasma rotation $v_{\text{toroidal}} \sim v_{\text{th}}$ is taken to be the same order as the thermal speed (Mach number of order unity).[1] In the laboratory frame, the perpendicular component of the toroidal rotation appears as an $E \times B$ drift velocity which is of the order of the thermal velocity. A background potential (discussed further in Secs. 2.4, 2.7.1 and 3.6) is required for quasineutrality be satisfied in the presence of the centrifugal force [4]. The perturbed potential ϕ, and background potential Φ in the comoving frame are then taken to be of the order

$$\phi \sim \frac{T}{e}\rho_*, \qquad \Phi \sim \frac{T}{e}, \tag{2.12}$$

where T is the temperature, and e is the charge on an electron. This ordering for ϕ corresponds to the linearisation of the electron Boltzmann response introduced in Sec. 1.5. Since Φ is an equilibrium quantity, its gradient length scale is ordered with the system size ($L_\Phi \sim R$) and the perpendicular potential gradients are then of the same order, with $\nabla_\perp \phi \approx \nabla_\perp \Phi$. It follows that the $E \times B$ velocity in the rotating frame is ordered $v_E \sim \rho_* v_{\text{th}}$, the same order as the other drifts. The parallel gradients of both potentials are treated equally, with the result that $\nabla_\parallel \Phi \sim \nabla_\parallel \phi / \rho_*$.

2.3 Local limit

The orderings of Eq. (2.3) and Eq. (2.4) for the background quantities allow the δf approximation to be evaluated in the local limit, in which only a small region is simulated (the local limit requires the δf formulation but not the converse). Using the separation of spatial scales (Eq. (2.3)), the perpendicular extent $l_\perp$ of the simulated domain is considered to be zero as compared to the device ($l_\perp / R \sim 0$), but larger than the turbulence ($l_\perp \gg \rho_i$). The separation of the turbulent and transport timescales (Eq. (2.3)) is used to calculate fluxes through the local flux surface, given a fixed background distribution F. This local approximation means that the background quantities are constant across the domain, but their gradients are kept as as a linear drive term. The effects of profile variation are not kept (parameters for only a single flux surface are used), which is consistent with a first order expansion up to $\mathcal{O}(\rho_*)$.

The utility of the local limit is that the local turbulence is homogeneous in the perpendicular plane (all points are equal), allowing periodic boundary conditions, and a Fourier decomposition to be used in the perpendicular directions. The equations in the following sections will be formulated in the local limit, which allows

---

[1] This ordering of the toroidal rotation distinguishes the equations in this work from those currently used in other gyrokinetic codes and also means the equilibirum is modified.

for some simplification of globally varying quantities.

2.4 Comoving frame

With the strong rotation ordering $v_{\text{toroidal}} \sim v_{\text{th}}$, the perpendicular component of the plasma rotation velocity in the laboratory frame (denoted by superscript L) is an $E\times B$ drift of order $v_E^L \sim v_{\text{th}}$, which breaks the assumption of $v_D \ll v_{th}$ used for the guiding centre motion. The difficulties of this large $E \times B$ velocity can be removed by a transformation to the comoving frame which rotates with the plasma (denoted in this section by superscript *)

$$\mathbf{v}^L = \mathbf{v}^* + \mathbf{u}_0, \tag{2.13}$$

$$\mathrm{d}\mathbf{x}^L = \mathrm{d}\mathbf{x}^* + \mathbf{u}_0 \mathrm{d}t, \tag{2.14}$$

$$\mathrm{d}t^L = \mathrm{d}t^*, \tag{2.15}$$

where $\mathbf{u}_0$ is the frame rotation velocity. Under this transformation the electric field transforms as

$$\mathbf{E}^L = \mathbf{E}^* - \mathbf{u}_0 \times \mathbf{B}. \tag{2.16}$$

The axisymmetric tokamak magnetic field may always be written in the form

$$\mathbf{B} = s_{\text{B}} R B_t(\psi) \nabla\varphi + s_{\text{j}} \nabla\varphi \times \nabla\Psi_p, \tag{2.17}$$

where Ψ_p is the normalised poloidal flux (with $\nabla\Psi_p$ pointing from the plasma axis to the edge), B_t is the toroidal field, and for clarity we define

$$s_{\text{B}} = \text{sign}(\mathbf{B}\cdot\nabla\varphi) = \pm 1, \qquad s_{\text{j}} = \text{sign}(\mathbf{j}\cdot\nabla\varphi) = \pm 1, \tag{2.18}$$

to be the sign of the plasma toroidal field and current relative to the toroidal angle φ which increases clockwise viewed from above.

The plasma angular rotation of an axisymmetric equilibrium is a flux function to order $\mathcal{O}(\rho_*)$, which can be obtained by neglecting viscosity and inertia [4, 67]. In the local model of GKW, we choose a rigid body rotation of the frame such that the rotation of the frame is equal to the rotation of the plasma on the local flux surface. In this frame, the large $E\times B$ flow is removed through the transformation Eq. (2.16), and the equations become similar in form to the non-rotating system. This approach, however, is not suitable for a global description since a gradient in the angular rotation would result in a time dependent metric. The frame rotates rigidly with toroidal angular velocity $\mathbf{\Omega} = -s_B \Omega \nabla Z$, whilst the plasma rotates with angular velocity $\omega_\varphi(\psi) = -s_B \omega_\varphi(\psi)\nabla Z$. The frame velocity is then given by

$$\mathbf{u}_0 = \mathbf{\Omega} \times \mathbf{x} = R^2 \Omega \nabla \varphi. \tag{2.19}$$

Using the axisymmetry of the field Eq. (2.17) it can then be shown that electric potential transforms as

$$\Phi^L = \Phi^* - s_{\mathrm{B}} s_{\mathrm{j}} \Omega \Psi_p. \tag{2.20}$$

The first term on the right hand side is a function of the poloidal angle, whilst the second term is a flux function. The second term $\Omega\Psi_p \sim T/e\rho_* = \mathcal{O}(\rho_*^{-1})$ is one order larger than the first $\Phi_* \sim T/e = \mathcal{O}(1)$. The transformation of Eq. (2.20) therefore removes the potential of $\mathcal{O}(\rho_*^{-1})$, which was responsible for the $v_E^L \sim v_{\mathrm{th}}$ flow. The potential $\Phi_* \equiv \Phi$ that remains is required in order that quasineutrality be maintained [4], and its drift satisfies $v_E^* \sim \rho_* v_{\mathrm{th}}$ which stays within the gyrokinetic ordering (as discussed in Sec. 2.2, the perturbed potential has $\phi \sim \rho_* T/e = \mathcal{O}(\rho_*)$, but the v_E drifts are the same order).[2]

2.5 Lagrangian formalism

The Lagrangian method for deriving the gyrokinetic equation requires consideration of three coordinate systems on the six dimensional phase space:

1. The particle coordinates $(\mathbf{x}, \mathbf{v})$ of position and velocity.

2. The guiding-centre coordinates $(\bar{\mathbf{X}}, v_\parallel, \bar{\mu}, \bar{\alpha})$ in which the particles are represented by their guiding centres with respect to the *equilibrium* fields and a gyrophase angle $\bar{\alpha}$. This phase space describes the guiding centre motion introduced in Chapter 1.

3. The gyrocentre coordinates $(\mathbf{X}, v_\parallel, \mu, \alpha)$ in which the particles are represented by their gyrocentres with respect to the *total* fields (equilibrium plus perturbed) and a gyrophase angle α.[3]

---

[2] In [68], a subsidiary geometrical ordering parameter B_θ/B was used to order $\Omega\Psi_p$ as T/e and the equations were formulated in the Laboratory frame.

[3] In the literature, the overbar is often used for the gyrocentre coordinates.

The relationship between the particle coordinates and the guiding centre coordinates is provided by the transformation [53]

$$\bar{\mathbf{X}}(\mathbf{x},\mathbf{v}) = \mathbf{x} - \boldsymbol{\rho}(\mathbf{x}), \tag{2.21}$$

$$v_\parallel(\mathbf{x},\mathbf{v}) = \mathbf{v}\cdot\mathbf{b}(\mathbf{x}), \tag{2.22}$$

$$\bar{\mu}(\mathbf{x},\mathbf{v}) = \frac{mv_\perp^2(\mathbf{x})}{2B(\mathbf{x})}, \tag{2.23}$$

$$\bar{\alpha}(\mathbf{x},\mathbf{v}) = \cos^{-1}\left(\frac{1}{v_\perp(\mathbf{x})}(\mathbf{b}(\mathbf{x})\times\mathbf{v})\cdot\mathbf{e}_1\right), \tag{2.24}$$

where $\mathbf{b}(\mathbf{x})$ is the unit vector in the direction of the equilibrium magnetic field $\mathbf{B}$, and

$$\boldsymbol{\rho}(\mathbf{x},\bar{\alpha}) = \rho(\mathbf{x})[\mathbf{e}_1\cos\bar{\alpha} + \mathbf{e}_2\sin\bar{\alpha}], \tag{2.25}$$

is the gyroradius vector pointing from the guiding centre to the particle position, with $(\mathbf{b},\mathbf{e}_1,\mathbf{e}_2)$ a right handed orthonormal coordinate system at the guiding centre. This transformation can be explicitly inverted using the approximation $\rho(\mathbf{x}) \approx \rho(\mathbf{X})$, which is valid to first order in ϵ_B.

The transformation to the gyrocentre phase space is constructed as an asymptotic expansion in ϵ_δ, in which the guiding centre transformation is the lowest order term. The Lie transform is used in the construction of the transformation at each order, making use of a gauge freedom at each order to remove the gyrophase dependence. [54, 69, 70]. The result is a 'near-identity' transformation which is invertible provided the phase space is sufficiently well behaved. The transformation can be constructed to arbitrary order, but in practice second order is usually sufficient. In the gyrocentre phase space, the polarisation drift is removed from the equations of motion but appears in the coordinate transformation between the guiding centre and gyrocentre space (see Sec. 2.9).

Using these transformations, the standard Lagrangian for a charged particle in a magnetic field

$$\gamma = (e\mathbf{A} + m\mathbf{v})\cdot d\mathbf{x} - H dt, \qquad H = \frac{m}{2}v^2 + e\phi, \tag{2.26}$$

can be transformed into the gyrocentre Lagrangian in the rotating frame [57]

$$\Gamma = [Ze\mathbf{A} + m(v_\parallel\mathbf{b} + \mathbf{u}_0)]\cdot d\mathbf{X} + \mu \mathrm{d}\alpha - H\mathrm{d}t, \tag{2.27}$$

where the Hamiltonian $H = H_0 + H_1 + H_2 + \mathcal{O}(\rho_*^3)$ is given to first order by

$$H_0 = Ze\langle\Phi\rangle + \frac{1}{2}mv_\parallel^2 + \mu B - \frac{1}{2}m\mathbf{u}_0\cdot\mathbf{u}_0, \qquad H_1 = Ze\langle\phi\rangle. \tag{2.28}$$

The second order part H_2 will be used only for the field equations, and is described in Sec. 2.9. The angle brackets denote the gyroaverage

$$\langle h(\mathbf{x})\rangle = \langle h(\mathbf{X}+\boldsymbol{\rho})\rangle = \frac{1}{2\pi}\int_0^{2\pi} h(\mathbf{X}+\boldsymbol{\rho})d\alpha, \tag{2.29}$$

which is the average of an arbitrary function h over a gyro-orbit. The gyroaverage operator is a function of the perpendicular velocity space, since the gyroradius $\rho(\mathbf{x},\mu)$ depends on the magnetic moment of the particle. The Lagrangian here is given in the symplectic form, in which all time dependent field effects appear in the Hamiltonian. This form allows the field equations to be constructed from functional variations, as outlined in Sec. 2.9. The Hamiltonian is only used to first order H_1 in evaluation of the equations of motion, but the second order part H_2 is used in the derivation of the field equations. In order to guarantee energy consistency for the gyrokinetic-poisson equation set, no approximations should be made after this initial truncation of the Lagrangian [71, 72].

2.6 Equations of motion

The equations of gyrocentre motion in the rotating frame can be derived from the generalised Hamilton's equation for any function h on the phase space

$$\frac{\mathrm{d}h}{\mathrm{d}t} = \{h,H\} + \frac{\partial h}{\partial t}, \tag{2.30}$$

where the generalised guiding centre Poisson bracket [55, 69] is

$$\{F,G\} = \frac{Ze}{m}\left(\frac{\partial F}{\partial\alpha}\frac{\partial G}{\partial\mu} - \frac{\partial F}{\partial\mu}\frac{\partial G}{\partial\alpha}\right) - \frac{\mathbf{b}}{eB_\parallel^*}\cdot\nabla F\times\nabla G + \frac{\mathbf{B}^*}{mB_\parallel^*}\cdot\left(\nabla F\frac{\partial G}{\partial v_\parallel} - \frac{\partial F}{\partial v_\parallel}\nabla G\right), \tag{2.31}$$

for arbitrary functions F and G of the non-canonical coordinates $(\mathbf{X}, v_\parallel, \mu, \alpha)$, and where

$$\mathbf{B}^* = \mathbf{B} + \frac{m}{Ze}\nabla\times(v_\parallel\mathbf{b} + \mathbf{u}_0), \tag{2.32}$$

is a generalised magnetic field with parallel projection

$$B_\parallel^* = \mathbf{b}\cdot\mathbf{B}^*. \tag{2.33}$$

The inclusion of $\mathbf{u}_0$ in $\mathbf{B}^*$ provides the orgin of the inertial forces in what follows.

Choosing $h = [\mathbf{X}, v_\parallel, \mu, \alpha]$ to be each of the coordinates in turn $(\partial h/\partial t = 0)$

produces the equations of motion

$$\begin{aligned}
\frac{\mathrm{d}\mathbf{X}}{\mathrm{d}t} &= \{\mathbf{X}, H\} = \frac{\mathbf{b}}{ZeB_\parallel^*} \times \nabla H + \frac{\mathbf{B}^*}{mB_\parallel^*}\frac{\partial H}{\partial v_\parallel}, && (2.34)\\
\frac{\mathrm{d}v_\parallel}{\mathrm{d}t} &= \{v_\parallel, H\} = -\frac{\mathbf{B}^*}{mB_\parallel^*} \cdot \nabla H = -\frac{1}{mv_\parallel}\frac{\mathrm{d}\mathbf{X}}{\mathrm{d}t} \cdot \nabla H, && (2.35)\\
\frac{\mathrm{d}\mu}{\mathrm{d}t} &= \{\mu, H\} = 0, \qquad \frac{\mathrm{d}\alpha}{\mathrm{d}t} = \{\alpha, H\}. && (2.36)
\end{aligned}$$

The invariance of μ is a requirement for a gyrokinetic theory, and is achieved through a careful construction of the Poisson bracket using a Lie algebra [55].[4] Both $B_\parallel^*$ and $\partial\alpha/\partial t$ are independent of α, which will be used later in the phase space conservation that leads to the gyrokinetic equation. These equations of motion require some manipulation to arrive at a form suitable for implementation in a local gyrokinetic code, as presented below.

The perpendicular part of any vector $\mathbf{p}$ may be written (using the vector identity Eq. (A.1)) as

$$\mathbf{p}_\perp \equiv \mathbf{p} - (\mathbf{p}\cdot\mathbf{b})\mathbf{b} = -\mathbf{b} \times (\mathbf{b} \times \mathbf{p}), \tag{2.37}$$

which, when used in evaluating $(\mathbf{B}^* - B_\parallel^*\mathbf{b})$ gives the ratio

$$\frac{\mathbf{B}^*}{B_\parallel^*} = \mathbf{b} - \frac{m}{ZeB_\parallel^*}\mathbf{b} \times (\mathbf{b} \times \mathbf{p}), \tag{2.38}$$

with, in this case

$$\mathbf{p} = \nabla \times (v_\parallel \mathbf{b} + \mathbf{u}_0). \tag{2.39}$$

For rigid body rotation, $\partial_R \Omega = 0$, and hence one finds

$$\nabla(\mathbf{u}_0 \cdot \mathbf{u}_0) = 2R\Omega^2 \nabla R, \tag{2.40}$$

and using the vector identity Eq. (A.2) on Eq. (2.19) (with $\nabla \cdot \mathbf{x} = 3$), we have

$$\nabla \times \mathbf{u}_0 = 2\boldsymbol{\Omega} \qquad \Rightarrow \qquad \mathbf{p} = v_\parallel \nabla \times \mathbf{b} + 2\boldsymbol{\Omega}. \tag{2.41}$$

Using the identity Eq. (A.3) we find

$$\mathbf{b} \times (\nabla \times \mathbf{b}) = -(\mathbf{b}\cdot\nabla)\mathbf{b}, \tag{2.42}$$

---

[4] In higher order expansions, the invariance of the magnetic moment $\mu = mv_\perp^2/2B$ used here can be broken by low-frequency short-wavelength perpendicular fluctuations [73] and a higher order adiabatic invariant $\bar{\mu}$ can be defined [54]. For the orderings used here, the two are equivalent.

which on substitution into Eq. (2.38) gives

$$\frac{\mathbf{B}^*}{B_\parallel^*} = \mathbf{b} + \frac{mv_\parallel}{ZeB_\parallel^*}\mathbf{b}\times(\mathbf{b}\cdot\nabla)\mathbf{b} + \frac{2m}{ZeB_\parallel^*}\mathbf{\Omega}_\perp, \tag{2.43}$$

where $\mathbf{\Omega}_\perp$ is the rotation vector perpendicular to the field, as defined by Eq. (2.37). Substituting these relations into Eq. (2.34) finally yields the gyrocentre velocity

$$\frac{\mathrm{d}\mathbf{X}}{\mathrm{d}t} = v_\parallel\mathbf{b} + \underbrace{\frac{1}{Ze}\frac{mv_\parallel^2}{B_\parallel^*}\mathbf{b}\times(\mathbf{b}\cdot\nabla)\mathbf{b} + \frac{\mu}{Ze}\frac{\mathbf{b}\times\nabla B}{B_\parallel^*} + \frac{2mv_\parallel}{ZeB_\parallel^*}\mathbf{\Omega}_\perp - \frac{m\Omega^2 R}{ZeB_\parallel^*}\mathbf{b}\times\nabla R + \frac{\mathbf{b}\times\nabla\langle\Phi\rangle}{B_\parallel^*}}_{\mathbf{v}_D} + \underbrace{\frac{\mathbf{b}\times\nabla\langle\phi\rangle}{B_\parallel^*}}_{\mathbf{v}_E} \tag{2.44}$$

At this point we note from our assumed orderings that even with the Mach number ordered as unity, $B_\parallel^*$ does not differ much from B

$$B_\parallel^* = B[1+2\Omega/\omega_c] \sim B[1+\mathcal{O}(\rho_*)], \tag{2.45}$$

in the local model, and hence $B_\parallel^*$ is replaced with B in the equations that follow, which are accurate to $\mathcal{O}(\rho_*)$. To preserve energy conservation, this approximation is also made consistently in Eq. (2.35), Eq. (2.50), and the Jacobian for velocity space integration

$$\mathrm{d}^3\mathbf{v} = \frac{2\pi B_\parallel^*}{m}\mathrm{d}v_\parallel\mathrm{d}\mu \quad \approx \quad \frac{2\pi B}{m}\mathrm{d}v_\parallel\mathrm{d}\mu, \tag{2.46}$$

which will be used in the field equations.

The terms on the right hand side of Eq. (2.44) are grouped as the free streaming motion $v_\parallel\mathbf{b}$, the equilibrium drifts $\mathbf{v}_D$, and the perturbed $\mathbf{v}_E$ drift, as introduced in Sec. 1.3. The drifts appearing in $\mathbf{v}_D$ are, respectively, the curvature and ∇B drifts (together, $\mathbf{v}_d$), two additional drifts arising from inertial forces of the frame (Coriolis and centrifugal), and the $E\times B$ drift from the equilibrium Φ. In terms of Eq. (1.3) the forces responsible for the new inertial drifts are the Coriolis force

$$F_{\mathrm{co}} = 2mv_\parallel\mathbf{b}\times\mathbf{\Omega}, \tag{2.47}$$

and the centrifugal force

$$F_{\mathrm{cf}} = m\Omega^2 R\nabla R, \tag{2.48}$$

respectively. The Coriolis force has no component parallel to the field, and does no work on the particle. The centrifugal force, however, does work on parallel motion, and this results in a modified trapping condition (given in Sec. 2.8).

In contrast to the gyrocentre velocity, the equation of motion for the parallel acceleration requires less manipulation and is obtained directly from Eq. (2.35)

$$m v_\parallel \frac{\mathrm{d}v_\parallel}{\mathrm{d}t} = -\frac{\mathrm{d}\mathbf{X}}{\mathrm{d}t} \cdot \left[Ze\nabla\langle \phi + \Phi \rangle + \mu \nabla B - m\Omega^2 R \nabla R \right], \tag{2.49}$$

in the form that will be used in the following derivation of the gyrokinetic equation. This is also the statement of energy conservation for an individual particle.

2.7 Gyrokinetic equation

The gyrokinetic equation can be derived directly from the Hamilton equation for the guiding centre distribution $f_{\mathrm{tot}}(\mathbf{X}, v_\parallel, \mu)$, and the equations of motion Eqs. (2.34) (2.35) and (2.36). The construction of the gyrocentre coordinates is such that by definition $\partial f_{\mathrm{tot}}/\partial \alpha = 0$. Hamilton's equation guarantees phase space conservation, and it can be shown from the equations of motion that

$$\nabla \cdot \left(B_\parallel^* \frac{\mathrm{d}\mathbf{X}}{\mathrm{d}t} \right) + \frac{\partial}{\partial v_\parallel} \left(B_\parallel^* \frac{\mathrm{d}v_\parallel}{\mathrm{d}t} \right) = 0. \tag{2.50}$$

Applying Hamilton's equation (Eq. (2.30)) to the guiding centre distribution f_{tot} then leads to the gyrokinetic equation

$$\frac{\partial f_{\mathrm{tot}}}{\partial t} + \frac{\mathrm{d}\mathbf{X}}{\mathrm{d}t} \cdot \frac{\partial f_{\mathrm{tot}}}{\partial \mathbf{X}} + \frac{\mathrm{d}v_\parallel}{\mathrm{d}t} \frac{\partial f_{\mathrm{tot}}}{\partial v_\parallel} = 0, \tag{2.51}$$

which can be seen to have the same form as the Vlasov equation Eq. (1.27), and is simply an expression of phase space conservation analogous to the continuity equation in higher dimensional phase space. In the following sections we perform an ordering expansion in ρ_* on the gyrokinetic equation, using the δf formulation in which the distribution is split $f_{\mathrm{tot}} = F + f$, with the orderings described in Sec. 2.2. The advantage of the δf formulation is that the background distribution F is taken to be a stationary equilibrium, which provides a linear source term for the linearised modes in f.

2.7.1 Equilibrium equation

The gyrokinetic equation Eq. (2.51) is expanded to lowest order in ρ_*, (formally $\mathcal{O}(1)$), to obtain the equilibrium equation

$$v_\parallel \mathbf{b} \cdot \nabla F - \frac{1}{m} \mathbf{b} \cdot \left[Ze\nabla\langle \Phi \rangle + \mu \nabla B - m\Omega^2 R \nabla R \right] \frac{\partial F}{\partial v_\parallel} = 0. \tag{2.52}$$

As a consequence of the centrifugal force, the background potential Φ must be retained in the equilibrium in order for quasineutrality to be satisfied [4]. For the ions, this background potential acts to detrap the particles, but is outweighed by the centrifugal force which acts to trap them. The electrons experience an enhanced trapping from the background potential. In the nonrotating case the equilibrium equation reduces to the normal trapping equation

$$v_\parallel \mathbf{b}\cdot\nabla F - \frac{\mu\mathbf{b}}{m}\cdot\nabla B\frac{\partial F}{\partial v_\parallel} = 0, \tag{2.53}$$

for which any isotropic distribution is a trivial solution (though anisotropic solutions also exist, e.g. any function of the constants of motion). The well established 'neoclassical' theory extends statistical thermodynamics to collisional plasmas in toroidal geometry [60], and demonstrates that a Maxwellian distribution is (to lowest order) a maximum entropy equilibrium state for individual flux surfaces. Whilst the tokamak is designed entirely to prevent establishment of a radial thermal equilibrium, the fast parallel motion relative to the ion-ion collision frequency $\nu_{ii} \sim [20 - 200\text{Hz}]$ ensures that parallel thermalisation occurs, giving constant temperature (at lowest order) over a flux surface [49]. When the δf gyrokinetic equations are used in the 'collisionless' limit (as in most of this thesis), collisions are neglected on the perturbed distribution, but some minimum collisionality is always implicit in the assumption of a Maxwellian background. This framework thus depends on the timescales ordering

$$\underbrace{1/\tau_E}_{[0.25Hz]} \ll \underbrace{\nu_{ii}}_{[100Hz]} \ll \omega \ll \underbrace{\omega_{Ti}}_{[100GHz]}, \tag{2.54}$$

where $\tau_E \sim [4s]$ (ITER prediction) is the energy confinement time that characterises radial transport, and $\omega_T = v_{\text{th,i}}/qR$ is the parallel ion transit frequency. Given this ordering, the equilibrium background distribution is assumed to be Maxwellian in velocity space

$$F \equiv F_M = \frac{n}{(2\pi T/m)^{3/2}}\exp\left[-\frac{m(v_\parallel - u_\parallel)^2}{2T} - \frac{\mu B}{T}\right], \tag{2.55}$$

where $u_\parallel = RB_t/B[\omega_\varphi^L(\psi) - \Omega]$. In the comoving frame, $u_\parallel = 0$, but a constant gradient $u' = -(R_A/v_{\text{th}})\partial\omega_\varphi^L/\partial\psi$, in the plasma rotation is kept when derivatives of the Maxwellian are evaluated [57]. Here R_A is the major radius of the magnetic axis. Radial variation in the plasma rotation profile is responsible for diffusive momentum transport and can alter the stability threshold for ITG modes [44].

This Maxwellian is an exact solution of Eq. (2.52), but is not a true plasma equilibrium (except in the absence of radial temperature and density gradients). At next order, $\mathcal{O}(\rho_*)$, the additional term $\mathbf{v}_D \cdot \nabla F_M$ appears, which leads to parallel flow even in the absence of any fluctuations. These flows are of order $\mathcal{O}(\rho_*)$, and can be treated consistently in the perturbed solution f, but in global codes, a true equilibrium may be preferable [74, 75]. When combined with a momentum conserving collision operator, this term allows neoclassical currents (Pfirsch-Schlüter and bootstrap) and fluxes to be calculated consistently within a gyrokinetic code, but it can be discarded when only considering turbulent transport.

Substitution of the derivatives of the Maxwellian (given in the next section) into the equilibrium equation gives

$$\nabla_\parallel \ln(n_0) = -\frac{Ze\nabla_\parallel \langle\Phi\rangle}{T} + \frac{m\Omega^2 R\nabla_\parallel R}{T}, \tag{2.56}$$

the solution of which is

$$n(\theta) = n_{R_0} \exp\left(\frac{-Ze\langle\Phi\rangle}{T} + \frac{m\Omega^2(R^2 - R_0^2)}{2T}\right), \tag{2.57}$$

where $R_0(\psi)$ is a constant of integration chosen to be the major radius at which $n(\theta) = n_{R_0}$ for *each* local flux surface. Thus the solution of the equilibrium equation shows that in the presence of strong rotation the equilibrium density is no longer constant over a flux surface. This is a well known result [5, 47], set here in the context of the gyrokinetic ordering expansion.

The approximation $\langle\Phi\rangle \approx \Phi$ is made, since the background potential Φ is an equilibrium quantity, with variation only over large length scales. Φ is determined by applying the quasineutrality condition over all the species, which in the case of a pure hydrogenic plasma solves exactly to give

$$e\Phi = \frac{T_e T_i}{T_e + T_i}\left(\frac{m_i}{T_i} - \frac{m_e}{T_e}\right)\frac{\Omega^2}{2}(R^2 - R_0^2), \tag{2.58}$$

but in the general case of a multispecies plasma is calculated numerically (described in section Sec. 3.6). It is convenient to combine the centrifugal force and background potential in the (species dependent) centrifugal energy

$$\mathcal{E}(\theta) = Ze\Phi - \frac{1}{2}m\Omega^2(R^2 - R_0^2), \tag{2.59}$$

such that the equilibrium density variation can be written as an additional energy in the Maxwellian

$$F_M = \frac{n_{R0}}{(2\pi T/m)^{3/2}} \exp\left[-\frac{m(v_\parallel - u_\parallel)^2/2 + \mu B + \mathcal{E}}{T}\right]. \tag{2.60}$$

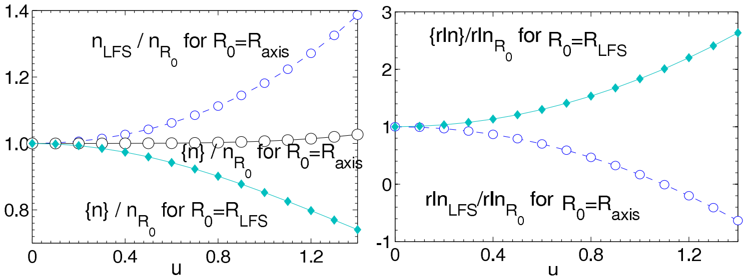

Figure 2.1: Comparison of density (left) and effective density gradient R/L_n^E (labelled rln, right) in a rotation scan for the GA-STD case with $R_0 = R_{\rm axis}$ (circles) and $R_0 = R_{\rm LFS}$ (diamonds). The flux surface average value is denoted by $\{\}$, and the value at the low field side midplane by LFS. The Mach number $u = R_A\Omega/v_{\rm th}$.

and $n_s(\theta,\psi) = n_{R_0,s}(\psi)\exp(-\mathcal{E}_s(\theta,\psi)/T_s(\psi))$ for each species. In the case of the pure hydrogenic plasma, it can be shown that $\mathcal{E}_i/T_i = \mathcal{E}_e/T_e$ (as it must be to satisfy quasineutrality) and neglecting the electron mass

$$\mathcal{E}_s \approx -\frac{T_s}{T_i + T_e}\frac{m_i}{2}\Omega^2(R^2 - R_0^2). \tag{2.61}$$

It must be noted that this redistribution of density in the Maxwellian will be different for each flux surface, with the result that the density gradient will also be modified by the centrifugal force. A choice must be made of where the input density and density gradient are defined. In GKW, the numerically convenient choice of a single major radius R_0 at which to define n_{R_0} and $R/L_n|_{R_0}$ is used. Two options are available: the magnetic axis $R_0 = R_{\rm axis}$, and the midplane of the flux surface at the low field side $R_0 = R_{\rm LFS}$. Whilst physical results are independent of the integration constant, the choice determines at which location the density and its gradient are held constant when scanning over rotation. The consequence of each choice for the density is shown in Fig. 2.1; the flux surface average density (denoted by $\{\}$) is nearly constant for $R_0 = R_{\rm axis}$, but not the density at the low field side midplane.

With the density variation over the flux surface, we define the local dimensionless density gradient as

$$\frac{R}{L_n^E}(\theta) = -\frac{1}{n}\frac{\partial n}{\partial \psi} = \frac{1}{T}\frac{\partial \mathcal{E}}{\partial \psi} + \frac{\mathcal{E}}{T}\frac{R}{L_T} + \left.\frac{R}{L_n}\right|_{R_0}, \tag{2.62}$$

(Other options such as $1/\{n\}(\partial n/\partial\psi)$ or $1/n_{R_0}(\partial n/\partial\psi)$ are evaluated in Sec. 3.6) where

$$\left.\frac{R}{L_n}\right|_{R0} = -\frac{1}{n_{R0}}\frac{\partial n_{R0}}{\partial \psi}, \tag{2.63}$$

is the dimensionless density gradient evaluated at R_0. For the cases presented later in

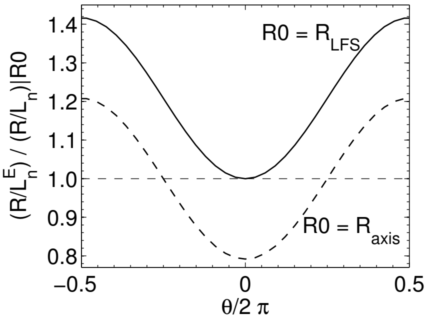

Figure 2.2: Flux surface variation in effective density gradient R/L_n^E with $R_0 = R_{\mathrm{LFS}}$ (solid), and $R_0 = R_{\mathrm{axis}}$ (dashed) for $u = 0.5$ and GA-STD parameters in $s-\alpha$ geometry.

this thesis, the term in Eq. (2.62) proportional to $\mathcal{E}$ dominates the term proportional to $\partial\mathcal{E}/\partial\psi$, but both are small compared to $R/L_n|R_0$ for the bulk species when $u < 0.5$.

For the simplified hydrogenic case Eq. (2.61), the effective density gradient modification can be shown to be

$$\frac{R}{L_n^E} - \frac{R}{L_n}\bigg|_{R_0} \approx \left(\frac{\partial T_e}{\partial\psi} + \frac{\partial T_i}{\partial\psi}\right)\frac{m_i\Omega^2(R^2 - R_0^2)}{2(T_e + T_i)^2} - \frac{m_i\Omega^2}{T_e + T_i}\left(R\frac{\partial R}{\partial\psi}\bigg|_\theta - R_0\frac{\partial R_0}{\partial\psi}\bigg|_\theta\right), \quad (2.64)$$

where the radial gradient of R_0 is kept in order that the density gradient keeps the usual property of being defined at constant θ. The parallel variation of R/L_n^E is plotted in Fig. 2.2.

For the ideal thought experiment in which rotation is varied independently of other plasma parameters, one preference might be to keep the total number of particles on a flux surface constant (the flux surface averaged density) with changing Ω. In practice, it is difficult to experimentally scan over rotation without varying the average density, and many diagnostic reconstructions use the assumption of a constant flux surface density. When studying ballooning modes in which the drive is localised on the low field side, it would be desirable to investigate the centrifugal effects irrespective of the density variation effects, in which case $R_0 = R_{\mathrm{LFS}}$ might be an appropriate choice. Since the dependencies of ITG mode and TEM turbulence on density and density gradient are well known [34, 76, 77], we would ideally like to examine the other consequences of the centrifugal terms. To this end, the choice $R_0 = R_{\mathrm{LFS}}$ is mostly used (unless stated otherwise) for the simulations presented in this thesis, with the assumption that it best minimises density variation alterations to the turbulence drive (insofar as this is possible). This choice also precludes the possibility of negative R/L_n^E, since the density gradient is at its minimum at the low field side (Fig. 2.2). For the rotation scans presented in Chapter 6, differences between $R_0 = R_{\mathrm{axis}}$ and $R_0 = R_{\mathrm{LFS}}$ have little bearing on the ITG modes, and for the TEM mode are not significant below $u = 0.6$.

The centrifugal force also modifies the solution of the Grad-Shafranov equation for the magnetic equilibrium, resulting in an increased outboard compression of the flux surfaces, commonly known as the Shafranov shift. The effects of the Shafranov shift on turbulence are an already known geometry effect [78–80]. The rotational Shafranov shift scales as βu^2, and is excluded in this thesis which deals with the electrostatic limit. For a complete description of all inertial effects, this effect could be included via coupling to an equilibrium solver which also includes rotation.

2.7.2 First order gyrokinetic equation

Continuing in the small parameter expansion, we next expand the gyrokinetic equation to order $\mathcal{O}(\rho_*)$. The equations of motion were evaluated using the Lagrangian of order $\mathcal{O}(\rho_*)$. For the conservation laws guaranteed by Noether's theorem in the Hamiltonian formulation to hold, no further terms should be discarded after the Lagrangian [54, 71, 72, 81].

Expanding the full gyrokinetic equation Eq. (2.51) into the δf formalism, and using the equation of motion Eq. (2.35) gives the gyrokinetic equation for the perturbed distribution

$$\begin{aligned}\frac{\partial f}{\partial t} + \frac{\mathrm{d}\mathbf{X}}{\mathrm{d}t}\cdot\nabla f - \frac{\mathbf{b}}{m}\cdot[Ze\nabla\langle\phi\rangle + \nabla P]\frac{\partial f}{\partial v_\parallel} - \overbrace{\frac{\mathbf{v}_D + \mathbf{v}_E}{mv_\parallel}\cdot[Ze\nabla\langle\phi\rangle + \nabla P]\frac{\partial f}{\partial v_\parallel}}^{\text{PVNL}} \\ = -(\mathbf{v}_D + \mathbf{v}_E)\cdot\nabla F_M + \frac{\mathbf{b}}{m}\cdot Ze\nabla\langle\phi\rangle\frac{\partial F_M}{\partial v_\parallel} + \frac{\mathbf{v}_D + \mathbf{v}_E}{mv_\parallel}\cdot[Ze\nabla\langle\phi\rangle + \nabla P]\frac{\partial F_M}{\partial v_\parallel},\end{aligned} \tag{2.65}$$

where

$$\nabla P = Ze\nabla\langle\Phi\rangle + \mu\nabla B - m\Omega^2 R\nabla R, \tag{2.66}$$

is a notational abbreviation for the trapping force, and the term $v_\parallel\mathbf{b}\cdot\nabla F_M$ has been cancelled with the term $(\mathbf{b}\cdot\nabla P/m)\partial F_M/\partial v_\parallel$ using the equilibrium condition Eq. (2.52).

The term labelled 'PVNL' contains what is known as the 'parallel velocity nonlinearity' which may be neglected as a $\mathcal{O}(\rho_*^2)$ term by the use of an additional ordering assumption on the velocity space derivatives

$$\frac{\partial f}{\partial v_\parallel} \sim \rho_*\frac{\partial F}{\partial v_\parallel}. \tag{2.67}$$

This ordering can be justified if the plasma is sufficiently collisional to smooth out fine-scale velocity space structures in the perturbed distribution faster than they arise through nonlinear phase-mixing. In the equations and simulations used for this thesis, this approximation *has* been made, with the consequence that the strict energy conservation guaranteed by the Hamiltonian formalism no longer applies, since this term is dropped *after* the truncation of the Lagrangian [71, 72, 81]. A number of investigations keeping this term [82–85] have shown that its effect on saturation levels is small for values of $\rho_* < 0.01$, justifying the ordering of Eq. (2.67) and the neglect of the term in a local code. The additional centrifugal terms in the PVNL are of the same order as the usual ones, so these arguments are still valid. The effect of the parallel velocity nonlinearity on long term nonlinear evolution is still an area of active research [54].

The spatial derivative of the Maxwellian evaluates as

$$\nabla F_M = \left[\frac{\nabla n_{R_0}}{n_{R_0}} + \left(\frac{v_\parallel^2}{v_{\rm th}^2} + \frac{(\mu B + \mathcal{E})}{T} - \frac{3}{2}\right)\frac{\nabla T}{T} + \frac{m v_\parallel R B_t}{BT}\nabla\omega_\varphi - \frac{\mu\nabla B}{T} - \frac{\nabla\mathcal{E}}{T}\right]F_M, \tag{2.68}$$

where $\nabla u_\parallel = RB_t/B\nabla\omega_\varphi$. The velocity derivative is simply

$$\frac{\partial F_M}{\partial v_\parallel} = -\frac{m v_\parallel}{T}F_M. \tag{2.69}$$

Substituting these derivatives into Eq. (2.65), one finds that the gradient terms containing ∇B and $\nabla\mathcal{E}$ (nearly) cancel with the $(\mathbf{v}_E\cdot\nabla P)\partial F_M/\partial v_\parallel$ term. This allows the gyrokinetic equation to be finally written as

$$\frac{\partial f}{\partial t} + \frac{\mathrm{d}\mathbf{X}}{\mathrm{d}t}\cdot\nabla f - \frac{\mathbf{b}}{m}\cdot(\mu\nabla B + \nabla\mathcal{E})\frac{\partial f}{\partial v_\parallel} = S, \tag{2.70}$$

where the source term is given by

$$\begin{aligned} S = & - \mathbf{v}_E\cdot\left[\frac{\nabla n_{R_0}}{n_{R_0}} - \frac{m\Omega^2}{T}R_0\left.\frac{\partial R_0}{\partial\psi}\right|_\theta\nabla\psi + \left(\frac{v_\parallel^2}{v_{\rm th}^2} + \frac{(\mu B + \mathcal{E})}{T} - \frac{3}{2}\right)\frac{\nabla T}{T} + \frac{m v_\parallel R B_t}{BT}\nabla\omega_\varphi\right]F_M \\ & - \frac{Ze}{T}\frac{\mathrm{d}\mathbf{X}}{\mathrm{d}t}\cdot\nabla\langle\phi\rangle F_M. \end{aligned} \tag{2.71}$$

The term containing $\partial R_0/\partial\psi$ is the only part of the term containing $\nabla\mathcal{E}\ F_M$ that does not cancel, and its additional appearance when compared to Ref. [57] is due to the allowance for the case $R_0 = R_{\rm LFS}$. When $R_0 = R_{\rm axis}$, $\partial R_0/\partial\psi|_\theta = 0$ in the simplest $(s-\alpha)$ model equilibrium. In Chapter 3, Eq. (2.70) is presented again in a form suitable for numerical implementation. The physical interpretation of each individual term is discussed in more detail in Sec. 3.5.

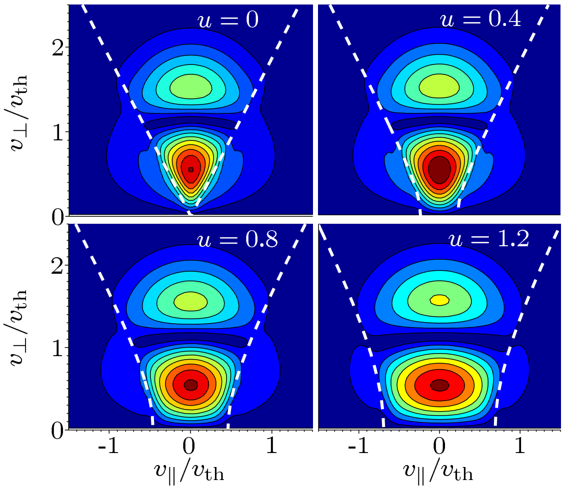

Figure 2.3: Magnitude of perturbed electron distribution in velocity space for the GKW-TEM case (see Chapter 6) at the outboard midplane with increasing Mach number $u = R_A\Omega/v_{\rm th}$. Arbitrary units, contours are equally spaced at same intervals for each plot. The trapping boundary of Eq. (2.72) is overplotted as a dashed line.

2.8 Centrifugal trapping

The modification to the trapping term in Eq. (2.70) means that the centrifugal trapping present in the equilibrium is also kept for the perturbed distribution. Following the same procedure used to derive Eq. (1.9), with the inclusion of the centrifugal energy $\mathcal{E}$, the centrifugal force leads to a modified trapping condition, in which particles are trapped if

$$v_\perp^2 > \frac{v_\parallel^2 - \frac{2}{m}(\mathcal{E}_{\rm H} - \mathcal{E}_{\rm L})}{\frac{B_{\rm H}}{B_{\rm L}} - 1}, \tag{2.72}$$

where the subscripts H and L refer to the high and low field sides respectively. Example evaluations of the modified trapping condition are overplotted in Fig. 2.3.

Using Eq. (2.61) and the simplification of concentric circular flux surfaces the trapping condition for both species becomes

$$\frac{v_{\perp,s}^2}{v_{th,s}^2} > \left[\frac{v_{\parallel,s}^2}{2\epsilon v_{th,s}^2} - \frac{2T_i}{T_i + T_e}u^2\right](1-\epsilon), \tag{2.73}$$

where $\epsilon = r/R_A = \psi$ is the inverse aspect ratio of the flux surface. We point out that the enhanced trapping on the electrons is due to the background potential, not the direct effect of the centrifugal force on the electrons. For the ions, the combination of the detrapping from the background potential and the trapping from the centrifugal force partially cancel, resulting in the identical trapping condition (and trapped fraction) for both species.

2.9 Gyrokinetic Poisson equation

The gyrokinetic Vlasov equation must be combined with field equations to form a closed system of equations. In deriving Eq. (2.70), magnetic field fluctuations were neglected appropriate to the limit of low β, so only an equation for the electrostatic field is required to close the system. Whilst this equation is often called the 'gyrokinetic Poisson equation', the equation solved is actually the constraint of neutrality

$$\sum_s Z_e n_s(\mathbf{x}) = 0, \tag{2.74}$$

where the sum is over all species. In reality, the charge density is not exactly zero, but it is assumed to be zero over the quasineutral length and timescales at which gyrokinetics is valid. By assuming zero charge density, the actual Poisson equation cannot be used to find the field and so is replaced by the quasineutrality closure. With the quasineutrality constraint, the Laplacian operator need not be inverted to find the field, which greatly simplifies the solution. The chief complication then in solving this equation is that the densities must be computed in physical particle phase space $(\mathbf{x}, \mathbf{v})$, not in the gyrocentre phase space in which the gyrokinetic equation is formulated [86]. In gyrocentre phase space quasineutrality is represented as

$$\bar{\varrho}(\mathbf{X}) + \varrho_{\text{pol}}(\mathbf{X}) = 0, \tag{2.75}$$

where $\bar{\varrho}$ is the gyrocentre charge density and $\varrho_{\text{pol}} = -\nabla \cdot P_{\text{gy}}$ is the gyrocentre polarisation density, with P_{gy} the gyrocentre polarisation vector. The gyrocentre polarisation density describes the difference between the actual charge density and the charge density of gyrocentres at a given point, which may be pictured as the Boltzmann density response of the gyrocentres due to the average variation in the potential over a gyro-orbit, $\phi(\mathbf{x}) - \langle\phi\rangle(\mathbf{X})$. This can also be understood as the consequence of the polarisation drift Eq. (1.6) averaged over the gyro-orbit timescale.

To close the gyrokinetic Vlasov-Poisson system, a model for polarisation must be adopted which is consistent with the formulation of the gyrokinetic equation. If the field equations are obtained by variational principles from the same symplectic Lagrangian / Hamiltonian used to derive the equations of motion, then energy consistency can be guaranteed by including the next higher order energies in the field terms [54, 71, 72, 81]. The system Lagrangian is obtained by integrating the gyrocentre particle Lagrangian Γ Eq. (2.27) over all of phase space

$$L = \sum_s \int \mathrm{d}^3\mathbf{v} \int \mathrm{d}^3\mathbf{x}\; f_{\text{tot}}\Gamma. \tag{2.76}$$

The field equation for ϕ is derived from this system Lagrangian by taking the functional derivative [87] of this system Lagrangian with respect to $\delta\phi$. Since Γ is in symplectic form, all dependence on the fields is contained in the Hamiltonian and the field equation may be written

$$\sum_s \frac{\delta(f_{\mathrm{tot}} H)}{\delta\phi} = 0. \tag{2.77}$$

For a consistent system, one order further must be kept in H than was used for the equations of motion [54, 71, 72, 81]. In the δf formulation, the field equation may be written as

$$\sum_s \frac{\delta[(F_M + f)(H_0 + H_1)]}{\delta\phi} = -\sum_s \frac{\delta[F_M H_2]}{\delta\phi}, \tag{2.78}$$

which contains the simplest model of linearised polarisation. For the functional derivative, only the field dependent part of the Hamiltonian $H_E = H_{01E} + H_{2E}$ is required, with

$$H_{01E} = Ze\langle\phi\rangle, \qquad H_{2E} = \frac{Z^2e^2}{2T}\left(\langle\phi\rangle^2 - \phi^2\right), \tag{2.79}$$

where the first order part comes from Eq. (2.28), and the second order part is as used in other codes [72], and represents physically the kinetic energy in the $\mathbf{v}_E$ drift with a Taylor approximation for the gyroaverage operator. H_E is therefore a function of ϕ and its gyroaverage $G\phi \equiv \langle\phi\rangle$ only, which are treated as separate variables for the purposes of the functional derivative. The exact form of the gyroaverage operator G will be demonstrated in Sec. 3.4, here it is sufficient to know that it is a spatially Hermetian operator. In this simple case then, all the functions of ϕ commute through the spatial integral in the system Lagrangian (and thus through the δ operator), and the functional derivative may be written

$$\sum_s \int \mathrm{d}^3\mathbf{v}\left[(F_M + f)\frac{\partial H_{01E}}{\partial G\phi}\delta G\phi + F_M\frac{\partial H_{2E}}{\partial\phi}\delta\phi + F_M\frac{\partial H_{2E}}{\partial G\phi}\delta G\phi\right] = 0, \tag{2.80}$$

since $\partial H_{01E}/\partial\phi = 0$. Evaluating the nonzero derivatives and commuting the operator G leads to

$$\sum_s \int \mathrm{d}^3\mathbf{v}\left[Z_s e(GF_M + Gf) + \frac{Z_s^2e^2}{T_s}\left(F_M\phi - GF_M G\phi\right)\right]\delta\phi = 0. \tag{2.81}$$

The F_M in the first term is a background quantity on which the gyroaverage G has no effect. Performing the velocity space integral over this term yields the charge density Zen_s, which becomes zero when summed over the species. The field equation can then be written as

$$\sum_s \int \mathrm{d}^3\mathbf{v}\left[Z_s e G f(\mathbf{X}) + F_M\frac{Z_s^2e^2}{T_s}(1 - G^2)\phi(\mathbf{x})\right] = 0. \tag{2.82}$$

This equation is used to calculate the potential at a point $\mathbf{x}$ in real space. The first term represents the gyrocentre charge density $\bar{\varrho}$ integrated over all gyrocentres passing through $\mathbf{x}$ whilst the second represents the linearised gyrocentre polarisation density ϱ_{pol} for all the gyro-orbits passing through $\mathbf{x}$ (which is why the G operator acts twice on ϕ). These physical interpretations, may be seen more clearly in the alternative derivation which starts from quasineutrality in the real phase space; however, this requires full knowledge of the transformation to the gyrocentre phase space which is defined by the Lie transforms [54]. In Sec. 3.5, this equation is rewritten in a form suitable for an efficient numerical implementation, which allows the operator G to be evaluated over the velocity space integral.

2.10 Summary

This chapter introduced the gyrokinetic formalism and used a modern variational approach to derive the δf gyrokinetic Vlasov equation and gyrokinetic Poisson equation from a gyrocentre Lagrangian. The equations are formulated in the comoving frame that rotates with the plasma, which in the local limit allows the effects of rotation to appear as inertial terms resulting from the centrifugal and Coriolis forces. The equations presented here (and also in Refs. [55, 88, 89]) differ from the equations in other gyrokinetic derivations and codes in the use of a strong rotation ordering which treats plasma toroidal rotation with Mach numbers of order unity. With this ordering, the centrifugal force leads to a modified equilibrium with an enhanced trapping force, as well as an additional drift.

Taken together, Eqs. (2.44), (2.60), (2.70), (2.71), and (2.82) form a closed set of equations describing local electrostatic drift wave turbulence in a tokamak core plasma in the collisionless limit, and contain all modifications that arise from the inclusion of the centrifugal force. These are the equations solved by the GKW code for the results presented later in this thesis, and details of their numerical implementation are presented in the next chapter.

Chapter 3

Gyrokinetic numerics

3.1 Introduction

In Chapter 2 the gyrokinetic Vlasov equation for a strongly rotating tokamak plasma was derived in the collisionless electrostatic limit, and the gyrokinetic Poisson equation was introduced. In this chapter we write these equations in a form suitable for an efficient numerical implementation, as used in the GKW code. Much of the material in this chapter is adapted directly from Ref. [58], with the centrifugal terms added for this thesis. In addition to these new inclusions, the author of this thesis contributed a number of corrections and improvements to clarity and presentation during the preparation of Ref. [58], as a co-author. The author of this thesis has complete authorship of Sections 3.4.1, 3.6, and 3.8, but does not claim primary authorship of any other section in this chapter.

3.2 Normalisations

All quantities in the GKW code are made dimensionless by means of normalisation with a reference quantity. We define a reference mass m_{ref}, a reference thermal velocity v_{thref}, a reference density n_{ref}, a reference temperature T_{ref}, a reference vacuum magnetic field B_{ref} evaluated on the magnetic axis, a reference gyroradius ρ_{ref} and a reference major radius R_{ref} which is usally taken to be R_A.

The reference quantities are related since

$$T_{\mathrm{ref}} = \frac{1}{2} m_{\mathrm{ref}} v_{\mathrm{thref}}^2, \qquad \rho_{\mathrm{ref}} = \frac{m_{\mathrm{ref}} v_{\mathrm{thref}}}{e B_{\mathrm{ref}}}. \tag{3.1}$$

We also define a normalised Larmor radius to be

$$\rho_* = \rho_{\mathrm{ref}} / R_{\mathrm{ref}}. \tag{3.2}$$

Time t, magnetic field B, angular rotation frequency Ω, and the major radius R, may then be made dimensionless using the reference values

$$\begin{aligned} t &= R_{\text{ref}} t_N / v_{\text{thref}}, & B &= B_{\text{ref}} B_N, \\ \Omega &= v_{\text{thref}} \Omega_N / R_{\text{ref}}, & R &= R_{\text{ref}} R_N, \end{aligned} \tag{3.3}$$

where the index N refers to a normalised quantity. The reference values are also used to define, for each species, a dimensionless mass m_R, a dimensionless thermal velocity v_R, a dimensionless density n_R, a dimensionless temperature T_R, and a dimensionless centrifugal energy $\mathcal{E}_R$

$$m_R = \frac{m}{m_{\text{ref}}}, \qquad v_R = \frac{v_{\text{th}}}{v_{\text{thref}}}, \qquad n_R = \frac{n_{R_0}}{n_{\text{ref}}}, \qquad T_R = \frac{T}{T_{\text{ref}}}, \qquad \mathcal{E}_R = \frac{\mathcal{E}}{T_R T_{\text{ref}}}. \tag{3.4}$$

The velocity space coordinates are made dimensionless with the thermal velocity for each species independently

$$v_\parallel = v_{\parallel N} v_{\text{th}}, \qquad \mu = \frac{m v_{\text{th}}^2}{B_{\text{ref}}} \mu_N, \tag{3.5}$$

such that the normalised values on the velocity grid are the same for each species. It is then convenient to normalise the distribution functions according to

$$f = \rho_* \frac{n_{R_0}}{v_{\text{th}}^3} f_N, \qquad F_M = \frac{n_{R_0}}{v_{\text{th}}^3} F_{MN}. \tag{3.6}$$

The potential is made dimensionless using the reference temperature

$$\phi = \rho_* \frac{T_{\text{ref}}}{e} \phi_N, \qquad \Phi = \frac{T_{\text{ref}}}{e} \Phi_N. \tag{3.7}$$

The factor of ρ_* has been added in the definition of the normalised perturbed fields and distribution function so that the normalised quantities are all of order $\mathcal{O}(\rho_*)$, under the orderings described in Chapter 2.

The gradient of density and temperature are made dimensionless using the density and temperature of the species for each species individually, but the plasma rotation is largely a bulk motion of all the species together and its gradient is normalised using the reference thermal velocity v_{thref}

$$\frac{1}{L_{n,N}} = \frac{R_{\text{ref}}}{L_n} = -\frac{1}{n_{R_0}} \frac{\partial n_{R_0}}{\partial \psi}, \qquad \frac{1}{L_{T,N}} = \frac{R_{\text{ref}}}{L_T} = -\frac{1}{T} \frac{\partial T}{\partial \psi}, \qquad u'_N = -\frac{R_{\text{ref}}}{v_{\text{thref}}} \frac{\partial \omega_\varphi}{\partial \psi}. \tag{3.8}$$

The gradient length scales are normalised with R_{ref}, but note that the same quantities are often written as R/L_n and R/L_T elsewhere in the literature. The dimensionless radial coordinate ψ is also normalised with R_{ref}:

$$\psi = \frac{R_{\mathrm{max}} - R_{\mathrm{min}}}{2R_{\mathrm{ref}}}, \tag{3.9}$$

where R_{max} (R_{min}) is the maximum (minimum) major radius of the flux surface. For circular flux surfaces, for instance, $\psi = r/R_{\mathrm{ref}} = \epsilon$, where r is the minor radius. The gradient operator on all quantities in all directions is normalised using the major radius R_{ref},

$$\nabla = \frac{1}{R_{\mathrm{ref}}}\nabla_N. \tag{3.10}$$

All fluctuating quantities are represented in the perpendicular direction by a spectral representation. The wavevectors introduced in the spectral representation (described in Sec. 3.4) arise from the perpendicular gradient of a fluctuating quantity and are normalised by ρ_{ref}

$$k = \frac{k_N}{\rho_{\mathrm{ref}}}, \tag{3.11}$$

which when compared with the gradient normalisation causes a factor of ρ_* to be absorbed when a perpendicular gradient is converted to Fourier space. Under the orderings described in Chapter 2, this ensures perpendicular gradients of fluctuating quantities to remain of $\mathcal{O}(\rho_*)$ in the normalised units.[1]

Finally, the poloidal flux Ψ used in the derivation of the metric tensors is normalised according to

$$\Psi_p = R_{\mathrm{ref}}^2 B_{\mathrm{ref}} \Psi_{p,N}. \tag{3.12}$$

In the rest of this chapter the equations are presented in their normalised form and the subscript N is dropped for convenience.

The reference quantities do not appear anywhere in the code, which operates only in the dimensionless units. The user must have in mind values for the reference quantities in order to provide sensible code input and to interpret the code output (both of which occur in normalised form). In practice, the reference values will usually be chosen to be practical values, with m_{ref} often chosen equal to be the bulk ion mass, T_{ref} the ion (or electron) temperature, n_{ref} the equilibrium electron density on the flux surface, and R_{ref} the major radius of the magnetic axis. B_{ref} is always the toroidal magnetic field at the magnetic axis. The dimensionless quantity ρ_* also does not appear in the code, but it is used in the code normalisations to relate perpendicular and parallel derivatives consistently with the orderings introduced in Chapter 2.

---

[1] The same result could alternatively be achieved by normalising the perpendicular gradients of fluctuating quantities with ρ_{ref}.

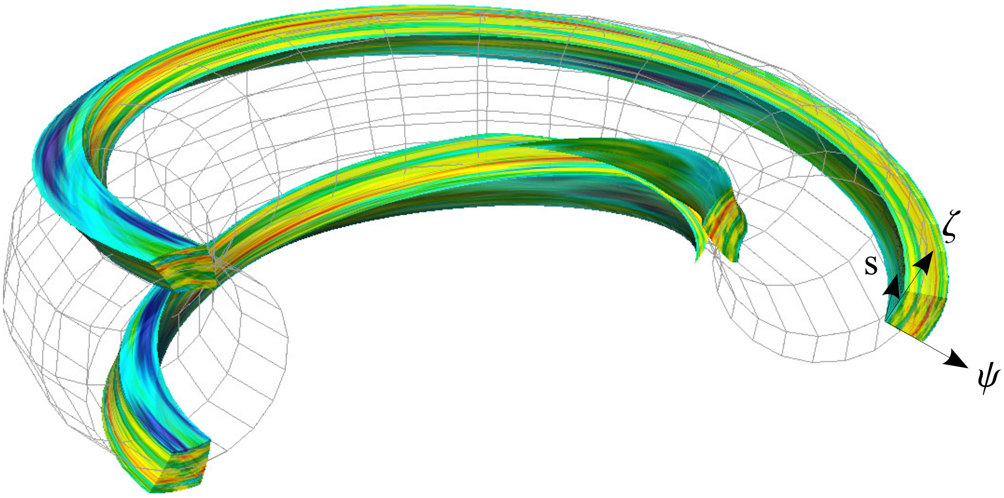

Figure 3.1: Flux tube domain and field aligned coordinates on a circular flux surface with $q = 2$, $\hat{s} = 1$ and $\epsilon = r/R = 0.29$.

3.3 Geometry

In GKW, the local limit introduced in Sec. 2.3 is used in conjunction with a field aligned coordinate system, in which a parallel coordinate s parametrises a field line, and the other two (non-orthogonal) coordinates (radial (ψ) and binormal-axisymmetric (ζ)) are perpendicular to the field. The local limit in field aligned coordinates thus represents a 'flux tube' bounded by four field lines (Fig. 3.1) in which the effect of the magnetic shear is incorporated in the coordinate system. The parallel boundary is treated with a shifted-periodic boundary condition which preserves both poloidal and toroidal periodicity. The flux tube geometry tailors the simulation domain to the $k_\parallel \ll k_\perp$ structure of the turbulence, whilst also allowing a reduction of the simulation volume by exploitation of the axisymmetry.

GKW is formulated in straight field line (Hamada) coordinates [90], in which the contravariant components of the magnetic field, B^s and B^γ, are both flux functions. The safety factor is then determined by the ratio $q = B^\gamma/B^s$. Starting from an orthogonal coordinate system (ψ, θ, φ), where ψ is the radial coordinate (i.e. $\mathbf{B}\cdot\nabla\psi = 0$), θ is the poloidal angle (upward on the outboard midplane), and φ is the toroidal angle (clockwise when viewed from above), and using the transformations

$$s = s(\psi, \theta), \qquad \gamma = \gamma(\psi, \theta, \varphi), \tag{3.13}$$

one can derive [91, 92]

$$s(\theta,\psi) = \int_0^\theta \frac{\mathrm{d}\theta'}{\mathbf{B}\cdot\nabla\theta'} \bigg/ \oint \frac{\mathrm{d}\theta'}{\mathbf{B}\cdot\nabla\theta'}, \tag{3.14}$$

$$\gamma = \frac{\varphi}{2\pi} + s_\mathrm{B}\frac{RB_t}{2\pi}\int_0^\theta \frac{\mathrm{d}\theta'}{\mathbf{B}\cdot\nabla\theta'}\left[\left\{\frac{1}{R^2}\right\} - \frac{1}{R^2}\right], \tag{3.15}$$

with

$$B^s = 1\bigg/\oint \frac{\mathrm{d}\theta'}{\mathbf{B}\cdot\nabla\theta'} \qquad B^\gamma = s_\mathrm{B}\frac{RB_t}{2\pi}\left\{\frac{1}{R^2}\right\}. \tag{3.16}$$

In the equations above, the magnetic field is decomposed as

$$\mathbf{B} = s_\mathrm{B}RB_t\nabla\varphi + s_\mathrm{j}\nabla\varphi\times\nabla\Psi, \tag{3.17}$$

where $B_t > 0$ is the toroidal component of the magnetic field, $s_\mathrm{B} = \pm 1$ and $s_\mathrm{j} = \pm 1$ the sign of the magnetic field and plasma current (positive in the direction of $\nabla\varphi$) and Ψ the normalised poloidal flux ($\nabla\Psi$ points from the magnetic axis to the plasma edge). The brackets $\{\}$ denote the flux surface average, (the limit of the volume average between two flux surfaces as the distance between them goes to zero) which in the transformed coordinates can be written simply as

$$\{g\} = \oint g\,\mathrm{d}s. \tag{3.18}$$

The normalising constants have been chosen such that the domain [-1/2,1/2] in s corresponds to one poloidal turn and the domain [-1/2,1/2] in γ corresponds to one toroidal turn. The transformations of Eq. (3.13) leave the angle γ to be an ignorable (axisymmetric) coordinate, since any quantity that is independent of φ will also be independent of γ after the transformation.

The (s,γ,ψ) coordinates are then transformed again using a simple linear transformation

$$\zeta = qs - \gamma \qquad \text{where} \qquad q = \frac{B^\gamma}{B^s}, \tag{3.19}$$

to make them field aligned, i.e. $B^\zeta = 0$ and $B^\psi = 0$. The field line is parametrised only by s, such that any derivative taken along the field requires only a derivative in the s direction, and may be written as

$$\mathbf{B}\cdot\nabla = B^s\frac{\partial}{\partial s}. \tag{3.20}$$

Note however that this does not mean that ∇s is in the direction of the field.

The coordinate transformation above flips the sign of the toroidal angle, and the right handed coordinate system can therefore be defined as (ψ,ζ,s). The

Jacobian of the new coordinate system can be expressed in terms of the original Jacobian through

$$J_{\psi\zeta s} = 2\pi\mathbf{B}\cdot\nabla\theta \oint \frac{\mathrm{d}\theta'}{\mathbf{B}\cdot\nabla\theta'} J_{\psi\theta\varphi}. \tag{3.21}$$

We note here that the coordinates ψ, s and ζ are all dimensionless with ψ being a normalised 'minor radius' of the flux surface, see Eq. (3.9). ζ, being the axisymmetric coordinate, has much in common with the toroidal angle. However in the large aspect ratio approximation, the direction of $\nabla\zeta$ is often almost poloidal. We shall refer to ζ as the 'binormal' coordinate to avoid this ambiguity (note that binormal may also be misleading; ζ and ψ are both normal to $\mathbf{b}$, but are only normal to each other at $s = 0$).

The coordinates defined above are used in GKW to define a number of geometric tensors used for evaluating the vector calculus operators that appear in the equations. First, we note that the gyrokinetic equation contains parallel derivatives which are expressed in the tensor

$$\mathbf{b}\cdot\nabla = \mathcal{F}\frac{\partial}{\partial s} \quad \Rightarrow \quad \mathcal{F} = \frac{B^s}{B}. \tag{3.22}$$

For perpendicular drifts, which involve a cross product with the magnetic field, we define the tensor

$$\mathcal{E}^{\alpha\beta} = \frac{1}{2B}(\nabla x_\alpha \times \nabla x_\beta)\cdot\mathbf{b} = \frac{1}{2B}(\mathbf{b}\times\nabla x_\alpha)\cdot\nabla x_\beta. \tag{3.23}$$

The convection connected with the velocity $\mathbf{v}_E$ can then be directly expressed using this tensor as

$$\mathbf{v}_E\cdot\nabla f = \frac{\partial\phi}{\partial x_\alpha}\frac{\partial f}{\partial x_\beta}\mathcal{E}^{\alpha\beta}, \tag{3.24}$$

where the Einstein summation convention implies summation over repeated indices. The antisymmetry $\mathcal{E}^{\alpha\beta} = \mathcal{E}^{\beta\alpha}$ may be used to simplify evaluation of this term. It is also worth noting that the magnetic field can be expressed as

$$\mathbf{B} = 2\pi s_{\mathrm{j}}\nabla\Psi\times\nabla\zeta, \tag{3.25}$$

which immediately leads to

$$\mathcal{E}^{\psi\zeta} = \frac{s_{\mathrm{j}}}{4\pi}\frac{\partial\psi}{\partial\Psi}, \tag{3.26}$$

showing that $\mathcal{E}^{\psi\zeta}$ is constant on a flux surface. We also define

$$\mathcal{D}^{\alpha} = -2\mathcal{E}^{\alpha\beta}\frac{1}{B}\frac{\partial B}{\partial x_\beta} = \frac{\mathbf{b}\times\nabla B}{B}\cdot\nabla x_\alpha, \qquad \mathcal{G} = \mathcal{F}\frac{\partial\ln B}{\partial s}, \tag{3.27}$$

with $\mathcal{D}$ related to the ∇B drift, and $\mathcal{G}$ to the trapping. The Coriolis and centrifugal drifts will enter the equations through the one forms $\mathcal{H}$ and $\mathcal{I}$ respectively

$$\mathcal{H}^{\alpha} = -\frac{s_{\rm B}}{B\Omega}\mathbf{\Omega}_{\perp}\cdot\nabla x_{\alpha}, \qquad \mathcal{I}^{\alpha} = \frac{s_{\rm B}}{2B}(\nabla x_{\alpha}\times\nabla R^2)\cdot\mathbf{b}, \tag{3.28}$$

and the centrifugal potential is calculated (see Sec. 3.6) using the quantities

$$\mathcal{J} = R^2 - R_0^2, \qquad \mathcal{K} = \left.\frac{\partial\mathcal{J}}{\partial\psi}\right|_s, \qquad \mathcal{L} = \left.\frac{\partial(R_0^2)}{\partial\psi}\right|_s. \tag{3.29}$$

Finally, for transformations of the shearing rate we also define

$$\mathcal{M} = \frac{\partial^2\Psi}{\partial\psi^2} = \frac{s_{\rm j}}{4\pi}\frac{\partial}{\partial\psi}\left(\frac{1}{\mathcal{E}^{\psi\zeta}}\right). \tag{3.30}$$

The tensor elements defined above are defined in their normalised form, in which they all have similar magnitude. These elements, however, are multiplied with the derivatives towards the respective coordinate. Since the derivatives along the field are much smaller than the derivatives in the perpendicular plane, these quantities do not enter at first order, so the tensor elements containing the coordinate s are neglected (i.e. $\mathcal{D}^s = \mathcal{E}^{s\psi} = \mathcal{E}^{s\zeta} = \mathcal{H}^s = 0$), except in the case where $\mathcal{E}^{s\psi}$ or $\mathcal{E}^{s\zeta}$ is multiplied with the background potential Φ.

In Chapter 2, we described the flux tube local limit, in which the turbulence is assumed homogeneous in the plane perpendicular to the magnetic field, and periodic boundary conditions are used. GKW uses this limit, and all background plasma parameters are assumed homogeneous across the simulation domain perpendicular to the field. Therefore there is no dependence of the geometry parameters on the coordinates ζ and ψ, and only the dependence of equilibrium quantities on the 'parallel' coordinate s are kept. All the tensors $\mathcal{D},\mathcal{E},\mathcal{F},\mathcal{G},\mathcal{H},\mathcal{I},\mathcal{J},\mathcal{K},\mathcal{M}$ as well as the metric tensor, are therefore functions of the parallel coordinate s only.

GKW currently implements three different geometry models to evaluate these tensors: A simplified '$s-\alpha$' equilibrium [93], an improved circular equilibrium [94], and a generalised tokamak equilibrium via an interface to the Grad-Shafranov equilibrium solver CHEASE [95].

3.3.1 s-α

The '$s-\alpha$' equilibrium (with $\alpha = 0$) is the simplest choice for the geometry of a tokamak, in which the flux surfaces are concentric circles, and only the lowest order in an $\epsilon = r/R_A$ expansion is kept in the definition of all the tensors. The coordinates can then be approximated as

$$\psi = \epsilon = \frac{r}{R}, \qquad \zeta = \frac{s_{\mathrm{B}} s_{\mathrm{j}}}{2\pi}[|q|\theta - \varphi], \qquad s = \frac{\theta}{2\pi}, \tag{3.31}$$

with the (normalised) gradients

$$\nabla\psi = \mathbf{e}_r, \qquad \nabla\zeta = \frac{s_{\mathrm{B}} s_{\mathrm{j}}|q|}{2\pi\epsilon}[\mathbf{e}_\theta + \hat{s}\theta\mathbf{e}_r], \qquad \nabla s = \frac{1}{2\pi\epsilon}\mathbf{e}_\theta, \tag{3.32}$$

where $\hat{s} = (r/q)\mathrm{d}q/\mathrm{d}r$ is the magnetic shear. Note that the gradient of the toroidal angle is ordered small compared with the gradient of the poloidal angle (times q) and is neglected in the gradient of ζ. The contravariant components of the magnetic field are

$$B^s = s_{\mathrm{j}}\frac{B_p}{2\pi r} \qquad B^\zeta = -s_{\mathrm{B}}\frac{B_t}{2\pi R}, \tag{3.33}$$

where B_p (B_t) is the poloidal (toroidal) magnetic field. The gradient of the magnetic field strength is assumed to be in the direction of ∇R and the drift term is approximated as

$$\mathbf{B} \times \nabla B = -s_{\mathrm{B}} B^2[\cos\theta\mathbf{e}_\theta + \sin\theta\mathbf{e}_r]. \tag{3.34}$$

Using these expressions one can evaluate the tensors to be

$$\mathcal{F} = \frac{s_{\mathrm{j}}}{2\pi|q|}, \qquad \mathcal{I}^\psi = \mathcal{H}^\psi = \mathcal{D}^\psi = -s_{\mathrm{B}}\sin(2\pi s), \tag{3.35}$$

$$\mathcal{I}^\zeta = \mathcal{H}^\zeta = \mathcal{D}^\zeta = -\frac{s_{\mathrm{j}}|q|}{2\pi\epsilon}[\cos(2\pi s) + 2\pi\hat{s}s\sin(2\pi s)], \tag{3.36}$$

$$\mathcal{J} = 2\epsilon\cos(2\pi s), \qquad \mathcal{K} = 2\cos(2\pi s) - \mathcal{L}, \qquad \mathcal{M} = \frac{1}{q} - \frac{\hat{s}}{q}, \tag{3.37}$$

where the two choices $R_0 = R_{\mathrm{axis}}$ and $R_0 = R_{\mathrm{LFS}}$ give

$$R_0 = 1 \Rightarrow \mathcal{L} = 0, \qquad R_0 = 1 + \epsilon \Rightarrow \mathcal{L} = 2, \tag{3.38}$$

respectively. Finally the nonzero metric elements $g^{\alpha\beta} = \nabla x_\alpha \cdot \nabla x_\beta$ are

$$g^{\zeta\zeta} = \left(\frac{q}{2\pi\epsilon}\right)^2 + \left(\frac{q}{\epsilon}\hat{s}s\right)^2, \qquad g^{\psi\zeta} = g^{\zeta\psi} = \frac{s_{\mathrm{B}} s_{\mathrm{j}}|q|}{\epsilon}\hat{s}s, \qquad g^{\psi\psi} = 1. \tag{3.39}$$

3.3.2 Circular geometry

The s–α model has been shown to have inconsistencies arising from the identification of the parallel coordinate s with the poloidal angle θ, leading to an inconsistent treatment of different terms, when only the first order in ϵ is kept [94]. These inconsistencies can lead to quite a substantial difference in results when compared to a numerical equilibrium or an improved analytic equilibrium [94, 96, 97]. We also find that for some nonlinear runs the $s-\alpha$ geometry can result in numerically unstable zonal flows [89]. In GKW the improved ad-hoc circular equilibrium model of Ref. [94] which addresses these deficiencies is also implemented.

As with the $s-\alpha$ model, the starting assumption of the model is that the flux surfaces are circular and concentric with the poloidal flux being a function of the radial coordinate only $\Psi = \Psi(r)$. This is a valid assumption in the case of small ϵ and small β. It simply means that the terms of order ϵ^2 are neglected and that the Shafranov shift is considered to be of order ϵ^2. As in the $s-\alpha$ model, the tensors are evaluated only to first order in ϵ, but to ensure consistent ordering this truncation is made only at the end of any manipulations.

The second assumption of the model is that the radial derivative of the poloidal flux is given by

$$\frac{\partial \Psi}{\partial r} = \frac{r B_{\rm ref}}{q\sqrt{1-\epsilon^2}}. \tag{3.40}$$

Here we do not list the derivation or calculation of all the tensor quantities, but only those that were added for the work of this thesis (those related to the centrifugal effects and the $E \times B$ shearing). For evaluation of all the geometric quantities in the circular model, we refer the reader to [59]. The tensor related to the centrifugal drift can be expressed as

$$\mathcal{I}^{\alpha} = s_{\rm j} \frac{2\pi}{B_N^2} \frac{\epsilon(1+\epsilon\cos\theta)}{|q|\sqrt{1-\epsilon^2}} \left[g_N^{\epsilon\alpha} \left[\cos\theta \frac{\partial \zeta}{\partial \epsilon} - s_{\rm B} s_{\rm j} \frac{|q|}{2\pi\epsilon} \frac{\sin\theta\sqrt{1-\epsilon^2}}{1+\epsilon\cos\theta} \right] - g_N^{\zeta\alpha} \cos\theta \right]. \tag{3.41}$$

We also have

$$\mathcal{M} = \frac{1}{q\sqrt{1-\epsilon^2}} \left(1 - \frac{\epsilon}{1-\epsilon^2} - \frac{\hat{s}}{q} \right). \tag{3.42}$$

Finally, the elements used to calculate the centrifugal potential are

$$\mathcal{J}_N = (1+\epsilon\cos\theta)^2 - \frac{R_0^2}{R_{\rm ref}^2}, \qquad \mathcal{K}_N = \frac{\partial \mathcal{J}_N}{\partial \epsilon} = 2\cos\theta(1+\epsilon\cos\theta) - \mathcal{L}_N, \tag{3.43}$$

where

$$\frac{1}{R_{\rm ref}} \frac{\partial R_0}{\partial \epsilon}\bigg|_s = \cos(\theta) + \frac{\epsilon\sin^2(\theta)}{1+\epsilon\cos(\theta)}, \tag{3.44}$$

such that the two choices for R_0 (magnetic axis value or $R(s=0)$) give

$$R_0 = R_{\rm ref} \Rightarrow \mathcal{L}_N = 2\epsilon, \quad R_0 = (1+\epsilon) R_{\rm ref} \Rightarrow \mathcal{L}_N = 2(1+\epsilon), \tag{3.45}$$

respectively.

3.4 Spectral representation

In the flux tube local limit, the turbulence is considered homogeneous in the perpendicular directions, such that periodic boundary conditions can be employed, and a discrete Fourier decomposition can be used.

The equations are then written in Fourier space, in which perpendicular derivatives are evaluated algebraically. For the nonlinear terms, a pseudospectral method is used, in which the velocity $\mathbf{v}_E$ and ∇f are calculated in Fourier space, transformed to real space where they are multiplied, before their product is finally transformed back into Fourier space. This approach allows exploitation of the efficiency of Fast Fourier Transform algorithms.

In what follows a $\widehat{\cdot}$ indicates the Fourier representation of a quantity and $\mathcal{T}$ and $\mathcal{T}^{-1}$ represent the forward and inverse discrete Fourier transform operations (DFT), respectively. The DFT used in GKW is defined as

$$f(\psi,\zeta,s) = \sum_{k_\zeta k_\psi} \hat{f}(k_\psi,k_\zeta,s)\exp[\mathrm{i}k_\zeta\zeta/\rho_* + \mathrm{i}k_\psi\psi/\rho_*] = \mathcal{T}^{-1}(\hat{f}), \tag{3.46}$$

where the factor of ρ_* has been added in the definition so that

$$\mathcal{T}\left(\rho_*\frac{\partial f}{\partial x_\alpha}\right) = \mathrm{i}k_\alpha\hat{f}, \tag{3.47}$$

as is consistent with the normalisations and orderings already discussed. The finite number of modes used in a discrete Fourier transform (in contrast to the continuous Fourier transform), set both a largest and smallest scale that can be represented on this basis. The natural way to remove the largest scales in this representation is through the periodicity condition

$$\psi = \psi + L_x, \qquad L_x = \frac{2\pi\rho_*}{k_{\psi,\mathrm{min}}}, \tag{3.48}$$

(and similarly for the ζ direction). With this condition, most of the desirable algebraic properties of the continuous Fourier transform (and specifically, Eq. (3.47)) are retained (discussed further in Sec. 4.2).

The periodicity of the torus, however, is not automatically satisfied. The condition of toroidal periodicity can be formulated as

$$f(\psi,\zeta+1,s) = f(\psi,\zeta,s) \quad\Rightarrow\quad \frac{k_\zeta}{2\pi\rho_*} = N, \tag{3.49}$$

where N is an integer [17, 98]. Since ρ_* is small, this condition can in general be satisfied with very small changes to k_ζ or ρ_*, and is equivalent to the condition that the toroidal modenumber is large (which is used in the ballooning representation below). In the local limit, the final equations are independent of ρ_* and it is assumed that the relation above is satisfied. The poloidal periodicity can be specified in our coordinates as

$$f(\psi, \zeta + q/2, 1/2) = f(\psi, \zeta - q/2, -1/2). \tag{3.50}$$

which in Fourier space translates to

$$\begin{aligned} &\sum_{\mathbf{k}} \hat{f}(k_\psi, k_\zeta, 1/2) \exp\left[\frac{\mathrm{i}k_\zeta}{\rho_*} + \frac{\mathrm{i}k_\psi \psi}{\rho_*} + \frac{\mathrm{i}qk_\zeta}{2\rho_*}\right] \\ &= \sum_{\mathbf{k}} \hat{f}(k_\psi, k_\zeta, -1/2) \exp\left[\frac{\mathrm{i}k_\zeta}{\rho_*} + \frac{\mathrm{i}k_\psi \psi}{\rho_*} - \frac{\mathrm{i}qk_\zeta}{2\rho_*}\right]. \end{aligned} \tag{3.51}$$

Expanding the safety factor around a reference value q_R (the value at the centre of the radial domain)

$$\frac{qk_\zeta}{\rho_*} = \frac{q_R k_\zeta}{\rho_*} + k_\zeta \frac{\partial q}{\partial \psi} \frac{\psi}{\rho_*} + \frac{1}{2} k_\zeta \rho_* \frac{\partial^2 q}{\partial \psi^2} \left(\frac{\psi}{\rho_*}\right)^2, \tag{3.52}$$

and neglecting the second derivative correction (which gives only a ρ_* variation over the size of the box), it can be seen that this condition can be satisfied if $q_R k_\zeta / 2\pi\rho_*$ is assumed to be an integer, and if

$$\hat{f}(k_\psi, k_\zeta, \frac{1}{2}) = \hat{f}(k_\psi + k_\zeta \frac{\partial q}{\partial \psi}, k_\zeta, -\frac{1}{2}), \tag{3.53}$$

which can be understood as the connection of a mode to the appropriate higher k_ψ mode at the boundary of the s domain. Thus, increasing the number of k_ψ modes is equivalent to increasing the length of the field line simulated.

This boundary condition for the Fourier modes implies that a convenient choice for the spacing of the k_ψ modes in the discrete Fourier representation is

$$\Delta k_\psi = k_{\zeta,\min} \frac{\partial q}{\partial \psi} \frac{1}{i_k}, \tag{3.54}$$

where i_k is some integer. The integer i_k allows for control over radial resolution and boxsize, by altering the spacing between the radial modes, which would otherwise be dictated by the magnetic shear.

A further advantage of the Fourier representation is that in Fourier space the gyroaverage becomes an algebraic operation [86, 99]. From the definition of the gyroaverage (Eq. (2.29)) one finds

$$
\begin{aligned}
\langle h(\mathbf{x})\rangle &= \frac{1}{2\pi}\int_0^{2\pi} h(\mathbf{X}+\boldsymbol{\rho})d\alpha \\
&= \frac{1}{2\pi}\int_0^{2\pi}\left[\sum_{\mathbf{k}}\hat{h}\exp(i\mathbf{k}\cdot\mathbf{X})\exp(i\mathbf{k}\cdot\boldsymbol{\rho})\right]d\alpha \\
&= \sum_{\mathbf{k}}\hat{h}\exp(i\mathbf{k}\cdot\mathbf{X})\left[\frac{1}{2\pi}\int_0^{2\pi}\exp(i\mathbf{k}\cdot\boldsymbol{\rho})\right]d\alpha, \qquad (3.55)
\end{aligned}
$$

(for any function h which is independent of the the gyrophase α) since the translation by $\boldsymbol{\rho}$ becomes a multiplication in Fourier space, by the shifting theorem. The integral can be expressed as a Bessel function of the first kind

$$
\begin{aligned}
\frac{1}{2\pi}\int_0^{2\pi}\exp(i\mathbf{k}\cdot\boldsymbol{\rho})d\alpha &= \frac{1}{2\pi}\int_0^{2\pi}\exp[ik\rho\cos(\alpha-\theta)]d\alpha \\
&= \frac{1}{2\pi}\int_0^{2\pi}\exp(ik\rho\cos\alpha)d\alpha \equiv J_0(k_\perp\rho), \qquad (3.56)
\end{aligned}
$$

where the angle θ between $\boldsymbol{\rho}$ and $\mathbf{k}$ is averaged out and

$$(k_\perp\rho)^2 = \frac{m_R T_R}{Z^2B^2}g^{\alpha\beta}k_\alpha k_\beta, \qquad (3.57)$$

is the full perpendicular (unnormalised) wave vector evaluated independently for each species. In Fourier space the gyroaverage is therefore written

$$\widehat{\langle h\rangle} = J_0(k_\perp\rho)\widehat{h}. \qquad (3.58)$$

In order to specify the wave vector in normalised form, the expression

$$(k_\theta\rho_{\mathrm{ref}})^2 = g^{\zeta\zeta}k_\zeta^2, \qquad (3.59)$$

is evaluated using $g^{\zeta\zeta}$ at the low field side midplane ($s = 0$) to determine k_ζ from the value of $k_\theta\rho_{\mathrm{ref}}$ given as an input (here k_θ is not a normalised quantity). Note however that ρ_{ref} is defined on the flux surface at the major radius of the magnetic axis. The values of k_θ so defined are usually used for identifying a mode in code input and output.

3.4.1 Relation to ballooning representation

The 'ballooning representation' [93] is often used in the analytic linear treatment of a single mode, such as a drift wave, which has large extension $k_\parallel \ll k_\perp$ along the magnetic field. The combination of field aligned coordinates, spectral representation and parallel boundary condition Eq. (3.53) used in GKW give a formulation equivalent to the ballooning representation. Here we outline the strategy for constructing the ballooning representation of the gyrokinetic equation, in order to illustrate the 'ballooning' nature of the turbulence, and its relationship to the GKW flux tube.

In the ballooning representation, the toroidal perturbed solutions of the gyrokinetic equation are represented in an 'eikonal' basis $f_n^{(0)}$ which contains any rapid spatial variation perpendicular to the field. By assumption, an eikonal must satisfy

$$\mathbf{b} \cdot \nabla f^{(0)} = 0. \tag{3.60}$$

For the axisymmetric tokamak field this may be written in toroidal (ψ, θ, φ) coordinates as

$$B^\varphi \left(\frac{\partial f^{(0)}}{\partial \varphi} + \frac{B^\theta}{B^\varphi} \frac{\partial f^{(0)}}{\partial \theta} \right) = 0, \tag{3.61}$$

where for simplicity of illustration, we use the low aspect ratio approximation $\epsilon = r/R \ll 1$ to assume constant pitch over the poloidal angle with $q = \frac{B^\varphi}{B^\theta}$.[2] Assuming solutions of the form $f_n^{(0)} = l(\theta) \exp[in\varphi]$ and applying the condition of toroidal periodicity leads to the eikonal basis

$$f_n^{(0)} = \exp[in(\varphi - q(\theta + \theta_0))], \tag{3.62}$$

where n is an integer representing the toroidal mode number and θ_0 is a constant of integration representing the poloidal angle at which the mode is at its maximum. The eikonal basis solutions contain all rapid spatial variation perpendicular to the field (with $n \gg 1$)[3] and no phase variation along the field line. Time dependence and parallel spatial dependence of the perturbation are added by assuming a slowly varying 'envelope' function g around the eikonal solution in the form

$$f_n^{(1)} = g_n(\theta, v_\parallel, \mu, t,) f_n^{(0)}(\rho, \theta, \varphi). \tag{3.63}$$

Since all perpendicular variations are contained in $f_n^{(0)}$, a perpendicular wavevector $\mathbf{k}_{\perp,n}$ may be defined by analogy with the Fourier basis to satisfy

$$\nabla f_n^{(0)} \equiv i \mathbf{k}_{\perp,n} f_n^{(0)}. \tag{3.64}$$

---

[2] Dropping this assumption leads to an integral of the local pitch over θ in the eikonal.

[3] This is equivalent to the assumption in the local approximation that $k_\zeta \ll 2\pi/R$.

Hence differentiating Eq. (3.62) one finds

$$\mathbf{k}_{\perp,n} = n\left[\nabla\varphi - q\nabla\theta - \frac{\partial q}{\partial\psi}(\theta-\theta_0)\nabla\psi\right]. \tag{3.65}$$

Since $|\nabla\varphi| = 1/R$ and $|\nabla\theta| = 1/r$, this may be approximated in the low aspect ratio limit[4] by

$$\mathbf{k}_\perp = -\frac{nq}{\psi}[\psi\nabla\theta + \hat{s}\nabla\psi(\theta-\theta_0)], \tag{3.66}$$

where the definition of the magnetic shear $\hat{s} = (\psi/q)\partial q/\partial\psi$ has also been used. Comparing to the decomposition $\mathbf{k}_\perp = k_\theta\mathbf{e}_\theta + k_\psi\mathbf{e}_\psi$ one finds

$$k_{\theta,n} = -\frac{nq}{r}, \qquad k_{\psi,n}(\theta) = \hat{s}\theta k_{\theta,n} + k_{\psi_0,n}, \tag{3.67}$$

where $k_{\psi_0,n} = \hat{s}\theta_0 nq/r$ is the radial wavenumber at $\theta = \theta_0$. The physical interpretation is that the shear in the magnetic field creates a rotation in the perpendicular structure of the mode, as followed poloidally, (See, for example, Fig. 2 of Ref. [100]). The result is that magnetic shear places a limit on the poloidal extension that the mode may have, because the rotation of the mode results in greater stabilisation from the FLR effects as $k_\perp$ increases.[5] This poloidal dependence of the radial wavenumber is implicit in the GKW field aligned coordinates (compare Eq. (3.67) with $\nabla\zeta$ in Eq. (3.32)), and is preserved at the end of the field line boundary by the connection condition Eq. (3.53). The most unstable wavevector in the local model thus has $k_{\psi_0} = 0$, and maximum amplitude at $\theta_0 = 0$, which is usually where the mode drive is greatest (discussed further in Sec. 5.3).

Substituting the form Eq. (3.63) into the gyrokinetic Eq. (2.70), keeping terms only up to $\mathcal{O}(\rho_*)$, and neglecting the nonlinear terms gives the 'ballooning equation' for the parallel envelope g_n

$$\frac{\partial g_n}{\partial t} + v_\parallel\mathbf{b}\cdot\nabla g_n + g_n\mathbf{v}_d\cdot\mathbf{k}_\perp - \frac{\mu B}{m}\frac{\mathbf{B}\cdot\nabla B}{B^2}\frac{\partial g}{\partial v_\parallel} = S, \tag{3.68}$$

since $\mathbf{v}_d\cdot\nabla g_n \sim \mathcal{O}(\rho_*^2)$.

The condition of toroidal periodicity was implicit in the construction of the eikonal, but poloidal periodicity (required for a physical solution) is not intrinsic to the eikonal form, except on rational flux surfaces (where q is rational). A poloidally periodic solution can however be constructed from a linear combination of $f_n^{(1)}$

---

[4] This approximation was also made in the $s-\alpha$ geometry for $\nabla\zeta$. It can be avoided here by using the field line coordinate $\alpha = \varphi - q\theta$.

[5] Large magnetic shear, (either positive or negative) is therefore strongly stabilising, but the most unstable geometry does not have $\hat{s} = 0$, because the strongest drive occurs for $\hat{s} \sim 1$, for reasons explained very intuitively in Ref. [100] and also discussed in Sec. 5.3.

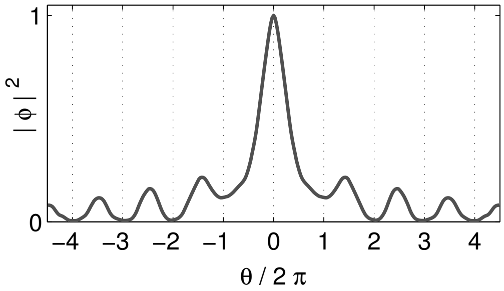

Figure 3.2: GKW solution of the ballooning mode structure for a trapped electron mode (GKW-TEM case, defined in Chapter 6) with $k_\theta \rho_s = 1.13$.

by placing an additional constraint on the envelope function g_n. The trick that characterises the ballooning representation is the construction of a new periodic envelope function from the infinite sum [93]

$$\bar{g}_n(\theta) = \sum_{p=-\infty}^{\infty} g_n(\theta + 2\pi p), \tag{3.69}$$

with the requirement that the infinite sum converges. This restriction results in a g_n that must decay away as $\theta \to \pm\infty$. The new periodic envelope function $\bar{g}_n(\theta)$ can then be used to find periodic time-dependent 'ballooning mode' solutions of the form

$$\bar{f}_n^{(1)}(\theta) = \sum_{p=-\infty}^{\infty} g_n(\theta + 2\pi p) \exp(-in(\varphi - q(\theta + \theta_0 + 2\pi p))). \tag{3.70}$$

On any rational flux surface, poloidal periodicity will be satisfied by the eikonal $f_{n_q}^{(0)}$, without the use of the $\bar{g}_n$ construction. However, since the radial wavenumber is increasing with θ, a periodic envelope function g_n cannot be physical as the energy in the mode $\sim k_\perp$ would diverge (the only exception is the case where $\hat{s} = 0$). Hence on rational surfaces the same construction must also be used for a physical solution, but not due to the requirement of poloidal periodicity. The term 'ballooning' used to describe these modes refers to their tendency to localise on the outboard side of the tokamak, and decay as $\theta \to \pm\infty$, as shown in Fig. 3.2. In general, the decay distance increases for smaller $\hat{s} = 0$, and is much more extended for electron driven modes due to their fast parallel motion.

In this treatment, we have considered a single toroidal mode with mode-number n, but ballooning representation can also be thought of as a 'ballooning transform' analogous to the Fourier transform which can represent an arbitrary function in a nonlinear system. The ballooning representation can also be extended to include radial profile variations [101–103], but in the local limit radial structure can be represented as a Fourier series in $k_{\psi,l}$. An arbitrary function can then be discretised over the three indices (l, n, p), with nonlinear terms involving a sum (or Fourier transform in the l, n directions) over all three indices. Rather many p's must be kept in the sum in order to obtain equivalent results to the method described in Sec. 3.4 [17, 98]. In the GKW spectral representation the interaction over p is achieved by the nonlinear interaction of connected modes in k_ψ and the expensive sum required for the nonlinear terms is only over two indices (and is accomplished efficiently with a 2D FFT). Thus, for nonlinear problems the spectral representation in field aligned coordinates with parallel boundary connection Eq. (3.53) used in GKW is the most efficient and natural manner to numerically implement a finite discretised equivalent of the ballooning transform, and is also used in other gyrokinetic codes [21, 104].

An understanding of the ballooning mode structure is useful in order to run GKW effectively and to interpret the results. The code can be run in two regimes: a) A single mode extending for $2n_p - 1$ poloidal turns (for a linear run), or b) a box of modes (for linear or nonlinear runs) with one poloidal turn, connected by the ballooning-shifted-periodic boundary condition Eq. (3.53). In the second case, the integer i_k determines the relationship between radial boxsize and the radial resolution, and the field line for mode n has a connected length of $N_x k_{\zeta,1}/k_{\zeta,n} i_k$ poloidal turns (nearest lower odd integer). Here N_x is the number of k_ψ modes, N_s is the number of points along the field line, and n_p is an integer. For an extended ballooning mode to be well resolved along the field, either a) high n_p or b) many k_ψ modes are needed. The length of the simulated field line differs for each mode, being longest for the long wavelength modes which dominate transport. For a single k_ζ mode, the two formulations can be made exactly equivalent as shown in the following table:

Method	N_s	i_k	N_X	n_p
a)	16	1	5	1
b)	80	N/A	1	3
a)	n_s	1	$2n_p - 1$	1
b)	$n_s(2n_p - 1)$	N/A	1	n_p

Ballooning theory can be extended to treat radial variations in the background quantities by the solution of a higher order radial envelope equation [101]. The global solutions are linear combinations of the local ballooning modes. The profile variations result in a radial variation of local mode frequency, such that the coupling of the local modes leads to a most unstable mode with $\theta \neq 0$ [102, 103, 105–107].

3.5 Gyrokinetic equations for a strongly rotating plasma

In this section we list the complete set of equations for a collisionless rotating plasma in the electrostatic limit, as implemented in GKW. The normalisations, spectral representation, geometric tensors, and local limit introduced in the preceding sections are used to write the equations in a form suitable for numerical implementation. The gyro-kinetic equation for the perturbed distribution Eq. (2.70) can be written in the form

$$\frac{\partial f}{\partial t} = \mathrm{I} + \mathrm{II} + \mathrm{III} + \mathrm{IV} + \mathrm{V} + \mathrm{VI} + \mathrm{VII} + \mathrm{VIII}, \tag{3.71}$$

with

$$\begin{aligned}
\mathrm{I} &= -v_\parallel \mathbf{b}\cdot\nabla f \rightarrow -v_R v_\parallel \mathcal{F}\frac{\partial \hat{f}}{\partial s},\\
\mathrm{II} &= -\mathbf{v}_D\cdot\nabla f \rightarrow\\
&\qquad -\frac{\mathrm{i}}{Z}\left[T_R E_D \mathcal{D}^\alpha + T_R v_\parallel^2 \beta' \mathcal{E}^{\psi\alpha} + 2 m_R v_R v_\parallel \Omega \mathcal{H}^\alpha + m_R \Omega^2 I^\alpha + Z\mathcal{E}^{\beta\alpha}\frac{\partial \Phi}{\partial x_\beta}\right] k_\alpha \hat{f},\\
\mathrm{III} &= -\mathbf{v}_E\cdot\nabla f \rightharpoonup -\rho_*^2 \frac{\partial \phi}{\partial x_\beta}\mathcal{E}^{\beta\alpha}\frac{\partial f}{\partial x_\alpha} = \rho_*^2 \mathcal{E}^{\psi\zeta}\left(\frac{\partial \phi}{\partial \zeta}\frac{\partial f}{\partial \psi} - \frac{\partial f}{\partial \zeta}\frac{\partial \phi}{\partial \psi}\right)\\
&\qquad \rightharpoonup \mathcal{T}\Big(\mathcal{E}^{\psi\zeta}\left[\mathcal{T}^{-1}(ik_\zeta\hat{\phi})\mathcal{T}^{-1}(ik_\psi\hat{f}) - \mathcal{T}^{-1}(ik_\zeta\hat{f})\mathcal{T}^{-1}(ik_\psi\hat{\phi})\right]\Big),\\
\mathrm{IV} &= +\frac{\mathbf{b}}{m}\cdot(\mu\nabla B + \nabla\mathcal{E}_R)\frac{\partial f}{\partial v_\parallel} \rightarrow v_R\left(\mu B\mathcal{G} + \frac{1}{2}\frac{\partial \mathcal{E}_R}{\partial s}\mathcal{F}\right)\frac{\partial \hat{f}}{\partial v_\parallel},\\
\mathrm{V} &= -\mathbf{v}_E\cdot\nabla F_M \rightarrow \mathrm{i}k_\alpha\hat{\phi}\mathcal{E}^{\alpha\psi}\left[\frac{1}{L_n} + \frac{m\Omega^2}{T}\mathcal{L} + E_T\frac{1}{L_T} + \frac{2v_\parallel}{v_R}\frac{u' B_t}{B}\right]F_M,\\
\mathrm{VI} &= -\mathbf{v}_D\cdot\nabla F_M \rightarrow \frac{1}{Z}\left[T_R E_D\mathcal{D}^\psi + 2m_R v_R v_\parallel \Omega\mathcal{H}^\psi + m_R\Omega^2 I^\psi + Z\mathcal{E}^{s\psi}\frac{\partial \Phi}{\partial s}\right]\\
&\qquad \times\left[\frac{1}{L_n} + \frac{m\Omega^2}{T}\mathcal{L} + E_T\frac{1}{L_T} + \frac{2v_\parallel}{v_R}\frac{u' B_t}{B}\right]F_M,\\
\mathrm{VII} &= -\frac{Ze}{T}v_\parallel\mathbf{b}\cdot\nabla\langle\phi\rangle F_M \rightarrow -\frac{Z}{T_R}v_R v_\parallel\mathcal{F}\frac{\partial\widehat{\langle\phi\rangle}}{\partial s}F_M,\\
\mathrm{VIII} &= -\frac{Ze}{T}\mathbf{v}_D\cdot\nabla\langle\phi\rangle F_M \rightarrow\\
&\qquad -\mathrm{i}\left[E_D\mathcal{D}^\alpha + \beta' v_\parallel^2\mathcal{E}^{\psi\alpha} + \frac{2m_R v_R}{T_R}v_\parallel\Omega\mathcal{H}^\alpha + \frac{m_R\Omega^2}{T_R}\mathcal{I}^\alpha + \frac{Z}{T_R}\mathcal{E}^{\beta\alpha}\frac{\partial\Phi}{\partial x_\beta}\right]k_\alpha\,\widehat{\langle\phi\rangle}\,F_M,
\end{aligned}$$

where the arrows represent the transformations to normalised ($\rightharpoonup$) and Fourier ($\rightarrow$) quantities and where

$$E_D = v_\parallel^2 + \mu B, \qquad E_T = v_\parallel^2 + 2\mu B + \mathcal{E}_R - \frac{3}{2}. \tag{3.72}$$

The equations above apply to each of the species individually.

The only nonlinearity in the equations is the $\mathbf{v}_E \cdot \nabla f$ Term III. This term causes nonlinear saturation when the perturbations reach large enough amplitudes, and linear stability can be investigated by removing this term. In the linear case the binormal modes are decoupled, but different radial modes can still be coupled over the parallel boundary conditions. An unstable mode will exponentially grow to infinite amplitude, and GKW therefore applies a scaling of the equations at every time-step to obtain a stationary solution with constant growth rate and frequency..

For the linear terms, Term I describes the free streaming motion of particle along the field line, and Term II describes the curvature and inertial drifts in the perturbed distribution, which cause propagation of a drift wave. Term IV describes the magnetic trapping as particles move through the magnetic field gradient, and Term V provides the energy source from the background gradients which drive the instabilities. Term VI, when combined with collisions, can generate the neoclassical fluxes, but is not used in any results presented in this thesis. Term VII describes the collisionless parallel Landau damping of the perturbations against the background Maxwellian, and Term VIII describes the equivalent damping for the perpendicular drifts.

To close the equations, the field ϕ must be obtained by solving the Poisson equation described in Sec. 2.9. In the spectral representation, the gyroaverage operator G is replaced by the Bessel function J_0. The integral of J_0^2 multiplied with the Maxwellian in the second term of Eq. (2.82) can then be evaluated using

$$\frac{1}{v_{\mathrm{th}}^2} \int_0^\infty \mathrm{e}^{-v_\perp^2/v_{\mathrm{th}}^2} J_0^2\left(k_\perp v_\perp \frac{ZeB}{m}\right) v_\perp \,\mathrm{d}v_\perp = \Gamma(b) = \mathrm{e}^{-b} I_0(b), \tag{3.73}$$

(unnormalised) where I_0 is the modified Bessel function and

$$b = \frac{1}{2} m_R T_R (k_\perp \rho_* R_{\mathrm{ref}}/ZB^2)^2 = \overbrace{\frac{1}{2}\frac{k_\perp^2 m^2 v_{\mathrm{th}}^2}{e^2 B^2}}^{\text{in original units}}. \tag{3.74}$$

For the first term, the velocity space integral is rewritten in the gyrocentre phase space with the Jacobian Eq. (2.46). Using the normalisations of GKW the Poisson equation for a single mode can then be written as

$$\sum_s Z_s n_{R_0,s}\left[2\pi B\int \mathrm{d}v_\parallel \mathrm{d}\mu J_0(k_\perp\rho_s)\hat{g}_s + \frac{Z_s}{T_{R,s}}[\Gamma(b_s)-1]\exp(-\mathcal{E}_{Rs})\hat{\phi}\right] = 0. \tag{3.75}$$

In the adiabatic electron limit only the ion dynamics is simulated and the Poisson equation above is evaluated as

$$\sum_{\text{s,ions}} Z_s n_{R_0,s}\left[2\pi B\int \mathrm{d}v_\parallel \mathrm{d}\mu J_0(k_\perp\rho_s)\hat{g}_s + \frac{Z_s}{T_{R,s}}[\Gamma(b_s)-1]\exp(-\mathcal{E}_{Rs})\hat{\phi}\right] = \frac{n_{R_0,e}\exp(-\mathcal{E}_{Re})}{T_{Re}}(\hat{\phi}-\widehat{\{\phi\}}), \tag{3.76}$$

where the index e refers to the electrons, the sum on the left hand side of the equation is over all ion species, and the correction $\{\phi\}$ is zero except for the zonal modes with $k_\zeta = 0$ (See also Sec. 1.5 and Ref. [7]). This field equation differs from the literature [54, 58] only in the polarisation term which includes the rotational density variation in the Maxwellian.

The equations presented here reflect the collisionless electrostatic limit used for nearly all the results presented in this thesis. For details of the electromagnetic terms and the collision operator, we refer the reader to Refs. [58, 59]. The electrostatic limit is valid for plasmas with low β, the predominant case in conventional tokamaks. The collisionless limit may be justified when collisional processes are slow relative to the turbulent fluctuations (Eq. (2.54)), if ion heat transport is the channel of interest. In these cases, the role of collisions can be approximated by numerical dissipation (see Sec. 4.6.1), but the subtle effects of this approximation on nonlinear saturation on the longer term transport timescales is a matter of open debate [108, 109]. Furthermore, for accurate determination of particle or electron heat transport, collisional diffusion across the trapped-passing boundary in velocity space is important even on shorter timescales.

3.6 Centrifugal potential

We recall that the rotation of the plasma leads to an equilibrium density variation within a flux surface

$$n(\theta) = n_{R_0,s} \exp\left(\frac{-Z_s \Phi(\theta))}{T_{R,s}} + \frac{m_s \Omega^2 (R^2 - R_0^2)}{T_{R,s}} \right), \tag{3.77}$$

(normalised units). The background equilibrium potential Φ in the rotating frame is found by applying the quasineutrality condition over all the species

$$Q(\Phi(\theta,\psi)) = \sum_s Z_s n_{R_0,s}(\psi) \exp\left(\frac{-Z_s \Phi(\theta,\psi)}{T_{R,s}(\psi)} \right) \exp\left(\frac{m_s \Omega^2 \left(R(\theta,\psi)^2 - R_0(\psi)^2 \right)}{T_{R,s}(\psi)} \right) = 0. \tag{3.78}$$

Since there is only one negative species and the exponential function is monotonically increasing, the equation $Q(\Phi) = 0$ will always have exactly one root. In GKW, Φ is calculated numerically for arbitrary species combinations from the quasineutrality condition by an iterative root finding bisection algorithm. The calculation is done once for each parallel grid point in s during the initialisation phase of the code. The terms II, VI, and VIII in Eq. (3.71) also require the ψ and s derivatives of Φ, which are calculated using a fourth order finite difference.

The bisection algorithm begins with an upper limit estimate for Φ. The initial value used in GKW is (somewhat arbitrarily) taken as

$$\left[\max_s \{ \log(1 + |Z_s n_s|) \} + \max_s \{ m_s \log(1 + n_s) \} \right] \Omega^2 (R^2 - R_0^2) + 0.1, \tag{3.79}$$

which should always contain the root, but be small enough to prevent exponentiation overflows. $\Phi_b = -\Phi_a$ is the lower limit estimate. It is possible that extreme species input data could break the solver, and the upper limit estimate might need to be adjusted for those cases. The value is chosen to ensure that the root lies in the range (Φ_b, Φ_a). The mid value $\Phi_{\mathrm{est}} = (\Phi_a + \Phi_b)/2$ is taken and the value of $Q(\Phi_{\mathrm{est}})$ is calculated. If $Q(\Phi_{\mathrm{est}}) > 0$, then the upper estimate is updated ($\Phi_a = \Phi_{\mathrm{est}}$), and if $Q(\Phi_{\mathrm{est}}) < 0$, then the lower estimate is updated ($\Phi_b = \Phi_{\mathrm{est}}$). The process repeats until the solution has converged to within machine accuracy. The bisection algorithm, while not the fastest possible, is guaranteed to converge as long as the bounds are appropriate and the function Q has only one root in the initial range. In practice, the convergence occurs in about 55 iterations using the initial estimates specified above.

In the case of a plasma of only singly charged ions, Eq. (3.78) solves exactly

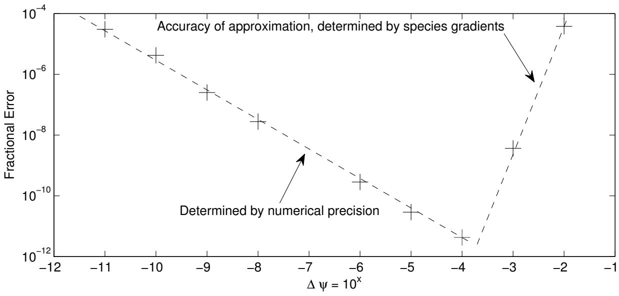

Figure 3.3: Numerical experiment to determine optimum $\Delta\psi$ for calculating the radial derivative of the centrifugal potential Φ for the singly charged ions GA-STD case described in Chapter 4. The experiment was conducted in double precision and the fractional error is calculated against the analytic result Eq. (3.81).

to give

$$\Phi = \frac{T_e T_i}{T_e + T_i}\left(\frac{m_i}{T_i} - \frac{m_e}{T_e}\right)\Omega^2(R^2 - R_0^2), \tag{3.80}$$

(normalised units, unlike Eq. (2.58)) which has radial derivative

$$\begin{aligned}\frac{\partial\Phi}{\partial\psi} = \left[\frac{m_i\frac{\partial T_e}{\partial\psi} - m_e\frac{\partial T_i}{\partial\psi}}{T_e + T_i} + \frac{m_e T_i - m_i T_e}{(T_e + T_i)^2}\left(\frac{\partial T_e}{\partial\psi} + \frac{\partial T_i}{\partial\psi}\right)\right]\Omega^2(R^2 - R_0^2)\\ +2\Omega^2\left[\frac{m_i T_e - m_e T_i}{T_e + T_i}\right]\left(R\frac{\partial R}{\partial\psi} + R_0\frac{\partial R_0}{\partial\psi}\right).\end{aligned} \tag{3.81}$$

If the bulk ion species is singly charged, these quantities are evaluated in the code to provide a check on the solution of the root finding algorithm.

In the local flux tube model, the gyrokinetic equation is solved only on one flux surface (i.e. at one position in ψ), keeping radial derivatives of equilibrium quantities. To consistently calculate the radial derivative of Φ, Eq. (3.78) is also solved numerically on adjacent flux surfaces using $Q(\Phi, s, \psi + \Delta\psi) = 0$, using the radial derivatives of the species quantities to calculate the temperature and densities on adjacent flux surfaces.

The choice of $\Delta\psi$ used in the code is motivated by a compromise between machine precision when dividing by small numbers, and the accuracy of the finite difference as $\Delta\psi \to 0$. The discrepancy between the root finding algorithm and the analytic solution (Eq. (3.81)) is plotted in Fig. 3.3. The value of $\Delta\psi = 10^{-4}$ is implemented as a permanent choice, which for the case investigated minimises the error to less than 10^{-11} in double precision.

The density n_R and density gradient $1/L_n|R_0$ (Eq. 3.8) are defined for each species at the point on the flux surface at which $R = R_0$. Two choices for the definition of R_0 are available in the code; $R_0 = R_{\mathrm{axis}}$, which sets R_0 as the major radius of the magnetic axis (but the reference point is not on the axis itself), and the default $R_0 = R_{\mathrm{LFS}}$, which sets R_0 to be the value of R at $s = 0$, in the plane of the magnetic axis at the low field side (for general geometry this may *not* be equivalent to the maximum R). This choice alters only the definition of the geometry quantities $\mathcal{J}$ and $\mathcal{K}$. In the rotating case, the effective density gradient varies over the flux surface and there is no longer one obvious definition of the density gradient as a dimensionless quantity. For instance

$$\frac{1}{L_n^E}(\theta) = -\frac{1}{n}\frac{\partial n}{\partial \psi}, \qquad \frac{1}{L_n^{e1}}(\theta) = -\frac{1}{\{n\}}\frac{\partial n}{\partial \psi}, \qquad \frac{1}{L_n^{e2}}(\theta) = -\frac{1}{n_{R_0}}\frac{\partial n}{\partial \psi}, \tag{3.82}$$

can each be argued to be a relevant quantity. The most appropriate may be determined by the nature of the particular instability being examined. These definitions can be evaluated to be

$$\frac{1}{L_n^E} = \frac{\partial \mathcal{E}_R}{\partial \psi} + \mathcal{E}_R \frac{1}{L_T} + \frac{1}{L_n}\bigg|_{R_0}, \qquad \frac{1}{L_n^{e1}} = \frac{1}{L_n^E}\frac{\exp(-\mathcal{E}_R)}{\left\{\exp(-\mathcal{E}_R)\right\}}, \qquad \frac{1}{L_n^{e2}} = \frac{1}{L_n^E}\exp(-\mathcal{E}_R). \tag{3.83}$$

(The flux surface average operation is denoted by $\{\}$.) In addition, the perturbation weighted flux surface average of the effective density gradient,

$$\frac{1}{L_n^*} = \frac{\{|\phi(\theta)| 1/L_n^E(\theta)\}}{\{\phi(\theta)\}}, \tag{3.84}$$

can also be of interest, since it weights the variation to the locations where the mode is most unstable. Unlike the previous definitions this does not only depend on the equilibrium quantities, and can only be calculated after the perturbed solution is determined.

Since the density gradient is an important parameter for determining the stability of many modes, GKW calculates $1/L_N^E$ and $1/L_n^{e1}$ and n/n_{R_0} for each species as a function along the field. $1/L_n^{e2}$ can then be trivially calculated from the other two, and $\frac{1}{L_n^*}$ can also be calculated using other code output. It should be noted that even when the input $1/L_n|_{R_0}$ is the same for every species, the effective $1/L_n^E$ can differ for each species at locations other than R_0. For typical parameters of a deuterium plasma, the variation in effective density and gradient can be 30% at $\Omega = 1$, increasing rapidly for $\Omega > 1$. In practice, we find that the different definitions do not differ substantially, except for very heavy species, and we use $1/L_n^E$ exclusively in what follows.

3.7 Diagnostics

The fluxes are calculated as flux surface averaged guiding centre radial fluxes and, following Eq. (1.23), are given by the equation

$$\Gamma_j^\psi = \left\{ \int \mathrm{d}^3\mathbf{v} \tilde{\mathbf{v}}_E \cdot \nabla\psi \alpha_j f \right\}, \tag{3.85}$$

for the electrostatic flux. Here $j = (1, 2, 3)$ with $\alpha_j = (1, mv^2/2, mv_\parallel)$, i.e. $j = 1$ is the particle flux, $j = 2$ is the heat flux Q_s, and $j = 3$ is the parallel velocity flux $\Gamma_\parallel$.

Both the potential ϕ and the distribution function f are represented as a sum over complex Fourier modes. To obtain a real quantity which does not spatially average to zero, a particular wavevector of the representation of f must be combined with the complex conjugate of the same wavevector in the representation of ϕ, i.e.

$$\langle\!\langle \tilde{v}_E \tilde{f} \rangle\!\rangle = 2 \sum_m \mathrm{Re}[\langle\!\langle \hat{\mathbf{v}}_{Em}^\dagger \cdot \nabla\psi \hat{f}_m \rangle\!\rangle], \tag{3.86}$$

where $\hat{v}_{Em}$ and $\hat{f}_m$ are the Fourier amplitudes of the $E \times B$ velocity and distribution function of the mode m respectively, the dagger denotes the complex conjugate, and $\langle\!\langle\rangle\!\rangle$ is the time average over a few mode periods $1/\omega$. Substituting the various definitions one can derive the expression for the normalised electrostatic fluxes

$$\mathcal{I}_j = \sum_m \left\{ 2\pi B \mathcal{E}^{\psi\beta} k_{\beta m} \int \mathrm{d}\mu \mathrm{d}v_\parallel \, \hat{\alpha}_j \mathrm{Im}[\langle \hat{\phi}_m \rangle^\dagger \hat{f}_m] \right\}, \tag{3.87}$$

where $\sum_m = \sum_{k_\zeta} \sum_{k_\psi}$ is a sum over all modes and $\{\}$ is an integration over the flux surface. The fluxes in physical units can then be obtained from

$$R_{\mathrm{ref}} \Gamma_s^\psi = n_{R_0,s} \rho_*^2 v_{\mathrm{thref}} \mathcal{I}_1, \tag{3.88}$$

$$R_{\mathrm{ref}} Q_s^\psi = n_{R_0,s} T_s \rho_*^2 v_{\mathrm{thref}} \mathcal{I}_2, \tag{3.89}$$

$$R_{\mathrm{ref}} \Gamma_{\parallel s}^\psi = m_s n_{R_0,s} v_{ths} \rho_*^2 v_{\mathrm{thref}} \mathcal{I}_3. \tag{3.90}$$

for the particle flux, heat flux, and parallel momentum flux respectively.[6]

These fluxes are all calculated in the comoving (starred) frame. Applying the transformation of Sec. 2.4, $v_\parallel^* = v_\parallel^L - R_A \Omega B_t / B$, one finds that they are related

---

[6] Note that parallel momentum is not a true flux surface quantity. To calculate the parallel part of the toroidal angular momentum flux, $\Pi_\parallel$, the multiplier $\alpha_j = s_B R B_t v_\parallel / B$ should be used, but here we define the parallel velocity flux for consistency with the results in Chapter 5. In the $s - \alpha$ model (only) $RB_t/B = R_A$, and the two are interchangeable. See also Sec. 5.2.

to the fluxes in the laboratory frame (unnormalised units) by

$$\Gamma^* = \Gamma^L, \tag{3.91}$$

$$Q^* = Q^L - \frac{R_A \Omega B_t}{B}\Gamma_\parallel^L + \frac{1}{2}m_i\left(\frac{R_A \Omega B_t}{B}\right)^2 \Gamma^L, \tag{3.92}$$

$$\Gamma_\parallel^* = \Gamma_\parallel^L - m_i \frac{R_A \Omega B_t}{B}\Gamma^L. \tag{3.93}$$

The fluxes presented in this thesis are all fluxes calculated in the rotating frame, but are similar to those in the laboratory frame since the first term on the RHS dominates for typical experimental parameters.

3.8 Numerical implementation

The equations above are solved in GKW with a combination of finite difference and spectral methods, coded in the Fortran 95 programming language. In this section, a summary of the numerical techniques is presented to allow the reader to understand later sections. For further details of the numerical implementation of GKW, we refer the reader to [58, 59].

The linear terms are stored in an unchanging matrix which is calculated at the initialisation of the code, and remains constant thereafter. Derivatives in s and $v_\parallel$ (terms I and IV) are implemented as fourth order finite differences with numerical hyperdiffusion. The perpendicular derivatives are evaluated algebraically in Fourier space, including in the nonlinear term (III), in which the nonlinear convolution is implemented with a pseudospectral approach using Fast Fourier Transforms (FFTs). The velocity $\mathbf{v}_E$ and ∇f are calculated in Fourier space, then transformed to real space and multiplied. The product is transformed back into Fourier space.

Time integration is performed explicitly with a fourth order Runge-Kutta scheme. The right hand side of the time integration is evaluated in three sections, as follows: 1) Multiplication of a dense matrix by the solution vector, to perform the integration required for calculation of the fields. 2) Evaluation of the nonlinear terms using repeated 2D FFTs with the FFTW3 library [110]. 3) Multiplication of a sparse diagonal matrix with the current solution vector for the linear terms.

GKW uses a uniform grid in $v_\parallel$, and s, and a quadratically spaced grid in magnetic moment μ ($v_\perp$ is equally spaced). These grids are one feature that distinguish GKW from other continuum gyrokinetic codes [21, 104, 111, 112]. The uniform velocity grid has the advantage of easing the implementation of the centrifugal trapping term, but has the disadvantage of requiring many parallel velocity space points for accurate determination of particle fluxes. Furthermore the uniform grids also lend themselves to efficient parallelisation.

A typical nonlinear simulation with GKW requires of the order of 50 million grid points, which dictates that the code must be able to efficiently utilise hundreds to thousands of processors on modern high performance hardware. GKW is parallelised using the Message Passing Interface (MPI). Each parallel process is responsible for solving the equations over a subdomain of the space and a subset of the species. A process usually only has knowledge of the part of the solution it is responsible for, unless explicitly communicated between processes using the MPI library.

The equation for the distribution function contains no derivatives in the magnetic moment μ, which means that the distribution function for any point in the μ grid can be updated independently of the other points in the μ grid. Similarly, the distribution function for each species can be updated independently. The μ grid and the species (typically at least 16 points) can therefore be easily decomposed across processors. However, these points are coupled via the fields, which must be updated before the distribution function can be calculated in an explicit time step. The field equations involve a summation over the whole of the velocity space and the species, for which the code requires a global inter-process reduction sum.

To allow GKW to scale to thousands of processors, further parallelisation over the $v_\parallel$ and s directions is required, which requires communication of edge data values to ghost cells on neighbouring processors on the grid in order that the finite differences can be evaluated. Parallelisation over the $v_\parallel$ direction also involves extending the parallel reduction sum in the fields calculation to this dimension. The maximum number of processors on which GKW can run on is determined by the problem size. When the code is near this limit, parallel efficiency can be reduced by the large communications overheads, particularly from the parallel reduction for the fields, which involves a large amount of data communication across all processors. Strong scaling to 4096 cores with 80% effciency has been demonstrated for a realistic problem size [58].

3.8.1 Hybrid scheme

In the course of this thesis, hybrid parallelism combining distributed memory MPI parallelism with shared memory OpenMP parallelism was implemented to allow the code to scale further, and more efficiently. Many modern high performance machines now have an architecture with a number of shared memory CPU cores on each node (2-24), and a large number of these nodes connected by a fast network interconnect. The communication between nodes is much slower than between cores, and a well optimised and well utilised MPI implementation will take advantage of this by putting the most intensive communication on the local node. In cases where this is not done, or cases where a subset of the problem grid does not fit nicely on a single node, the efficiency of the inter-node communication may be increased by reducing the number of intra-node MPI processes in the communication. For example, on a machine with 8 cores per node (e.g. HPC-FF), 1024 processors can be utilised with the combinations (number of MPI processes, number of OpenMP threads per node) = (1024,1), (512,2), (256,4), or (128,8), where the lower number of MPI processes in the latter case may result in a more efficient reduction sum (though in theory the amount of inter-node data communicated by the ideal MPI usage would remain the same).

In GKW, hybrid parallelism is achieved by subdividing the most CPU intensive loops amongst OpenMP threads. The slowest of these is the loop in nonlinear terms, where for each local grid point, 5-7 FFTs in 2D must be performed. At the maximum limit on the number of MPI processes, there will always be at least 2 (4 with collisions) points in this loop which can be divided between threads. (The code could be rewritten here to increase the number of threads that can be used here, if the hybrid scheme is first demonstrated to bring a clear benefit at 2-4 threads). The second largest loop which must be parallelised is the sparse matrix-vector multiply involved in the linear terms. Due to the sparse matrix storage format, this loop cannot be vectorised, but cache efficiency can be maximised by an appropriate sorting of the matrix. For the Hybrid scheme, the matrix elements are sorted so they can be subdivided between threads by the binormal modes (which are independent), to ensure there is no data race in the update of the right hand side. The same technique is used for the fields calculation. All possible smaller loops (<5% runtime) are also parallelised with OpenMP, but there are diminishing returns here due to the overhead involved in thread branching. This inherently serial element of the code will limit the number of threads that can efficiently be used (currently two).

Tests with the hybrid scheme on up to 1536 processors (on HPC-FF: IBM-Intel-Xeon-Infiniband) have demonstrated up to a 5% performance increase using two OpenMP threads per node. We expect that for larger problems, greater improvements may be observed at higher numbers of processors if the hardware communication capability is nearer its limit, but this remains to be demonstrated. In principle, the present hybrid scheme should allow the code to efficiently scale to twice as many processors.

Chapter 4

Homogeneous sheared flows in spectral methods

4.1 Introduction

Sheared flows are of interest in a range of fluid and plasma dynamics problems as they often play a governing role in the turbulence. The free energy present in a shear flow can drive turbulence, as is the case in the well known Kelvin-Helmholtz fluid instability (See, for example, Ch. 4 of Ref. [113]), whilst the distorting action of a sheared flow can suppress turbulence driven by density or temperature gradients by pushing the turbulence to smaller scales (e.g. in atmospheric convective cells) [33]. In a tokamak plasma, sheared $E \times B$ flows break apart the largest scale structures perpendicular to the magnetic field, reducing both turbulence drive and radial transport, and in some cases completely quenching the turbulence [29, 114]. The presence of a magnetic field stabilises the Kelvin-Helmholtz instability to the extent that flow gradients required to excite it are usually far beyond those seen in tokamak experiments [115]. However, a hybridisation of modes can occur in which the ITG mode is destabilised by parallel shear flows [44].

The evolution of these turbulent systems is governed by nonlinear partial differential equations which are often solved by direct numerical simulation using spectral methods in a finite box. These simulations of turbulence model a local region of a larger domain, on a scale at which gradual global variations in the larger system properties can be neglected. This local approximation (discussed in Chapter 2), in which the turbulence is assumed statistically similar everywhere in the simulated domain, relies on the use of periodic boundaries to model locally homogeneous turbulence. Provided that the turbulence correlation lengths are small compared to the domain size, such a model can provide a consistent local representation of the turbulence, and describe local attributes of the system independent of any effect due to a system boundary.

Sheared flows arise locally and self-consistently from nonlinear gyrokinetic turbulence (e.g. the plasma zonal flows introduced in Chapter 1), but the variation scale of these self generated flows is necessarily short compared to the model domain. A larger scale background shear flow may also be present as part of the equilibrium of the system, driven by effects on scales outside the local model. In the case of a tokamak equilibrium, a plasma rotation profile may be driven by neutral beam injection (NBI) used to heat the plasma, but can also arise spontaneously [116] when turbulent mechanisms provide a net transport of angular momentum across flux surfaces [117] (discussed further in Chapter 5). Plasma rotation is of practical importance in tokamaks, since it is widely accepted that sheared flows play a role in regulating microturbulent transport [28, 29], and are associated with the formation of transport barriers which provide access to the H-mode and advanced operating regimes [37, 38].

Since we are interested in understanding the role that background shear flows have on the turbulent system, it is useful to model a homogeneous shear flow as part of the background equilibrium as an input to the model, in contrast to the smaller radial scale zonal flows which arise self-consistently from the solution. A homogeneous shear flow is a flow with a constant shearing rate

$$\omega_s = \frac{dv_y}{dx}, \tag{4.1}$$

(constant in both time and space), such that the flow magnitude increases linearly in the direction perpendicular to the direction of the flow. In local gyrokinetics, this background plasma flow is perpendicular to the magnetic field ($x = \psi, y = \zeta$), and lies in the flux surface. As with the other equilibrium quantities, the background flow has a constant gradient across the radial domain. The size of this shearing rate relative to the linear growth rates of the system determines the importance of the shearing in breaking up turbulent eddy structures. Since the flow magnitude is monotonically changing radially across the simulation domain, the flow profile is necessarily aperiodic and cannot satisfy the boundary periodicity requirements needed for the Fourier decomposition Eq. (3.46). Unlike the other background derivatives, the derivative of the background flow cannot be reduced to a linear source term, since it acts on the perturbations as a nonlinear term coupling the k_x modes .

In this chapter, we explore strategies for treating homogeneous shear flows in a system with periodic boundary conditions, before describing the implementation chosen for GKW, and a benchmark against an alternative implementation in another gyrokinetic code.

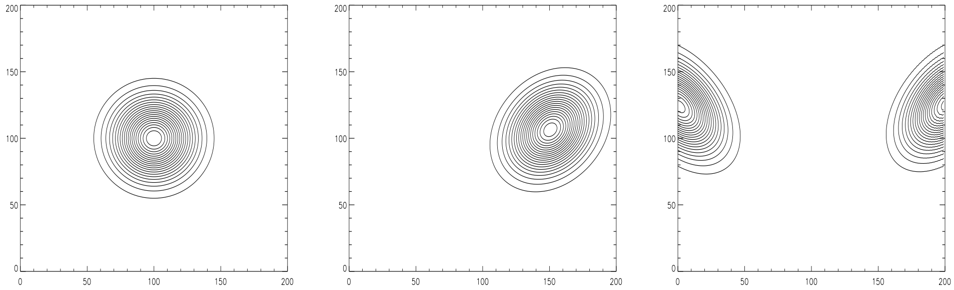

(a) $t = 0,\ t = \frac{L_x}{v_x}$ (b) $t = \frac{1}{4}\frac{L_x}{v_x}$ Advect, shear (c) $t = \frac{1}{2}\frac{L_x}{v_x}$ Inversion

Figure 4.1: Numerical solution of Eq. (4.2) using finite differences with periodic boundaries at $x = \{0, 200\}$ and $y = \{0, 200\}$. After the advection has completed one precession through the box ($t = \frac{L_x}{v_x}$), the Gaussian has returned exactly to its initial condition as shown in a). The net shear taking into account the boundary is zero.

4.2 Shear-periodic boundary conditions

To illustrate the effect of periodic boundary conditions on the homogeneous shear problem, it is instructive to consider a simple two dimensional advection problem with perpendicular homogeneous shear:

$$\frac{\partial f(x,y,t)}{\partial t} + v_x\frac{\partial f}{\partial x} + \omega_s x\frac{\partial f}{\partial y} = 0, \tag{4.2}$$

which has a constant x advection v_x and a constant shearing rate with $v_y = \omega_s x$. To investigate the effect of periodic boundaries on this problem, we solve Eq. (4.2) numerically in a simple code with explicit time integration, using finite differences for the derivatives, and an initial condition of a 2D Gaussian. The result, in Fig. 4.1, reveals that as the structure passes through the boundary, it undergoes an inversion which undoes the effect of the shearing during one precession through the box. This is perhaps not surprising, since unrolling the periodic boundaries with repetition of the domain shows that the that flow v_y has the form of a sawtooth wave; and, the Δv_y through the boundary has the equal and opposite effect to the Δv_y over the domain.

The simple advection problem can be evaluated equally well in Fourier space. Taking the continuous 2D Fourier transform (CFT) of Eq. (4.2) gives

$$\frac{\partial \hat{f}(k_x,k_y,t)}{\partial t} - ik_x v_x\hat{f} - k_y\omega_s\frac{\partial \hat{f}}{\partial k_x} = 0. \tag{4.3}$$

This equation can also be solved numerically but some care is needed. A standard finite difference representation of the spectral derivative (the third term on the left hand side) leads to a smearing in the shear profile from a sawtooth to a sinusoid. To obtain the correct result one must use the harmonic derivative [29, 118]:

$$\frac{\partial}{\partial k_y}(\hat{f}_{k_x;n}) \approx \sum_p \left(\frac{1}{p}\right)(-1)^{p+1}(\hat{f}_{k_x;n+p} - \hat{f}_{k_x;n-p}), \tag{4.4}$$

which can be obtained with the convolution theorem. If the spectral derivative is implemented in this way, solving Eq. (4.3) gives exactly the same results, (including the boundary inversion, Fig. 4.1) as solving Eq. (4.2) using finite differences. The convolution for computing the harmonic derivative gives a term which is equivalent to performing the inverse transform (in x only), applying the shifting theorem on the k_y vectors and Fourier transforming back again:

$$k_y \omega_s \frac{\partial \hat{f}}{\partial k_x} dt \approx \mathcal{F}_x \left[\{\mathcal{F}_x^{-1}(\hat{f})\} e^{i\omega_s x k_y dt} \right], \tag{4.5}$$

which provides a third method for solving the same problem. None of these methods, however, provide an acceptable solution; because the flow profile does not satisfy the periodicity of the discrete Fourier transform. Each method correctly implements the $E\times B$ shearing term inside the computational domain, but does not represent a homogeneous shear flow, since any turbulent structure passing through the radial boundary will experience a discontinuity in the flow profile (which in the periodic domain has a sawtooth form). This discontinuity violates the assumptions of the local limit, which assume that the turbulence is homogeneous with no effect due to the boundary. To satisfy this requirement, a periodic boundary should be both transparent and invisible to the turbulence. In GKW, implementations of the shear flow using Eq. (4.5) with periodic boundaries demonstrate an inhomogeneous solution: At low γ_E, the localised increased shear at the boundary breaks structures which span the boundary, whilst at high γ_E, the huge shear at the boundary can drive instabilities at the box edge even when turbulence is quenched elsewhere in the box.[1]

The question at hand, therefore, is how to model a finite domain of globally homogeneous turbulence in the presence of a homogeneous shear flow, in a manner which is impervious to the boundary. The most natural solution is to have time-dependent boundary conditions which move with the shear flow. In such a 'shear-periodic' model [119, 120] the boundaries satisfy the requirement that they have no effect on the turbulence. The boundary connection point mapping moves at the rate

---

[1] The original quench rule (Eq. (4.42)) of [29] was established using a gyrofluid model with exactly this deficiency, which led to unstable eigenmodes induced by the boundary [118].

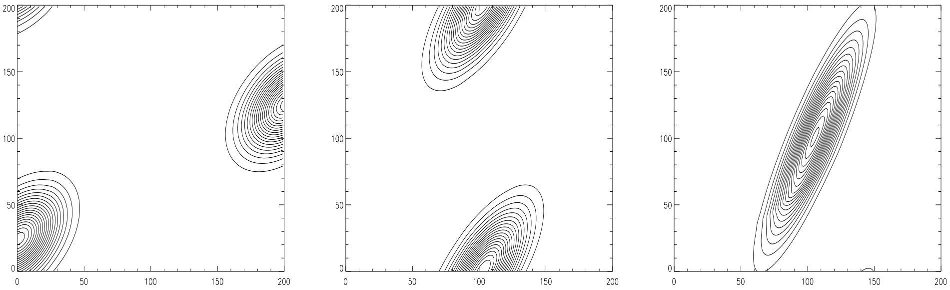

(a) $t = \frac{1}{2}\frac{L_x}{v_x}$ (b) $t = \frac{L_x}{v_x}$ (c) $t = 2\frac{L_x}{v_x}$

Figure 4.2: Numerical solution of Eq. (4.2) using finite differences with *shear-periodic* boundary at $x = \{0, 200\}$, and periodic boundary at $y = \{0, 200\}$. The shear-periodic boundaries remove the boundary inversion of Fig. 4.1. The same initial Gaussian, v_x, L_x and ω_S are used.

of the mean flow at the boundary such that

$$f(-a, y, t) = f(a, y \oplus \omega L_x t, t), \tag{4.6}$$

where the x boundaries are at $x = \pm a$ with $L_x = 2a$ and the $\oplus$ represents arithmetic modulo L_y. This boundary condition alters the meaning of 'periodic', such that any structure passing through the boundary may therefore arrive at a new (time-dependent) y position (Fig. 4.2), which can be understood as adjacent boxes moving relative to each other with the background flow. Shear-periodic boundary conditions provide the globally homogeneous consistent representation of local turbulence in the presence of homogeneous shear flows, without any need for moving coordinates or wavevectors.

In a finite difference code, shear-periodic boundaries are easy and effective to implement (as demonstrated by the simple code used to generate Fig. 4.2), and have been used successfully in the computational fluid dynamics community (for example [121]). Since GKW exploits many useful properties of the spectral representation for an efficient numerical representation (described in Chapter 3), we are interested in extending the shear-periodic boundary condition to the discrete Fourier representation.

Unfortunately, the shear-periodic modification to the boundary conditions means that the periodicity is no longer preserved in the simple one-to-one sense required for a standard discrete Fourier representation. As mentioned in Chapter 3, discretisation of the Fourier transform corresponds implicitly to a move from an infinite domain to a finite domain, with the minimum nonzero wavenumber determining the size of the box. In this Chapter, we define the 1D discrete Fourier transform (DFT) as:

$$
\begin{aligned}
&\mathcal{F}(f(x)) \rightarrow \hat{f}(k_j) = \sum_{n=0}^{N-1} f(x_n) e^{-ik_j x_n} \qquad (4.7)\\
&x_n = \tfrac{nL_x}{N}\\
&k_j = \tfrac{2\pi j}{L_x}, \qquad j = 0, .., N-1.
\end{aligned}
$$

This definition can be used to transform the first order forward finite difference of a first derivative to obtain

$$
\begin{aligned}
\mathcal{F}\left(\frac{\partial f(x)}{\partial x}\right) &\rightarrow \sum_{n=0}^{N-1}\left[\frac{\partial f(x)}{\partial x} e^{-ikx}\right](x_n) && (4.8)\\
&= \sum_{n=0}^{N-1}\left[\frac{\partial}{\partial x}(f(x)e^{-ikx}) + ikf(x)e^{-ikx}\right](x_n) && (4.9)\\
&= \sum_{n=0}^{N-1}\frac{\Delta(f(x_n)e^{-ikx_n})}{\Delta x} + ik\sum_{n=0}^{N-1} f(x_n)e^{-ikx} + O(\Delta x) && (4.10)\\
&= \frac{1}{\Delta x}[f(x_N)e^{-ikx_N} - f(x_0)e^{-ikx_0}] + ik\hat{f} + O(\Delta x), && (4.11)
\end{aligned}
$$

where $[g](x_n)$ represents a continuous function g evaluated at the discrete set of points x_n and $\Delta f(x_n) = f(x_{n+1}) - f(x_n)$ is the forward difference operator expressing the simplest finite difference representation of a derivative. Enforcing a periodic domain $x_{n+N} = x_n$ we have $f(x_0) = f(x_N)$ and with

$$
e^{-ik_j x_{n+N}} = e^{-ik_j x_n} e^{-ik_j x_N} = e^{-ik_j x_n} e^{-i2\pi j} = e^{-ik_j x_n}, \qquad (4.12)
$$

we retrieve the usual result for the CFT

$$
\mathcal{F}\left(\frac{\partial f}{\partial x}\right) = ik\hat{f}. \qquad (4.13)
$$

The same result can be similarly derived for higher order differences. This derivation demonstrates how periodicity is intrinsic and essential for the DFT to retain the useful algebraic properties of the CFT.

The demonstration above also shows that, in 2D, implementation of shear-periodic boundaries in a spectral method would alter the property Eq. (4.13). Here we notate the coulmnwise Fourier transform as

$$
\check{f}(x, k_y) = \mathcal{F}_x^{-1}(\hat{f}(k_x, k_y)) = \mathcal{F}_y(f(x, y)). \qquad (4.14)
$$

Using the shifting theorem for the DFT, the shear-periodic boundary condition

(Eq. (4.6)) can be written in this half Fourier space as

$$\check{f}(x_N, k_y) = \check{f}(x_0, k_y) e^{-ik_y \omega_s L_x t}. \tag{4.15}$$

Applying this boundary condition to Eq. (4.11) leads to

$$\mathcal{F}\left(\frac{\partial f}{\partial x}\right) = ik_x \hat{f} + i\left[\check{f}(x_0, k_y)(1 - e^{-ik_y \omega_s L_x t})\right], \tag{4.16}$$

which is the analogue of Eq. (4.13) in the shear-periodic regime. With this modification, the DFT of the two dimensional advection-shear problem Eq. (4.2) then becomes

$$\frac{\partial \hat{f}(k_x, k_y, t)}{\partial t} + iv_x k_x \hat{f} + iv_x \left[\check{f}(x_0, k_y)(1 - e^{-ik_y \omega_s L_x t})\right] - k_y \omega_s \frac{\partial \hat{f}}{\partial k_x} = 0, \tag{4.17}$$

which demonstrates that the shear-periodic boundary condition can be implemented numerically in a spectral code. The $\check{f}$ can be expressed as the sum over modes in k_x, but is preferably evaluated using an efficient FFT library. We have implemented this equation in a simple code, and find that in practice the Fourier representation of discontinuities at the real space boundary results in the well known Gibbs phenomenon (spectral ringing, as visible in Fig. 4.3) which can lead to problematic numerical errors. Such errors cannot be completely eliminated, but most of the adverse effects can be ameliorated with a combination of filtering and minimal hyperdissipation (Fig. 4.3). Thus Eq. (4.17) may be numerically time integrated with standard time explicit discretisation schemes by the following algorithm:

1. Apply the filter $\hat{f}'(k_x, k_y) = \mathrm{sinc}^d(k_x)\hat{f}(k_x, k_y)$, with d a real parameter for the filter (which may be adjusted for optimum compromise between conservation and stability).
2. Perform the one dimensional columnwise inverse FFT: $\check{f} = \mathcal{F}_x^{-1}(\hat{f}')$.
3. Compute $iv_x \check{f} = (x_0, k_y)(1 - e^{-ik_y \omega_s L_x t})$.
4. Add the additional boundary condition term along with the rest of the right hand side terms in the explicit time integrator.

The filtering f' is only applied to the boundary condition and not globally, and its use can be further minimised with a dealiasing method which increases the size of the grid in real space FFT. With sufficient grid sizes and minimal hyperdissipation, the method can be stable (though not perfectly conservative) for the simple problem Eq. (4.3). Our derivation used a first order forward finite difference operator at the boundary for simplicity; the same principle can be extended

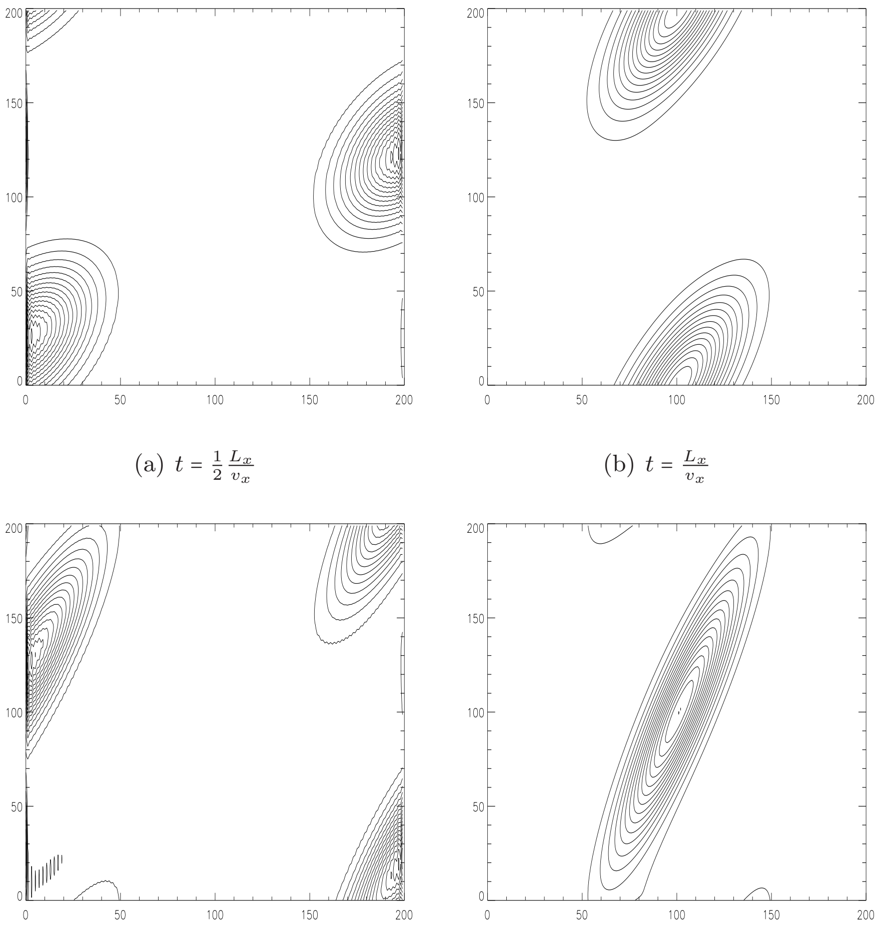

(a) $t = \frac{1}{2}\frac{L_x}{v_x}$

(b) $t = \frac{L_x}{v_x}$

(c) $t = \frac{3}{2}\frac{L_x}{v_x}$

(d) $t = 2\frac{L_x}{v_x}$

Figure 4.3: Numerical solution of Eq. (4.17) using Eq. (4.5) for the shear term and with pseudo-spectral shear-periodic boundary at $x = \{0, 200\}$, and periodic boundary at $y = \{0, 200\}$. The same initial Gaussian, v_x, L_x and ω_S are used as in Fig. 4.2. No dealiasing was used.

to higher order finite differences, but we do not believe this will help to address the problems generated by the spectral ringing. Other techniques for dealing with shocks, discontinuities, and aperiodic boundaries in spectral codes may be of use.

To our knowledge, the shear-periodic boundary conditions as described here have not been used in any spectral turbulence code. Of course, spectral methods are best suited to problems with smooth solutions, and the preferred solution for homogeneous shear flow is to implement the shear-periodic boundary conditions in real space with finite differences. However, for spectral codes which are already well developed, or where the other desirable features of a spectral code outweigh the imperfections of this algorithm, it could present an expedient solution for including sheared flow.

Sadly, in a spectral gyrokinetic flux tube code, there are further considerations which make this algorithm impractical. One key advantage of the spectral representation for a flux tube code is that the gyroaverage operation (which is an expensive multipoint average in real space) is reduced to multiplication by a Bessel function (as described in Sec. 3.4). Whilst our algorithm can cope with structures which pass through the boundary, there is no clean extension of the Bessel function for gyroaverages which occur across the boundary. An implementation of shear-periodic boundaries may be possible (though involved, in the gyroaverage) in a flux tube code which uses finite differences in the radial direction (such as GYRO [112] or GENE [104, 122]).

4.3 Time dependent wavevectors

The problems of implementing the shear periodic boundary condition in a spectral code can be circumvented by moving to coordinates that move with the flow [123–125], in which the 'radial' wavenumbers become time dependent:

$$\psi' = \psi, \qquad \zeta' = \zeta - \psi\bar{\gamma}_E t, \tag{4.18}$$

$$k'_\zeta = k_\zeta, \qquad k'_\psi = k_\psi - k_\zeta\bar{\gamma}_E t. \tag{4.19}$$

(In this section we move from discussing the simple problem Eq. (4.2) to the shearing implemented in GKW, so the notation of the previous section is updated to $(x \to \psi, y \to \zeta)$.) In these coordinates, the derivative in Fourier space in Eq. (4.3) becomes part of the time derivative. In the fluid mechanics community, the standard spectral implementation of homogeneous shear flows uses these coordinates by continually recalculating the wavenumbers, and applying a 'remeshing' of the solution back onto the original wavevector grid at peroidic intervals when the real space grid becomes too deformed [123–126]. An alternative approach avoids the periodic remeshing by absorbing the time dependent wavevector into a time dependent definition of the Fourier transform [127].[2] For a gyrokinetic code, however, these methods are computationally prohibitive, since time dependent wavevectors would require the reevaluation of the linear terms matrix and Bessel functions at every timestep, removing the performance benefits of the matrix-vector multiplication (see Chapter 3).

Therefore, the implementation method we chose for GKW for the work of this

---

[2] Ref. [127] contains an error such that their equation (26) does not agree with our Eq. (4.3), but a cancellation later rectifies this.

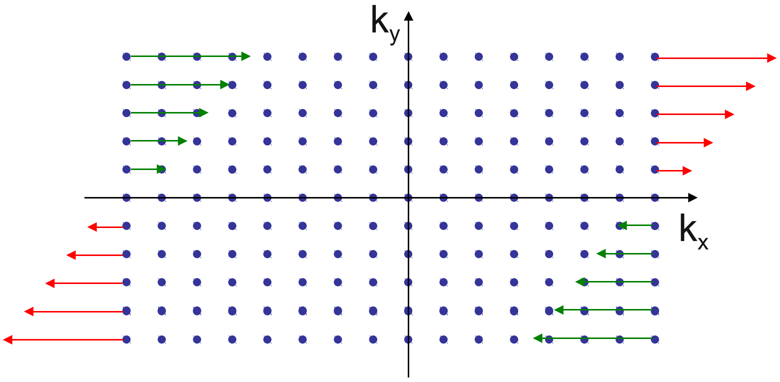

Figure 4.4: Background shear as an advection in wavevector space

thesis is to discretise the time dependence of the wavevectors as a remapping of the solution vector which occurs only when the wavenumber k'_ψ has moved far enough to be closer to the next k_ψ. This method was originally proposed by Hammett et al. in Ref. [128]. Here the 'remeshing' (remapping) of the solution vector occurs continually (and at different times for each k_ζ, Fig. 4.4), and the wavenumbers stay on their original fixed grid. In GKW the remapping is implemented by tracking the number of times each wavevector has been remapped $i_r(k_\zeta)$, and (for $\bar{\gamma}_E > 0$) remapping the solution vector

$$\hat{f}(k_\psi, k_\zeta, s) \to \hat{f}(k_\psi - \Delta k_\psi, k_\zeta, s), \tag{4.20}$$

when the inequality

$$\mathrm{Int}(k_\zeta \bar{\gamma}_E t / \Delta k_\psi) > i_r(k_\zeta), \tag{4.21}$$

is satisfied. Here, Int is the function which returns the *nearest* integer, and $\bar{\gamma}_E$ is the correctly normalised shear rate (defined in the next section). At the low k_ψ limit the solution vector is discarded, which means that the method is nonconservative. However, since the turbulence is characterised by a peaked spectrum (e.g. Fig. 1.6, Fig. 4.10), the losses are negligible if the range of radial wavenumbers is suitably wide. For numerical stability, the remapping must occur at the same time for all points along the s direction of the flux tube. As the metric tensor $\mathcal{E}^{\psi\zeta}$ is a flux function, (Eq. (3.25)), this condition is always satisfied if the shear rate is constant along the field line. The accuracy of the method has been argued to be second order on average [128] and is able to capture the physics effects of a background shear flow whilst allowing the desirable features of the flux tube model to be retained. Convergence of the remap method in L_x/L_y should be checked (particularly for the modes with lowest k_ζ) by decreasing $\Delta k_\psi / k_{\zeta\min}$ (see Sec. 4.6.1 for examples).

4.4 Sheared flow in GKW

In GKW, we implement the equilibrium $E \times B$ flow

$$\mathbf{v}_s(\psi) = \frac{\mathbf{b} \times \nabla \bar{\Phi}}{B} \tag{4.22}$$

which lies inside the flux surface. The shearing rate is defined in the normalised units as

$$\gamma_E^N = \frac{1}{2}\rho_*^2 \frac{\partial^2 \bar{\Phi}_N}{\partial \psi^2}, \tag{4.23}$$

where the normalisation $\bar{\Phi} = \rho_*(T_{\text{ref}}/e)\bar{\Phi}_N$ is as for the perturbed potential Eq. (3.7). The factor $1/2$ is present due to the definition of the reference thermal velocity. Since GKW treats the $E \times B$ shear independently from the centrifugal effects, we use $\bar{\Phi}$ to distinguish the background potential of the shearing from the background potential of the rotating frame, and we also use $\mathbf{v}_s$ to distinguish the equilibrium flow from $E \times B$ drifts due to the perturbations. In physical units the shearing rate is

$$\gamma_E = \frac{v_{\text{thref}}}{R_{\text{ref}}}\gamma_E^N = \frac{1}{B_{\text{ref}}} \frac{\partial^2 \bar{\Phi}}{\partial r^2}, \tag{4.24}$$

where $r = (R_{\max} - R_{\min})/2$. The GKW shearing rate is assumed radially constant and is defined as a flux function. At the radial centre of the flux tube $\mathbf{v_s}$ is chosen to be zero, with the result that there is no net flow over the domain. In the local limit with the approximations of the '$s-\alpha$' model geometry the shearing rate is then equivalent to the familiar definition [129, 130]:

$$\gamma_E \approx \frac{(RB_p)^2}{B_t} \frac{\partial^2 \bar{\Phi}}{\partial \Psi^2} \approx \frac{dv_s}{dr}. \tag{4.25}$$

The flow velocity is normalised as $v_s^N = v_s/v_{\text{thref}}$, and as before the index N is dropped in what follows. The sign convention here is opposite to Eq. (3.8), so $\gamma_E < 0$ corresponds to ∇E_0 radially outwards.

Only the Doppler shift of the background $E \times B$ rotation is kept in the description, i.e. the background flow is added as an additional convective term for the perturbed distribution $(\mathbf{v}_s \cdot \nabla f)$ in the gyrokinetic Eq. (3.71)), and we neglect the acceleration due to the background potential $(\mathbf{v}_s \cdot \nabla \bar{\phi} F_M)$. By omitting the latter term, the flow is implemented in conservative form and provides no drive to the turbulence, so that the stabilising effect may be studied in isolation. If the acceleration term were kept, it would provide a Kelvin-Helmholtz drive to the turbulence. This drive is likely to be small compared to the parallel shear drive (which is kept, in term VIII), but could be the subject of future work. The shear flow could also be self-consistently calculated from the momentum transport so that the full circle of interactions could be closed.

With zero net flow across the flux tube the additional nonlinear term is

$$\mathrm{III.B} = -\mathbf{v}_s \cdot \nabla f \rightharpoonup -\rho_*^2 \frac{\partial \bar{\Phi}}{\partial \psi} \mathcal{E}^{\psi\zeta} \frac{\partial f}{\partial \zeta} = -2\gamma_E \psi \mathcal{E}^{\psi\zeta} \frac{\partial f}{\partial \zeta}. \tag{4.26}$$

Defining $\bar{\gamma}_E = 2\gamma_E \mathcal{E}^{\psi\zeta}$ and taking the Fourier transform, the term can be written as a derivative in Fourier space

$$\mathcal{T}(-\bar{\gamma}_E \psi \frac{\partial f}{\partial \zeta}) = \bar{\gamma}_E k_\zeta \frac{\partial \hat{f}}{\partial k_\psi}. \tag{4.27}$$

The derivative represents a continuous advection (and shearing) in Fourier space in k_ψ which is implemented as described in the previous section.

4.5 Purely toroidal sheared rotation in general geometry

In a tokamak, a sheared $E\times B$ flow can arise as the component perpendicular to the magnetic field of either a poloidal or toroidal flow. Neoclassical collisional mechanisms damp strong poloidal flows, which are neglected in the local equilibrium (as discussed in Chapter 2). From radial force balance, an equilibrium toroidal rotation must be associated with a radial electric field which establishes the $E\times B$ drift $\mathbf{v}_E$ as the perpendicular component of the flow. In this section, we derive the relation between the perpendicular (γ_E) and toroidal (u') shear rates required for a purely toroidal flow, appropriate to the limit of small residual poloidal flow.

For this section only, we adopt the superscript L to represent quantities in the laboratory frame. All quantities without a superscript should be interpreted as being in the rotating frame (as in all other sections). The same coupling condition is derived by two routes to make clear the relationship between the frames.

In Chapter 2, the rotating frame was constructed such that rigid body rotation Ω of the frame matched the plasma rotation ω_φ^L on the local flux surface. The angular rotation then transforms as

$$\omega_\varphi(\psi) = \omega_\varphi^L(\psi) - \Omega \tag{4.28}$$

such that $\omega_\varphi(\psi) = 0$ (and hence $\mathbf{v_s} = 0$) at the centre of the radial domain [57].

4.5.1 In comoving frame

For a purely toroidal rotation, decomposing the toroidal flow into its parallel and perpendicular components gives

$$u_\parallel \mathbf{b} + \mathbf{v_s} = s_\mathrm{B} R\omega_\varphi(\psi) R\nabla\varphi, \tag{4.29}$$

where φ is the toroidal angle. Since Eq. (4.29) is written in the comoving frame, it reads $0 + 0 = 0$ in the centre of the flux tube. From the normalisations above, one can show that in the normalised units

$$\mathbf{v_s} = \frac{1}{2}\rho_*^2 \frac{\mathbf{b}\times\nabla\psi}{B}\frac{\partial\bar{\Phi}}{\partial\psi}. \tag{4.30}$$

Taking the binormal component of Eq. (4.29) we find

$$u_\parallel \underbrace{\mathbf{b}\cdot\nabla\zeta}_{=0} + \frac{1}{2}\rho_*^2 \underbrace{\frac{\mathbf{b}\times\nabla\psi}{B}\cdot\nabla\zeta}_{=2\mathcal{E}^{\psi\zeta}} \frac{\partial\bar{\Phi}}{\partial\psi} = s_\mathrm{B} R^2\omega_\varphi(\psi) \underbrace{\nabla\varphi\cdot\nabla\zeta}_{=-1/2\pi R^2}, \tag{4.31}$$

hence

$$\frac{1}{2}\rho_*^2 \frac{\partial\bar{\Phi}}{\partial\psi} = -\frac{s_\mathrm{B}}{4\pi}\frac{1}{\mathcal{E}^{\psi\zeta}}\omega_\varphi(\psi), \tag{4.32}$$

which upon differentiation gives the coupling relation

$$\underbrace{\frac{1}{2}\rho_*^2 \frac{\partial^2\bar{\Phi}}{\partial\psi^2}}_{\gamma_E} = -\frac{s_\mathrm{B}}{4\pi}\left[\frac{1}{\mathcal{E}^{\psi\zeta}}\underbrace{\frac{\partial\omega_\varphi}{\partial\psi}}_{\mathrm{u}'} + \underbrace{\omega_\varphi}_{=0}\frac{\partial}{\partial\psi}\left(\frac{1}{\mathcal{E}^{\psi\zeta}}\right)\right]. \tag{4.33}$$

Note that the second term on the right is zero when evaluated at the centre of the flux tube. All quantities in the above equation are flux functions, hence the shear rate will always be a flux function, as required for the discrete remapping method.

4.5.2 Relation to laboratory frame

In the laboratory frame Eq. (4.29) becomes

$$u_\parallel^L \mathbf{b} + \mathbf{v}_s^L = s_\mathrm{B} R\omega_\varphi^L(\psi) R\nabla\varphi. \tag{4.34}$$

Taking the binormal component leads to

$$\frac{1}{2}\rho_*^2 \frac{\partial\bar{\Phi}^L}{\partial\psi} = -\frac{s_\mathrm{B}}{4\pi}\frac{1}{\mathcal{E}^{\psi\zeta}}\omega_\varphi^L(\psi), \tag{4.35}$$

and taking the radial derivative gives

$$\frac{1}{2}\rho_*^2\frac{\partial^2\bar{\Phi}^L}{\partial\psi^2} = -\frac{s_\mathrm{B}}{4\pi}\left[\frac{1}{\mathcal{E}^{\psi\zeta}}\frac{\partial\omega_\varphi^L}{\partial\psi} + \omega_\varphi^L\frac{\partial}{\partial\psi}\left(\frac{1}{\mathcal{E}^{\psi\zeta}}\right)\right], \tag{4.36}$$

which has the same form as Eq. (4.33) but different values.

To make explicit the relationships between the quantities, the previous equation is rewritten (using Eq. (4.28)) in terms of the rotating frame quantities. Since the frame rotates rigidly, $\frac{\partial\Omega}{\partial\psi} = 0$ and $\partial\omega/\partial\psi = \partial\omega^L/\partial\psi = u'$. The tensor component $\mathcal{E}^{\psi\zeta}$ is invariant under the transformation. The electric field transforms [57] as

$$\bar{\Phi} = \bar{\Phi}^L + s_\mathrm{B}s_\mathrm{j}\frac{2}{\rho_*^2}\Psi\Omega, \tag{4.37}$$

where Ψ is the (frame independent) poloidal flux with $\nabla\Psi$ radially outward, and the factor of $2/\rho_*^2$ arises from the normalisation of $\bar{\Phi}$ (see Sec. 2.4 for clarification of signs). The coupling condition can then be written as

$$\underbrace{\frac{1}{2}\rho_*^2\frac{\partial^2\bar{\Phi}}{\partial\psi^2} - s_\mathrm{B}s_\mathrm{j}\Omega\frac{\partial^2\Psi}{\partial\psi^2}}_{\gamma_E^L} = -\frac{s_\mathrm{B}}{4\pi}\left[\frac{1}{\mathcal{E}^{\psi\zeta}}\frac{\partial\omega_\varphi}{\partial\psi} + \Omega\frac{\partial}{\partial\psi}\left(\frac{1}{\mathcal{E}^{\psi\zeta}}\right)\right], \tag{4.38}$$

when evaluated in the centre of the flux tube where $\omega_\varphi = 0$. Since $\Psi = f(\psi)$ only, from the relation Eq. (3.26) it follows that

$$\frac{\partial}{\partial\psi}\left(\frac{1}{\mathcal{E}^{\psi\zeta}}\right) = s_\mathrm{j}4\pi\frac{\partial^2\Psi}{\partial\psi^2}, \tag{4.39}$$

hence cancellation gives

$$\underbrace{\frac{1}{2}\rho_*^2\frac{\partial^2\bar{\Phi}}{\partial\psi^2}}_{=\gamma_E} = -\frac{s_\mathrm{B}}{4\pi}\frac{1}{\mathcal{E}^{\psi\zeta}}\underbrace{\frac{\partial\omega_\varphi}{\partial\psi}}_{=u'}, \tag{4.40}$$

which is the same as Eq. (4.33) when evaluated at the centre of the flux tube. The shearing rates in the two frames are therefore related by

$$\gamma_E^L = \gamma_E - s_\mathrm{B}s_\mathrm{j}\Omega\underbrace{\frac{\partial^2\bar{\Psi}}{\partial\psi^2}}_{\mathcal{M}}. \tag{4.41}$$

4.6 Nonlinear background $E \times B$ shear benchmark

Previous work with both gyrofluid and gyrokinetic codes has quantified the quenching effect of background $E \times B$ shear on tokamak turbulence and established the phenomenological relation for the turbulent diffusivity

$$\chi_i = \chi_{i0}(1 - \alpha_E \gamma_E / \gamma_{\max}), \tag{4.42}$$

where α_E is a constant of order unity, and $\gamma_{\max}$ is the maximum linear growth rate of the system in the absence of the sheared flow. The initial gyrofluid results [29, 76, 114] found $\alpha_E \sim 1$, and later gyrokinetic results found $\alpha_E \sim 0.5$ [56, 131–133].[3]

In this section we present a benchmark of our implementation of $E \times B$ shearing against the results of Ref. [133] using the GYRO code [112]. The implementation in GYRO makes use of finite differences in the radial direction, with damped boundary regions allowing for a direct implementation of a non-periodic shear flow in a local domain [132]. Since this method differs significantly from that used in GKW, a benchmark is of interest. Our implementation has also been benchmarked against the GS2 code [21] for the Cyclone case results presented in Ref. [134], with good agreement. Since the numerical implementation of the shearing in GKW and GS2 codes is identical, it is of less interest to present this benchmark here.

The benchmark is for the collisionless Waltz standard case [22, 29, 76] of a deuterium plasma with $R/L_T = 9$, $R/L_N = 3$, electron to ion temperature ratio $T_e/T_i = 1$, mass ratio $\sqrt{(m_i/m_e)} = 60$, safety factor $q = 2$, magnetic shear $\hat{s} = 1$, and inverse aspect ratio $\epsilon = r/R = 0.16$. This case is referred to throughout this thesis as the GA-STD case. Results are presented in the standard gyro-Bohm units where a is the plasma minor radius with $R/a = 3$, $c_s = \sqrt{T_e/m_i}$ is the ion sound speed, $\rho_s = c_s/\omega_{ci}$ is the ion-sound Larmor radius, and $\omega_{ci} = eB/m_i$ is the ion cyclotron frequency evaluated on the magnetic axis.

Both codes are run in the local limit with the model '$s - \alpha$' equilibrium with the MHD parameter $\alpha = 0$. In this geometry, the shearing rate for both codes is equivalent to the familiar definition [129, 130]:

$$\gamma_E \approx \frac{(RB_p)^2}{B_t} \frac{\partial^2 \Phi}{\partial \Psi^2} \approx \frac{dv_E}{dr}, \tag{4.43}$$

where Ψ is the poloidal flux. The values of the maximum linear growth rate $\gamma_{\max}$ and other linear properties for the simulations of this case are given in Table 4.1 and

---

[3] It appears that the elimination of the boundary discontinuity discussed in Sec. 4.2 altered the result from $\alpha_E = 1.18$ in Ref. [29] to $\alpha_E = 0.69$ in Ref. [114], thus some of the difference may not be between gyrofluid and gyrokinetic, but due to the boundary conditions.

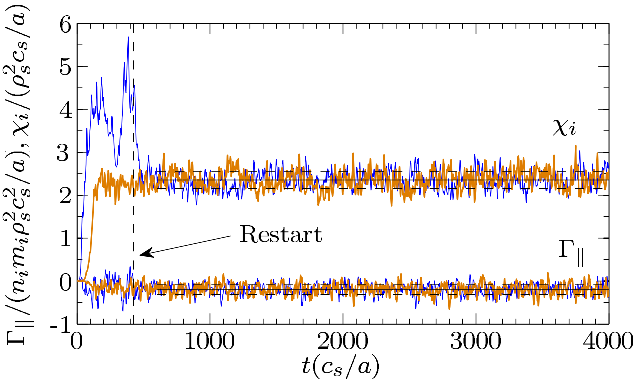

Figure 4.5: Time traces of ion heat diffusivity and momentum flux for the restart method (blue, thin) compared to a run without restart (orange, thick) with $\gamma_E = 0.118(c_s/a)$ with means and variances $\bar{\chi}_i = (2.354 \pm 0.202, 2.353 \pm 0.218)$ and $\bar{\Gamma}_\parallel = (-0.191 \pm 0.119, -0.188 \pm 0.127)$ for the restart and non-restart methods respectively.

results in this section are presented in terms of $\gamma_E/\gamma_{\max}$. The spectrum of linear growth rates is shown in Fig. 4.13.

In simulations with a high $E \times B$ shear rate, the linear growth can be suppressed such that the simulation takes an impractically long time to reach the nonlinear saturated state, or in some cases never will. However, if the simulation is initialised without background $E \times B$ shear, and the shear is applied once the nonlinear phase is reached, then the system will quickly reach a new saturated state. In the case where linear growth is completely suppressed, this state is referred to as 'subcritical' or 'self-sustained' turbulence [135–137], and has been conjectured to play a role in transport bifurcations leading to transport barriers [76, 138]. If the turbulence is not in this state (i.e linearly unstable with $E \times B$ shear), we find that the statistical properties of the saturated nonlinear state are unaffected by the path taken to get there (Fig. 4.5). All results presented here are obtained with the restart method for larger γ_E , and all time averages are taken over a minimum range of $t_{av} = 1600(a/c_s)$ after the new saturated state was reached, unless otherwise specified.

Unless otherwise stated, all simulations with adiabatic electrons are performed with $N_{\text{mod}} = 16$ binormal modes and $N_x = 83$ radial modes. The maximum wavevector has binormal wavenumber $k_\theta \rho_s = 0.75$ where k_θ is evaluated at the outboard midplane and ρ_s is evaluated at the magnetic axis. The mode spacing gives a perpendicular simulation domain of extent $[L_{\text{radial}}, L_{\text{binormal}}] = [120, 126]\rho_s$. The number of grid points in parallel velocity, magnetic moment, and along the field line are $N_{v\parallel} = 16$, $N_\mu = 8$ and $N_s = 16$ respectively. These grid sizes have proved sufficient to investigate the physics phenomena. The adiabatic results (away from the critical shear region) are well converged in N_s, N_μ and N_x, and $N_{v\parallel}$, and to within 10% in N_{mod} (increasing L_{binormal}).

All simulations with kinetic electrons are performed with $N_{\mathrm{mod}} = 21$ binormal modes with a maximum $k_\theta \rho_s = 1.0$, and $N_x = 167$ radial modes with a perpendicular simulation domain of extent $[L_{\mathrm{radial}}, L_{\mathrm{binormal}}] = [120, 126]\rho_s$. The number of points in the parallel velocity is increased to $N_{v\parallel} = 32$ as compared with the adiabatic case. The kinetic results are well converged in N_s, N_μ and N_x, and to within 20% in N_{mod} (increasing L_{binormal}) and $N_{v\parallel}$. These convergences are for cases without strong shear, convergence in the critical shear region is examined in the next section. Except where stated otherwise, all results presented in this section are for adiabatic electrons.

The resolution used in the GKW simulations is chosen to be comparable to the GYRO gridsizes used in Ref. [133] (though it should be noted that the numerics of the codes are different). In particular, both sets of results were obtained with $N_{\mathrm{mod}} = 16$ binormal modes over the same range of wavenumbers.

The correspondence between the linear growth rates predicted by GKW (Table 4.1) and GYRO (Ref. [133], Table I) is nearly exact. The comparison between the two codes for the nonlinear turbulent ion diffusivity quenching with shearing is shown in Fig. 4.6, and the GKW results are summarised in Table 4.2. As is standard, for these simulations (and those in Chapter 5), GKW was run with no hyperdissipation perpendicular to the field, and a small amount of hyperdissipation in the finite difference directions (s and $v_\parallel$) which stabilises the numerics ($\alpha_s = 1.8, \alpha_{vp} = 1.8$). Both the GKW and GYRO simulations are collisionless, and both codes use the restart method to access the self-sustained turbulence region.

It can be seen that GKW ion heat diffusivities are up to 25% higher, and that there is some disagreement between the codes in the critical shear region where the turbulence becomes completely suppressed. These differences are investigated in more detail in the next section. Notwithstanding the above, GKW and GYRO give good agreement for the turbulence quench relation (Eq. (4.42)) with close concurrence on the important parameter $\alpha_E \approx 0.4 - 0.6$ (depending on the case) which quantifies the strength of the shear suppression. This agreement gives good confidence in the qualitative physics predicted by both codes.

For adiabatic electrons, the benchmark was also conducted including the destabilising effect of parallel velocity shear $u' = 12\gamma_E$ consistently for purely toroidal rotation, also shown in Fig. 4.6. Here too the codes give good agreement, both predicting a minimum in the heat transport at $\gamma_E = 2\gamma_{\mathrm{max}}$.

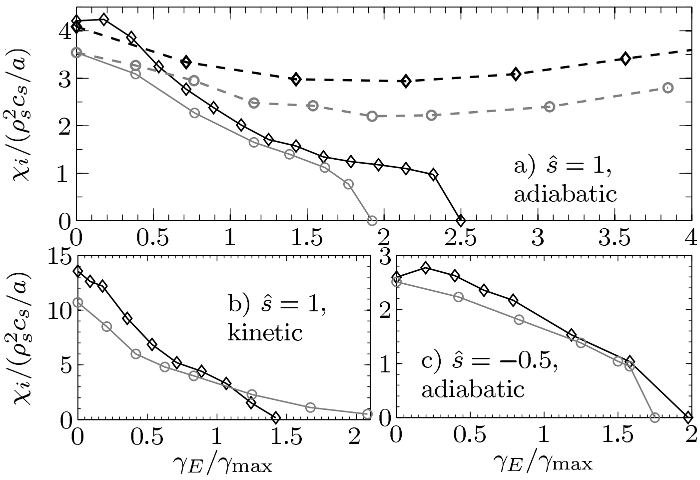

Figure 4.6: GKW benchmark of background $E \times B$ shear with GYRO for the GA-STD case. GKW results (diamonds) for a) adiabatic electrons, b) kinetic electrons, and c) adiabatic with $\hat{s} = -0.5$, are compared to the equivalent GYRO results (circles) from Tables II, III, IV and V of Ref. [133]. The dashed lines in a) include coupled parallel velocity shear for purely toroidal rotation with $u' = 12\gamma_E$. Standard dissipation, $[\alpha_x, \alpha_s, \alpha_{vp}] = [0.0, 1.8, 1.8]$.

4.6.1 Effect of resolution and dissipation

As was noted in Ref. [133], the region near the critical shear is difficult to resolve properly, indeed this is the region in which the two codes show worst agreement. A convergence study in N_{mod} and N_x in the critical shear region for the adiabatic case was undertaken with GKW. Simulations conducted with higher perpendicular resolution ($k_\theta \rho_s$ up to 8.05 and $k_\psi \rho_s$ up to 16.9) indicate that the region near the critical shear is sensitive to this resolution, with a longer 'tail' in the residual turbulent flux at high shear rates ($\gamma_E/\gamma_{\max} > 2$), as compared with the lower resolution results (Fig. 4.7). This is not surprising since the effect of the $E \times B$ shear is to break up structures, pushing the turbulence to smaller scales. The results initially indicate that this tail is 'converged' when the maximum resolved scales are $k_\theta \rho_s = 4.05$ and $k_\psi \rho_s = 4.2$ and higher, but as we show later, this convergence does not mean the result is physical. Whilst the shearing acts to directly increase only the k_ψ scales, nonlinear mixing also results in a similar resolution requirement in the binormal direction. (For kinetic simulations containing trapped electron modes extended along the field, greater radial resolution is usually required due to the magnetic shear coupling (Sec. 3.4.1), even in the absence of $E \times B$ shear.)

As discussed above, for the wavevector remapping method, convergence in radial resolution $L_{\mathrm{radial}}/L_{\mathrm{binormal}}$ should be checked; Fig. 4.8 demonstrates the results are well converged for the low shear cases when the remapping occurs most

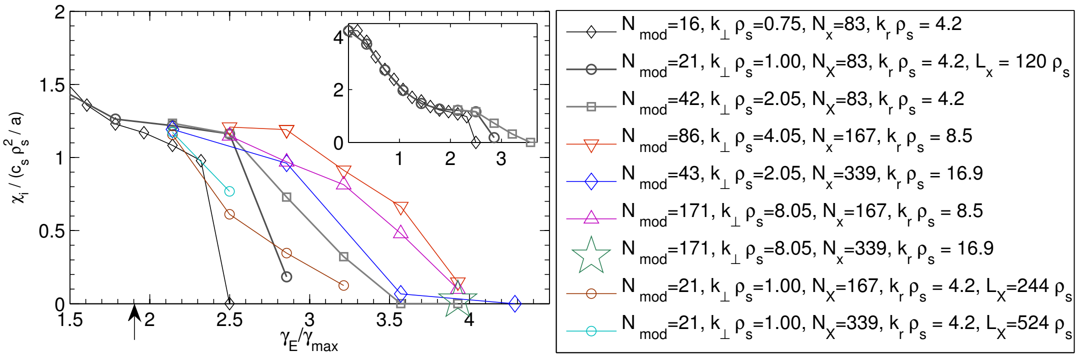

Figure 4.7: GKW results investigating the effect of increased perpendicular resolution in the critical shear region (without collisions or perpendicular dissipation). Time averages are over at least $t_{av} = 300(a/c_s)$, due to expensive nature of these computations and the low variance for these points. Standard dissipation, $[\alpha_x, \alpha_s, \alpha_{vp}] = [0.0, 1.8, 1.8]$. Here $k_\perp$ refers to maximum k_θ.

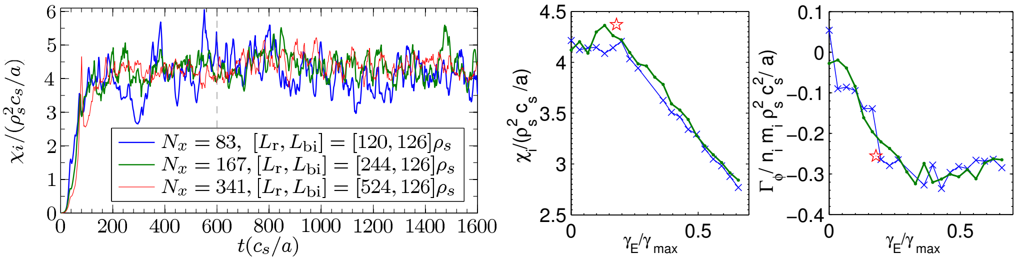

(a) $\gamma_E = 0.19\gamma_{\max}$, applied from $t = 0$.

(b) $\gamma_E = (0, 0.65)\gamma_{\max}$, same legend colours.

Figure 4.8: $L_{\mathrm{radial}}/L_{\mathrm{binormal}}$ convergence check of the $E\times B$ shearing implemented in GKW, with L_{binormal} held constant for small γ_E, when the remapping is infrequent. The averages over $t_{av} = 1000(a/c_s)$ for a) are $\bar{\chi}_i^{120}(a/c_s\rho_s^2) = 4.16 \pm 0.50$, $\bar{\chi}_i^{244}(a/c_s\rho_s^2) = 4.38 \pm 0.38$, $\bar{\chi}_i^{524}(a/c_s\rho_s^2) = 4.42 \pm 0.29$, with increasing L_{radial}. The variance decreases with increasing L_{radial} (since the average is over a larger domain) but the χ_i mean is converged to within 5% for $\gamma_E > 0.19\gamma_{\max}$. In b) the time averaged fluxes demonstrate that the results are well converged as the effect of the shear increases. The average momentum fluxes are close to zero (see Fig. 4.5), so their variance is relatively large.

infrequently. For the simulations with adiabatic electrons at lower resolutions, there is a sharp transition from the self-sustained turbulent state at the high shear limit. The convergence in $L_{\mathrm{radial}}/L_{\mathrm{binormal}}$ for these points is shown in Fig. 4.7 and Fig. 4.9; increased L_{radial} gives a smoother end to the tail and eliminates the sharp transition, but does not move the critical point at which the turbulence is suppressed. Very close to the critical shear therefore, the discrete nature of the shearing implementation allows turbulence to persist in the time between the remapping.

To investigate further if the tail in the turbulent heat flux at high shear is physical, we attempted to improve on the benchmark between GKW and GYRO. In an effort to better understand the differences, a few test simulations were made with GYRO, concentrating on the adiabatic case with $\hat{s} = 1$.[4]

We began by trying to understand the 17% difference in diffusivity at zero $E{\times}B$ shear (Fig. 4.6). Both codes are well converged for the adiabatic results (with the slight exception of the number of binormal modes, for which $N_{\mathrm{mod}} = 16$ was used in both for the benchmark) By running GYRO in flux tube mode with periodic boundaries, it was checked that the non periodic radial damped boundaries do not make any difference to the result at zero $E{\times}B$ shear (this cannot be checked at finite $E \times B$ shear, but convergence in L_{radial} could be checked instead). However, runs with newer GYRO did yield a result within 8% of the original GKW result (Fig. 4.9), (indeed a point close to this appears in Fig. 2 of Ref. [133], but not in the data table.)

As the next step to eliminate differences between the codes, we attempted to match numerical dissipation. GYRO uses a finite difference scheme in the radial and parallel directions with a (upwinding) dissipation which is equivalent to a hyperdiffusive term $\sim \alpha_{r,\theta} k^4/k^4_{\mathrm{max}}$ (Here θ is used for the GYRO parallel coordinate to distinguish it from GKW). GKW uses a similar scheme in the parallel s direction, but the spectral radial direction is usually dissipation free, with some high k filtering introduced by the dealiasing procedure. To try to match GYRO more closely, a spectral hyperdiffusive term $\sim \alpha_{x,y} k^4/k^4_{\mathrm{max}}$ was introduced into GKW. Since the velocity grids in the codes are rather different, matching velocity dissipation directly was not possible. We also attempted to match the codes by eliminating numerical dissipation and introducing a physical dissipation in the form of an ITER-like ion-ion collision rate $\nu_{ii} = 0.01(c_s/a)$.

The GKW results show that the critical shear region is also very sensitive to dissipation (Fig. 4.9). By including radial dissipation matched (as far as possible) to GYRO, the agreement between the codes is improved. At zero shear, and intermediate shear, exact agreement is found, but some differences remain at low shear and high shear. The GKW results indicate that radial dissipation, velocity space dissipation and collisions tend to reduce the turbulent tail, whilst parallel dissipation tends to increase it. We speculate that near the critical shear, any instability that survives is strongly localised in the parallel direction, which may cause numerical problems for the parallel dissipation. This is evidenced by a reduction in the tail for the simulations with $\alpha_s > 0$ when the parallel resolution is increased. Furthermore, the strong anisotropy of the turbulence prevents parallel (spatial or velocity) dissipation from being translated to dissipation at the smallest perpendicular scales,

---

[4] Thanks to W. Guttenfelder for running the GYRO simulations.

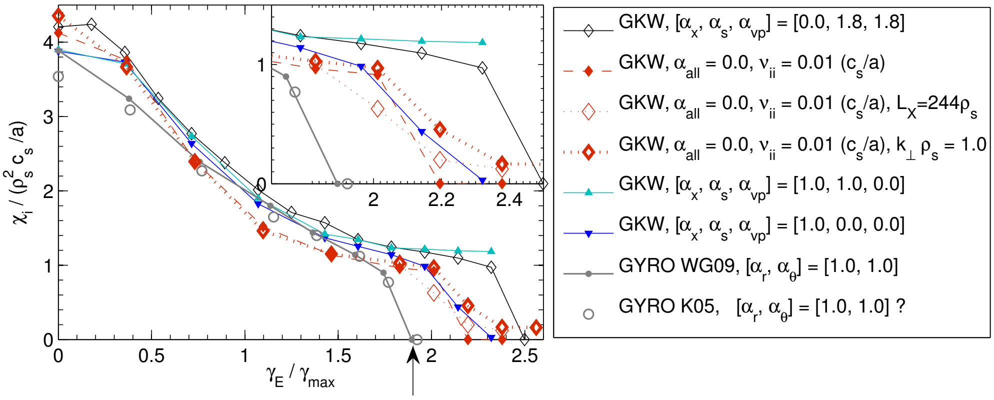

Figure 4.9: GKW results with varied dissipation and collisions, compared to GYRO results. K05 refers to GYRO results from Table II of Ref. [133], and WG09 refers to the same simulations repeated with a 2009 version of GYRO. For these results the original resolution (with $N_{\mathrm{mod}} = 16$) as described in Sec. 4.6 was used (except where indicated for the collisional runs).

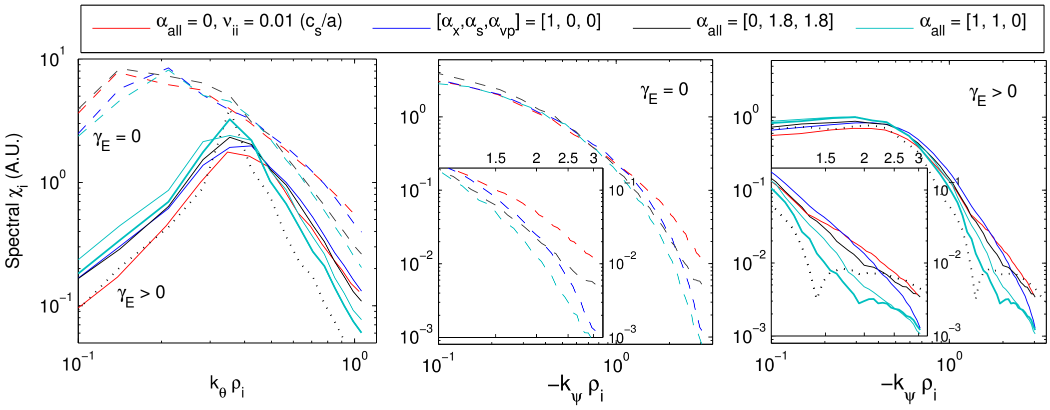

Figure 4.10: Spectra for the GKW results presented in Fig. 4.9 at zero shear (dashed), $\gamma_E/\gamma_{\max} = 1.8$ (solid), and $\gamma_E/\gamma_{\max} = 2.35$ (thick line and dotted line). The dotted line is for the case resolving up to $k_\theta\rho_s = 4.05$ and $k_\psi\rho_s = 8.5$. The k_ψ spectrum shown is the half which the turbulence is being pushed towards by the shearing. The curves plotted are the individual fluxes for each mode, and the colour scheme is the same as in Fig. 4.9.

but the coupling of the two perpendicular scales through the nonlinear terms means that dissipation applied radially is quickly mixed into the binormal direction.

From the spectra for these simulations, we note that the increased flux in the cases with the longer tail comes from the largest scales, and that these cases actually have less flux at the smallest wavelengths (Fig. 4.10). Unsurprisingly, radial dissipation alters the shape of the radial (and binormal) spectra at the smallest scales, and the cases with collisions have the flattest spectra (i.e. the cleanest turbulent cascade). In the cases with strong $E{\times}B$ shear and parallel dissipation, a tendency for the k_ψ spectrum to get less steep at the smallest scales is amplified, and for the most extreme cases there can even be an upturn in the spectrum (corresponding to those with the longest tail in Fig. 4.9). This indicates a bad numerical artifact, which can cause higher overall flux at the larger scales through the inverse cascade, hence the longer tail results should be regarded as nonphysical. Note however, that these cases are not underresolved, since the cases of Fig. 4.7 with the highest resolution (which appear to converge) actually show this artefact most severely (Fig. 4.10, dotted line). The cases with collisions or radial dissipation only do not have this problem, which indicates that the problem is exacerbated by parallel dissipation; when the parallel resolution is increased, the problem is mitigated and a good spectrum is obtained. We theorise that numerical problems associated with strong parallel localisation can lead to incorrect results due to a problem in the nonlinear cascade which can be identified in the spectrum.

Whilst improved agreement might be achieved by increasing the GKW radial dissipation, the ideal benchmark should focus on achieving fully converged results for both codes for the case with physical collisions and minimal numerical dissipation. With this aim in mind, the GKW collisional results were also convergence tested in the critical shear region, and are well converged in N_s, L_x and maximum binormal $k_\theta \rho_s$ (Fig. 4.9). The collisional case has less sensitivity to the maximum $k_\theta \rho_s$ than the collisionless results of Fig. 4.7, and does not suffer from a (visible) numerical artefact in the radial spectrum (Fig. 4.10). We believe therefore that the GKW collisional results are both physical and well converged.

The first point where the turbulence remains in GKW but is completely quenched with GYRO, is at $\gamma_E/\gamma_{\max} = 1.9$. For this point, some preliminary GYRO simulations were also conducted with different box sizes and resolution, and with varied dissipation coefficients (Fig. 4.11). With the exception of the zero dissipation case, the GYRO results at this point all show complete turbulence quenching, even when increasing the radial box size or binormal resolution. The zero dissipation case is unphysically unstable since the GYRO entropy diagnostic [139] shows unconstrained entropy growth in the phase before the $E \times B$ shear, and both GKW and GYRO find a non stationary spreading in the k_ψ spectrum (not shown). However, we do not believe the *same* problem is occurring in the GKW simulations which show nonzero turbulence at this point, since the GKW spectra for these results are stationary (Fig. 4.12). Further verification of a good statistical state for the GKW results would require implementation of new diagnostics (entropy / vorticity) in GKW.[5]

---

[5] Understanding the turbulent cascade and the relationship between dissipation, energy conservation, and the steady state is currently an active and controversial area of research well beyond the scope of this thesis [108, 109, 137].

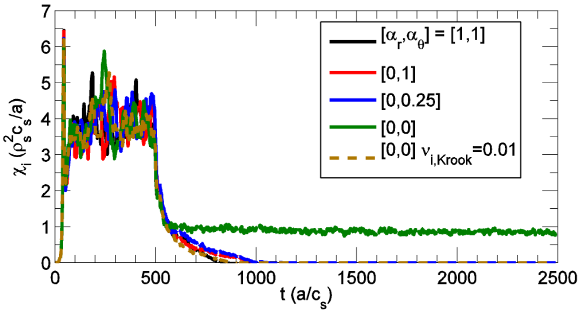

Figure 4.11: b) GYRO time traces for the restart method with different dissipation coefficients and collisions (dashed). The shear is $\gamma_E/\gamma_{\max}$ = 1.9, corresponding to the point marked with the arrow in Fig. 4.9. Figure courtesy of W. Guttenfelder.

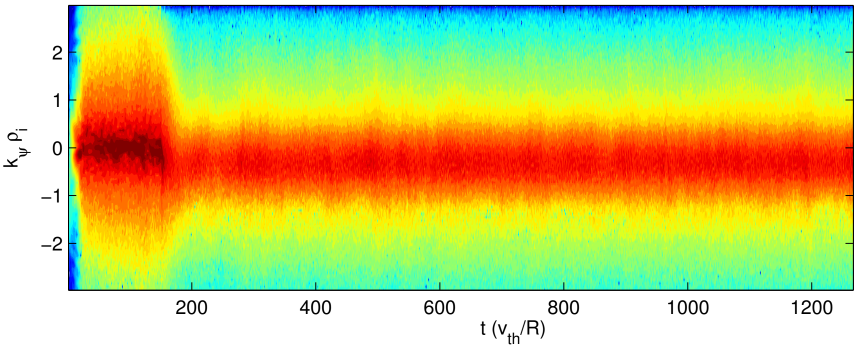

Figure 4.12: Time-contour plot of the χ_i spectrum (logarithmic scale, A.U.) for the collisional case in GKW with shear $\gamma_E/\gamma_{\max}$ = 1.8 applied at $t = 150(R/v_{th})$.

It appears that the GKW parallel dissipation α_s plays a different role to the GYRO parallel dissipation α_θ, again probably due to the different grid implementation. Even with radial dissipation, GKW still has a tendency to predict a longer tail than GYRO, which may be explained by the difficulty of matching resolution and dissipation between codes with different numerics; in particular, the parallel velocity grid and radial numerics differ significantly between the codes.

The benchmark is incomplete, since we have only been able to thoroughly investigate the convergence of the GKW results. However, it is expected that exact agreement could be achieved by conducting extensive convergence testing of the collisional case for both codes. We believe the current remaining difference could be explained by differences in the velocity grid dissipation, the collision operator, or a minimal cascade problem in GKW. The GS2 code is very similar to GKW, with an identical implementation of the $E \times B$ shear, and with differences mainly in the velocity grid. Including GS2 results in this benchmark might help to isolate the source of the remaining differences with GYRO.

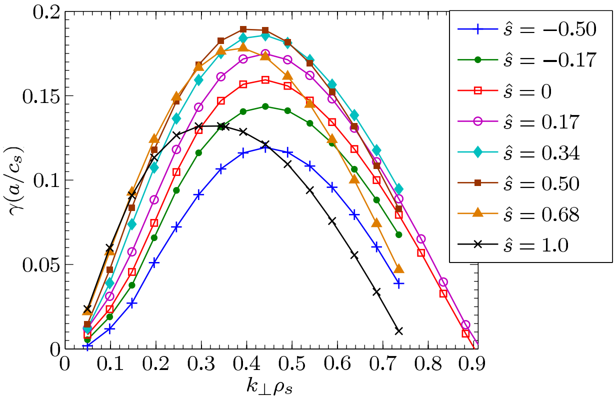

Figure 4.13: (Colour online) Adiabatic ITG growth rate spectra for different values of $\hat{s}$. For values of $\hat{s} > 0.5$, the spectrum peaks at lower $k_\theta \rho_s$.

To summarise, investigations with GKW have shown turbulence quenching by $E \times B$ shearing to be very sensitive to resolution and numerical dissipation in the region of the critical shear. These parameters should therefore be carefully considered when drawing conclusions in the realm of self-sustained turbulence (for example Ref. [138]). In the case of GKW, investigation of the spectral radial fluxes has revealed that the best results are obtained by minimising parallel dissipation and including either radial dissipation or collisions. When these factors are taken into account, very good (though not perfect) agreement between GKW and GYRO is found.

4.7 Parametric dependence of shear quench

In Ref. [133] it was noted that the $\hat{s} = -0.5$ case showed a weaker dependence on γ_E than the $\hat{s} = 1$ reference case, and that results for more values of $\hat{s}$ were needed to elucidate this dependence further. For the work in Chapter 5 a fine scan over the magnetic shear is conducted, and these results can also be used to address this question. The growth spectra for each of these cases is shown in Fig. 4.13 and results for the ITG quench rule for various $\hat{s}$ are shown in Fig. 4.14(a). Whilst the transport differs at zero γ_E, the results indicate that for $0.5\gamma_{\max} < \gamma_E < 1.5\gamma_{\max}$ the $E \times B$ shear dominates the magnetic shear in regulating the turbulence and there is little variation of the transport with $\hat{s}$. The shear quench parameter α_E can also be estimated from these results. As discussed above, the value of the critical shear for which the turbulence is completely quenched is sensitive to the resolution and dissipation in the simulation, so values of $\gamma_E^{\text{crit}}/\gamma_{\max} = 1/\alpha_E^{\text{crit}}$ should be treated with some caution. We therefore also estimate α_E^{grad} from a line drawn through $\chi_i(\gamma_E = 0)$ and $\chi_i(p)$, where p is the last point before the sharp transition, since

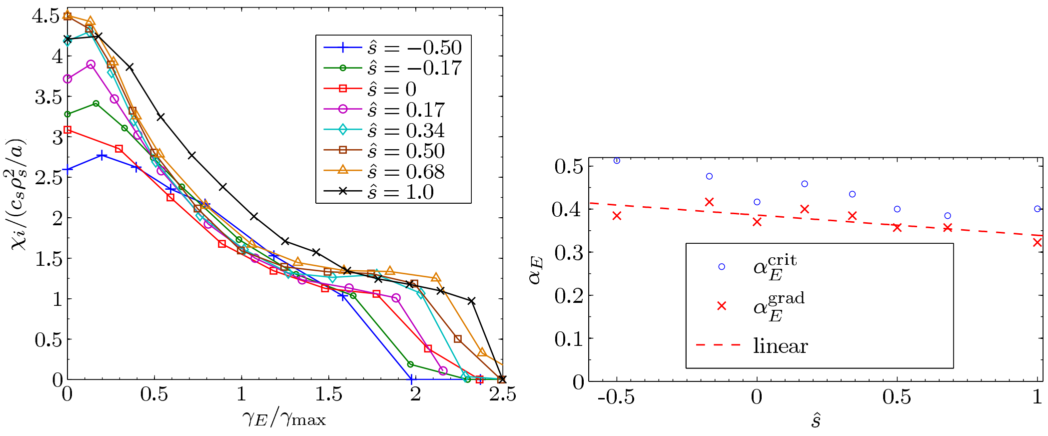

(a) Ion thermal diffusivity against shear rate

(b) Variation of quench rule with $\hat{s}$

Figure 4.14: $E\times B$ quenching of turbulent transport for various $\hat{s}$. In b), the linear fit has equation $\alpha_E^{\text{grad}} = -0.047\hat{s} + 0.39$.

Fig. 4.7 indicates that this point is less affected by the resolution. Whilst we note that this estimate is somewhat arbitrary, within the framework of the established linear quench rule, the values estimated show at least that α_E varies only slowly with $\hat{s}$ (Fig. 4.14(b)).

In Sec. 5.8, a case of pure TEM turbulence (labeled PURE-TEM) is presented, for which the $E\times B$ shear quench still occurs but at higher shearing rates with $\alpha_E \sim 0.2$ (Fig. 5.8(b)), as compared to $\alpha_E \sim 0.4$ for the GA-STD case. In the PURE-TEM case, the peak in the transport is at smaller scales (Fig. 5.8(d)), so higher $E\times B$ shearing rates are needed for turbulence suppression. These results therefore demonstrate whilst that the shear quench parameter α_E may be insensitive to variation in plasma geometry parameters such as the magnetic shear, a fundamental change in turbulence regime can significantly alter its value. This is not surprising since it is already known that the self consistent shearing generated by zonal flows has less effect on TEM turbulence than on ITG turbulence [34, 140]. It is also worth noting that since the scales which dominate nonlinear transport have no direct relation to the fastest growing mode, we should not expect the critical shearing rate to be related to this growth rate (indeed it is not clear that normalising the shearing rate with the linear growth rate of any single mode would provide a more consistent quench rule).

The effect of $E\times B$ shearing is not limited to the ion thermal transport, since the suppression of turbulence affects all turbulent transport channels. In addition, the $E\times B$ shear also breaks a symmetry in the gyrokinetic equation, resulting in a nondiffusive component in toroidal angular momentum transport. This symmetry breaking mechanism is examined and quantified in the next chapter.

Table 4.1: Most unstable linear modes: Growth rate $\gamma_{\max}$, with corresponding mode frequency ω and scale $k_\theta \rho_s$. Positive values of ω indicate propagation in the ion diamagnetic direction.

$\hat{s}$	$\gamma_{\max}(a/c_s)$	$\omega(a/c_s)$	$k_\theta \rho_s$
Adiabatic electrons			
-0.50	0.119	0.272	0.44
-0.17	0.144	0.278	0.44
0.00	0.159	0.286	0.44
0.17	0.175	0.303	0.44
0.34	0.186	0.313	0.43
0.50	0.190	0.329	0.40
0.68	0.178	0.330	0.38
1.00	0.132	0.296	0.31
Kinetic electrons			
1.00	0.265	0.324	0.28

Table 4.2: Representative nonlinear results for $\hat{s} = 1$ with mean and variance of saturated quantities. The ± figure is the variance of the nonlinear fluctuations, not an error measure. The length of the time averages is such that estimation of the error using two different averaging windows gives invisible error bars on most of the plots (with the slight exception of $M_\parallel$ calculations near $\gamma_E = 0$, e.g. Fig. 4.8).

$\gamma_E(a/c_s)$	$\bar{\chi}_i(a/c_s\rho_s^2)$	$\bar{\Gamma}_\parallel/n_i m_i(\rho_s c_s/a)^2$
Adiabatic electrons	$t_{av} = 1600(a/c_s)$	$t_{av} = 1600(a/c_s)$
0	4.21 ± 0.65	-0.045 ± 0.297
0.047	3.86 ± 0.42	-0.269 ± 0.257
0.094	2.77 ± 0.24	-0.220 ± 0.149
0.141	2.02 ± 0.16	-0.143 ± 0.095
0.189	1.57 ± 0.12	-0.071 ± 0.060
0.236	1.24 ± 0.08	-0.018 ± 0.043
0.283	1.10 ± 0.09	-0.001 ± 0.032
0.306	0.97 ± 0.14	0.004 ± 0.031
0.330	0	0
Kinetic electrons	$t_{av} = 255(a/c_s)$	$t_{av} = 255(a/c_s)$
0.000	13.56± 2.95	0.446 ± 0.985
0.047	12.20± 3.13	-1.024 ± 0.579
0.094	9.24 ± 1.67	-1.232 ± 0.570
0.141	6.86 ± 1.07	-0.904 ± 0.403
0.189	5.20 ± 0.59	-0.615 ± 0.234
0.236	4.42 ± 0.49	-0.558 ± 0.173
0.283	3.30 ± 0.44	-0.396 ± 0.120
0.330	1.55 ± 0.17	-0.164 ± 0.045
0.377	0	0

Table 4.3: Representative nonlinear results for $\gamma_E = 0.141(c_s/a)$ with mean and variance of time averaged saturated quantities.

$\hat{s}$	$\bar{\chi}_i(a/c_s\rho_s^2)$	$\bar{\Gamma}_\parallel(a/c_s\rho_s^2)$
Adiabatic electrons		
-0.50	1.53 ± 0.10	-0.143 ± 0.095
-0.17	1.73 ± 0.11	-0.193 ± 0.109
0.00	1.68 ± 0.13	-0.181 ± 0.107
0.17	1.92 ± 0.15	-0.166 ± 0.088
0.34	2.03 ± 0.20	-0.096 ± 0.074
0.50	2.11 ± 0.18	-0.066 ± 0.055
0.68	2.15 ± 0.18	0.046 ± 0.056
1.00	2.02 ± 0.16	0.124 ± 0.046

Chapter 5

Angular momentum transport by sheared flows

5.1 Introduction

A growing body of experimental evidence [42, 116, 141–150] now demonstrates that tokamak plasmas can exhibit toroidal rotation even in the absence of an external torque. This 'spontaneous' (or 'intrinsic') rotation has generated much recent theoretical attention on mechanisms of anomalous momentum transport beyond the diffusional paradigm [44–46, 56, 57, 72, 117, 133, 151–169]. The theory of turbulent toroidal momentum transport is not yet complete, but a number of the components already identified will be important in a comprehensive description.

Using symmetries in the local gyrokinetic equation, it was shown in Refs. [44, 117, 170] that the net transport of toroidal angular momentum must be zero for axisymmetric nonrotating plasmas with up-down symmetric flux surfaces. By breaking the symmetry assumptions of this derivation, the contributions to the momentum transport in the local limit (1-4 below) have all been systematically identified [117]. In a global model, the symmetry arguments used at $\mathcal{O}(\rho_*)$ do not hold, and many more mechanisms can contribute to the momentum transport (5-6 below). The origin of each contribution can be traced to a particular symmetry breaking mechanism, and can also be viewed in the framework of wave-particle momentum exchange [160].

It is clear that many of the mechanisms of momentum transport do not fit easily into the transport matrix (Eq. (1.28)), yet its persistence as a paradigm means that the nondiffusive contributions to transport are often referred to as 'off-diagonal'. Here, we reserve 'pinch' to refer to a transport term proportional to the quantity that is being transported (only item 2 below). In fluid terminology, nondiffusive, nonpinch terms are often referred to as 'residual stress'. The symmetry breaking mechanisms leading to angular momentum transport so far identified are:

1. A gradient in the plasma parallel velocity, which naturally leads to diffusive parallel momentum transport [44, 152, 161, 171].

2. In a plasma with an existing rotation, parallel velocity symmetry is broken by the Coriolis drift. The resulting phase difference between density and velocity fluctuations generates a pinch of parallel momentum which can sustain finite rotation gradients in a source free region [45, 57, 155, 156, 172, 173]. In the laboratory frame, the particle flux also enters into the momentum flux (Eq. (3.93)). The Coriolis pinch also includes a contribution due to $E \times B$ compression which is sometimes described within the framework of 'turbulent equipartition' [159, 164, 165].

3. A nondiffusive, nonpinch contribution to parallel momentum transport due to sheared background $E{\times}B$ flow was first identified in a sheared slab quasilinear model in Ref. [151] and later in more advanced models [56, 133, 157, 158]. The quantitative investigation of this residual stress is the focus of this chapter.

4. Flux surface shaping asymmetric about the horizontal axis (typical in single null plasmas) breaks the up-down symmetry of the plasma, and has been shown to generate net momentum transport, greatest near the plasma edge, which can provide a 'seed' rotation mechanism to build an initial rotation gradient in the outer core [46, 163, 174, 175].

5. In a global model, the radial symmetry of the local model does not exist, and a number of additional mechanisms at order $\mathcal{O}(\rho_*^2)$ lead to momentum transport, as has been evidenced in global gyrokinetic simulations [117, 154, 166, 167]. The mechanisms isolated to date include the parallel velocity nonlinearity [72, 176, 177], a gradient in the turbulence intensity [178], and a shift in the mode maximum from the low field side (nonzero θ_0) due to profile shearing [179]. The relative importance of these contributions remains to be determined, and more may yet be forthcoming.

6. The inclusion of the parallel flows of the true neoclassical equilibrium breaks the symmetry and can lead to momentum transport [169, 180]. Neoclassical flows can be kept in the local model if the neoclassical term (VI in Eq. (3.71)) and collisions are kept, but do not generate momentum transport in the usual local model ordering as they do not appear in the equilibrium (as discussed in Sec. 2.7.1).

The above mechanisms determine only the radial transport of toroidal angular momentum; the total angular momentum is always conserved. If the plasma gains a net spontaneous rotation there must also be an interaction with the wall which transfers momentum from the vessel (and the Earth). The specifics of these interactions in the edge and the scrape-off layer are outside the scope of core transport models. Mechanisms 1-3 all depend on the direction of an existing rotation and cannot determine a preference for rotation in a particular direction, but together they determine the form of the rotation profile.

The focus of this chapter is on the third of the above mechanisms; the contribution of sheared $E\times B$ flow to momentum transport. A sheared toroidal rotation has a perpendicular shear component γ_E^{tor}, which is coupled to a parallel shear component $u'_{\|}$, as described in Sec. 4.5. Sheared $E\times B$ flow can also be present independent of $u'_{\|}$, as the perpendicular component of a sheared poloidal flow. Sheared poloidal flow arises neoclassically as a gradient in the diamagnetic flow with $\gamma_E^{\mathrm{neo}} \propto (1/B)\mathrm{d}^2p/\mathrm{dr}^2$, and any anomalous poloidal flow is usually damped to the neoclassical level (e.g. [145]). The values of γ_E^{neo} are formally one order smaller in ρ_* than γ_E^{tor}, but steep gradients in the region of transport barriers can lead to comparable values. In the literature, the $E\times B$ momentum transport term has been discussed as both a diffusive correction and a residual stress, depending on the assumed origin of the $E\times B$ shear flow.

Global fluid simulations of internal transport barriers (ITBs) have included the $E\times B$ contribution to momentum transport in a quasilinear model, keeping both γ_E^{neo} and γ_E^{tor} consistently with global temperature and rotation profiles [152]. A cylindrical fluid model has also used a quasilinear calculation of the parallel stress to elucidate the parallel symmetry breaking mechanism leading to momentum transport [158]. Local gyrokinetic simulations with sheared toroidal rotation [133, 157] have indicated a sizeable correction to the momentum diffusivity from the $E\times B$ term, also seen in recent global gyrokinetic PIC simulations [166, 167].

In this chapter, the symmetry breaking caused by $E\times B$ shear is described, and the background perpendicular shear (γ_E) is treated independently from the parallel velocity shear ($u'_{\|}$) to isolate and quantify a nondiffusive, nonpinch contribution to the parallel momentum flux. It is found that the size of the term depends strongly on the magnetic shear, with the sign reversing for negative $\hat{s}$. Perpendicular shear flows are responsible for both symmetry breaking and suppression of turbulence, resulting in a shearing rate at which there is a maximum contribution to the momentum transport. The $E\times B$ momentum transport is shown to be quenched by increasing flow shear more strongly than the standard linear quench rule for turbulent heat diffusivity. We then examine the case of purely toroidal rotation, motivated by experimental observations of $v_\theta \ll v_\varphi$. Most of the results presented in this chapter were previously published in Ref. [56].

5.2 Framework for momentum transport

In a conventional large aspect ratio tokamak, the transport of toroidal angular momentum is dominated by the transport of parallel momentum, since neoclassical mechanisms damp poloidal flows. The parallel contribution to the electrostatic toroidal angular momentum transport Π_φ is given by

$$\Pi_\parallel = 2\pi \left\{ \int \nabla\psi \cdot \tilde{\mathbf{v}}_E R B_t v_\parallel f dv_\parallel d\mu \right\}. \tag{5.1}$$

For explicit listing of the other contributions to the toroidal angular momentum flux which are neglected here, we refer the reader to [72, 170]. In the $s - \alpha$ model used for the simulations of this chapter, $B_t/B = 1$ and $R = R_A$ is constant. In this simplified geometry (only) we may then write $\Pi_\parallel \approx R_A \Gamma_\parallel$ where $\Gamma_\parallel$ is as defined by Eq. (3.85). Given these approximations, for the results in this chapter it is assumed that the transport of parallel momentum is interchangable with the transport of toroidal angular momentum ($\Gamma_\parallel \approx \Pi_\varphi / R_A$).

In addition to s_B and s_j defined by Eq. (2.18), for clarity we also define

$$s_{\hat{s}} = \mathrm{sign}(\hat{s}) = \pm 1, \qquad s_\gamma = \mathrm{sign}(\gamma_E) = -\mathrm{sign}(\nabla E_r \cdot \nabla r) = \pm 1. \tag{5.2}$$

All results presented are for $s_B = s_j = s_\gamma = 1$, but the dependence of the momentum flux on these quantities (verified by simulations) is marked on graph axes. We define q as always positive, since s_j determines the direction of the poloidal field. Positive $\Gamma_\parallel$ is defined as transport of cofield rotation radially outwards.[1]

Motivated by the linear theory of the Coriolis pinch [45] and geometric symmetry breaking [46], we write the parallel momentum flux in the local limit as the sum of four components

$$\Gamma_\parallel = n_i m_i (\chi_\parallel u'_\parallel + V_\varphi u + M_\parallel \gamma_E + C_{\mathrm{FS}}), \tag{5.3}$$

where n_i is ion number density and m_i the ion mass. The terms in this equation correspond to items 1-4 respectively in the list in the previous section: The first term is the diffusive term due to the gradient in the parallel flow, the second term is the Coriolis pinch dependent on the frame rotation [45], the third term is due to the background $E \times B$ shear [151], and the final term is due to the up-down flux surface

---

[1] In later versions of GKW, the definition of $\Gamma_\parallel$ has been altered such that positive momentum is in the direction of φ.

asymmetry [46]. We stress that in this thesis $M_\parallel$ represents the $E\times B$ contribution to parallel momentum transport, not the Mach number.

In linear models (e.g. Ref. [45] and Ref. [46]), it is assumed that the fluctuation amplitudes in temperature, density, and potential scale together, such that the dimensionless ratios V_φ/χ_i, $\chi_\parallel/\chi_i$, and C_{FS}/χ_i vary only slowly over parameter space. Furthermore, the symmetry breaking mechanisms represented by the coefficients $\chi_\parallel$, V_φ, $M_\parallel$, C_{FS} of Eq. (5.3) are assumed to be independent both from each other and from the drivers $u'_\parallel$, u, and γ_E. A linearisation of the symmetry breaking terms [117] has shown that this is a formally valid decomposition for a single linear mode when

$$u'_\parallel \ll R/L_t, \qquad u \ll 0.5, \qquad \gamma_E \ll \gamma_{\max}. \tag{5.4}$$

The decomposition of Eq. (5.3) may also be valid in the nonlinear regime when the cross-phase dependence of the fluctuations do not significantly affect the fluxes [34]. This has proved to be the case in the nonlinear regime for $\chi_\parallel$ and V_φ when $\gamma_E = 0$ (e.g. Refs. [117, 157]), which motivates the use of the decomposition of Eq. (5.3) in this chapter as a framework in which to examine the $E\times B$ contribution to momentum transport.[2] For $\gamma_E \ll \gamma_{\max}$, nonlinear results from GKW with $u'_\parallel = u = 0$ (Fig. 4.8b) indicate $\Gamma_\parallel \propto \gamma_E$, which add further motivation for the use of this framework. (We note however, that precise determination of the form at low $E\times B$ shear is difficult due to the large variance in $\Gamma_\parallel/\gamma_E$.)

The results in this chapter make clear, however, that the linear models which motivate this decomposition Eq. (5.3) do not easily extend to the nonlinear regime when $\gamma_E \sim \gamma_{\max}$: The suppression due to $E\times B$ shearing alters both the spectrum and the amplitude of the turbulence in a manner which makes the various contributions to the momentum transport depend nonlinearly on more than one input drive.

5.3 Asymmetry of nonradial modes

The ballooning representation introduced in Sec. 3.4.1 illustrates that magnetic shear couples the radial wavenumber of a mode to the poloidal angle

$$k_{\theta,n} = -\frac{nq}{r}, \qquad k_{\psi,n}(\theta) = \hat{s}\theta k_{\theta,n} + k_{\psi_0,n}, \tag{5.5}$$

where $k_{\psi_0,n} = \hat{s}\theta_0 nq/r$ is the radial wavenumber at $\theta = \theta_0$ (a repetition of Eq. (3.67)). The poloidal dependence of the radial wavenumber enters the equations in two ways (which can be understood intuitively by reference to the simple model of Sec. 1.5.1):

---

[2] The cross-phase dependence of the fluctuations was calculated for the slab in the quasilinear weights of Ref. [151].

Firstly, the perpendicular wavenumber $k_\perp^2 = k_\theta^2 + k_\psi^2$ appears in the gyroaverage operator which contains the finite Larmor radius (FLR) effects. The FLR effects are more stabilising for larger $k_\perp$, with the consequence that for $\hat{s} \neq 0$, the most unstable mode in the local limit has $k_{\psi_0} = 0$ and $\theta_0 = 0$, with maximum amplitude at the low field side.

Secondly, the radial wavenumber enters in the compression due to the curvature drifts $\mathbf{v}_d$ which drive the mode. In the simple '$s - \alpha$' geometry the compression may be written as

$$\mathbf{v}_d \cdot \nabla = ik_\theta \left[\cos\theta + \left(\hat{s}\theta + \frac{k_{\psi_0}}{k_\theta} \right) \sin\theta \right], \tag{5.6}$$

which in the GKW equations is represented by $\mathcal{D}$ (Eq. (3.27) and Eq. (3.36)) in II of Eq. (3.71). For the most unstable mode with $k_{\psi_0} = 0$, the drive is symmetric in θ. Whilst the drive can be bimaximal, the combination with the FLR stabilisation and parallel coupling usually mean there is only a single mode maximum at the low field side. Furthermore, the presence of $\hat{s}$ in Eq. (5.6) is the reason that the most unstable modes are for geometries with $\hat{s} \sim 1$ (Fig. 4.13), when FLR stabilisation alone would imply the most unstable mode should have $\hat{s} = 0$).

For other modes with $k_{\psi_0} \neq 0$, the maximum drive is shifted from the low field side, and competition with the FLR stabilisation will determine the exact location of the maximal mode amplitude. Note that the asymmetry in the drive will be the largest for modes with small $\hat{s}$, small k_θ and large k_{ψ_0}. However, when the first term in Eq. (5.6) dominates, the growth rate of a mode with $\theta_0 \neq 0$ can be approximated by $\gamma \sim \gamma_0 \cos(\theta_0)$ where γ_0 is the growth rate at $\theta_0 = 0$ [102, 106].

To summarise, two dependencies on the radial wavenumber in the equations both lead to a shift in the eigenmode maximum away from the low field side for modes with $k_{\psi_0} \neq 0$. For geometries with strong magnetic shear, poloidal asymmetry in the FLR stabilisation dominates, whilst for geometries with weak magnetic shear, the asymmetries in the drive from the curvature drifts are more important.

5.4 Symmetry breaking by $E\times B$ shear

As described in Sec. 4.4, the $E\times B$ shear introduces a time dependence into the mode radial wavenumber such that Eq. (5.5) may be written as

$$k_\psi(\theta, t) = k_\theta[\hat{s}(\theta - \theta_0) + \gamma_E t]. \tag{5.7}$$

This means that stationary eikonal eigenfunctions do not exist in the presence of $E\times B$ shear, since as described in the previous section, k_ψ is coupled to a shift in the mode maximum θ_0. A basis mode can then be thought of as an 'eigenmode'

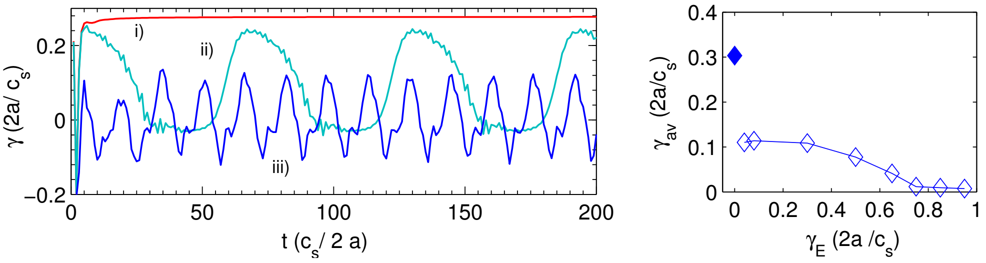

(a) i) $\gamma_E = 0$, i) $\gamma_E = 0.1(2a/c_s)$, iii) $\gamma_E = 0.4(2a/c_s)$

(b) Time averaged growth rates

Figure 5.1: Floquet mode growth rate in GKW for the most unstable mode of the adiabatic GA-STD case, $k_\theta \rho_s = 0.31$.

with a time-dependent $\theta_0' = \theta_0 + (\gamma_E/\hat{s})t$, which is continuously convected along the field line. The convected eigenmode will be convected with an oscillating growth rate $\gamma \sim \gamma_0 \cos(\theta_0')$, since it is driven and damped as it passes through the regions of bad and good curvature respectively [102, 114, 181]. These 'Floquet' modes (or passing modes, or 'Bloch' modes) can be observed in a linear GKW simulation of a single k_ζ mode with a large number of k_ψ modes, and a large i_k (Fig. 5.1a). The cycling of the Floquet mode means that even the smallest amount of $E \times B$ shear will drastically reduce the time averaged growth rate (Fig. 5.1b).[3] At larger γ_E , the shear also distorts the eigenfunctions leading to poloidal breakup of the mode and complete suppression of the linear mode [114].

Clearly the Floquet mode picture breaks down for small values of $|\hat{s}|$, but gives a qualitative understanding of the physics for stronger magnetic shear. To treat $E{\times}B$ shear for values of $\hat{s}$ close to zero in the ballooning representation requires consideration of higher ballooning mode harmonics (for more details see Ref. [114]). In the spectral representation of GKW, these higher ballooning harmonics are kept implicitly in the box of modes.

In the nonlinear regime, the convective cycling of Floquet modes allows nonlinear pumping of linearly stable modes [114], which provides one mechanism for the self-sustained turbulence discussed in Sec. 4.6. When multiple modes (or physically, a continuum) are considered, linearly unstable modes at all k_ψ and k_ζ are continuously growing, convecting and nonlinearly coupling to other modes.[4] The net effect is that a balance is reached, in which the $E \times B$ shear combined with the nonlinear coupling generates a steady average nonzero k_{ψ_0} over all the modes (although there is no single eigenmode for which k_{ψ_0} is constant).

As described in the previous section, a nonzero k_{ψ_0} generates an asymmetry

---

[3] In a global model, the same effect is not observed, because the global solution is a linear combination of modes and an individual Floquet mode cannot be isolated [105, 106, 182, 183].

[4] Since the Floquet mode convection is a consequence of toroidal geometry, $E \times B$ turbulence quenching is qualitatively different in slab geometry.

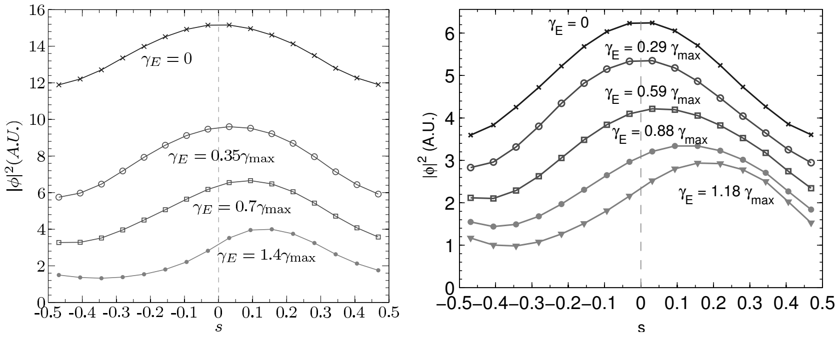

(a) $\hat{s} = 1$ (b) $\hat{s} = 0$

Figure 5.2: GKW nonlinear results for time averaged perturbed parallel potential showing increasing asymmetry with increasing γ_E . For negative γ_E the direction of the shift is reversed for both sets of results. $s \sim \theta/2\pi$ is the parallel coordinate. When $|\hat{s}| > 0.17$, the shift is always in the direction of $s_{\hat{s}} s_B s_j s_\gamma \mathbf{b}$.

in both the local drive and the FLR stabilisation. The result is that the turbulence maximum is shifted away from the low field side, which can be seen in nonlinear simulations (Fig. 5.2a). The direction of the shift depends on the sign of both $\hat{s}$ and γ_E, but for zero $|\hat{s}|$, a shift is still present (Fig. 5.2b).

For nonzero $\hat{s}$, the parallel shift can be understood as the $E{\times}B$ shear acting to undo the twist along a field line due to the magnetic shear (e.g. Fig. 2 of Ref. [100]), so that the maximum drive and minimum FLR stabilisation no longer occur at the low field side. In what follows, this is referred to as the ‘untwisting mechanism’.

At zero magnetic shear, there is no direct coupling between θ_0 and k_{ψ_0} in Eq. (5.7), yet a steady shift in the turbulence maximum persists (Fig. 5.2b), since the average nonzero k_{ψ_0} still breaks the symmetry of the drive from the curvature drifts. In what follows, this is referred to as the ‘curvature drive asymmetry’.

Note that since the rate of increase in k_ψ depends on k_θ, this average k_{ψ_0} will be different for each binormal mode. The $\hat{s} = 0$ case does not require the ballooning representation and can be treated with a formalism purely periodic in θ, and it would be of interest in future work to develop this argument with a simple analytic model. Away from zero $\hat{s}$, the untwisting mechanism dominates, indicated by the reversal of the shift for $\hat{s} < 0$. With this in mind, the use of $s_{\hat{s}} = \pm 1$ should only be interpreted if $|\hat{s}| > 0.2$.

The presence of background $E \times B$ shear has thus been demonstrated to break the symmetry in nonlinear simulation of gyrokinetic turbulence, a necessary but not sufficient condition for the generation of a turbulent momentum flux. In the following sections, the contribution of this symmetry breaking mechanism to the momentum transport is quantified in a large number of nonlinear simulations.

Except where specified otherwise, the simulations are all for the GA-STD case and resolutions described in Sec. 4.6, with adiabatic electrons. A scan over the magnetic shear is presented, since as discussed, this parameter interacts strongly with the $E \times B$ symmetry breaking mechanism. The linear properties, growth rate spectra and turbulent $E{\times}B$ shear suppression for these cases were presented in Sec. 4.7. The '$s - \alpha$' equilibrium model used has up-down symmetric flux surfaces, so the term C_{FS} is zero in all simulations. In addition, all simulations in this chapter have $u = 0$, so the pinch V_ϕ is also zero. All results presented here are obtained with the restart method for larger γ_E, and all time averages were taken over a minimum range of $t_{av} = 1600(a/c_s)$ after the new saturated state was reached, except where specified otherwise. The results presented for $\hat{s} = 1$ correspond to the same simulations presented in Fig. 4.6.

5.5 Momentum transport by $E{\times}B$ shear

In order to investigate the $E{\times}B$ momentum transport term independently from the diffusive and pinch terms, nonlinear gyrokinetic simulations were performed with $u'_\parallel = u = 0$ with a scan over γ_E and $\hat{s}$. Thus for the simulations in this section all terms in Eq. (5.3) are zero except for the $M_\parallel \gamma_E$ term due to $E \times B$ shear. These simulations produce nonzero values for the parallel momentum flux $\Gamma_\parallel$, therefore the system is not in the null flow state of equilibrium rotation.

Since the results presented form a two dimensional parameter scan, we list only selected representative results in tabular form; Table 4.2 shows the variation of fluxes with γ_E for $\hat{s} = 1$, and Table 4.3 shows the variation of the fluxes against $\hat{s}$ for $\gamma_E = 0.141(c_s/a)$. The results for the raw momentum flux are shown in Fig. 5.3(a). As expected, the $E{\times}B$ contribution exhibits a maximum in the shearing rate, but it can also be seen that the results exhibit a strong dependence on the magnetic shear, with the sign reversing with $s_{\hat{s}}$. To deconstruct the results further, we examine ratio quantities of interest.

Since the turbulence follows a linear quench rule (Eq. (4.42)), the quantity $\Gamma_\parallel/\chi_i$ plotted in Fig. 5.3(b) represents the strength of the symmetry breaking $E{\times}B$ contribution with the background level of the turbulence factored out. The results show that the cases with $0 < \hat{s} < 0.5$ behave differently to the outlying values of the magnetic shear, since the ratio $\Gamma_\parallel/\chi_i$ grows with γ_E. This different behaviour suggests that for these cases, both symmetry breaking mechanisms may be at work together.

Fig. 5.3(c) plots the dimensionless quantity $M_R = M_\parallel/\chi_i$; the momentum transport due to $E{\times}B$ shear with the assumed dependence on both the level of the

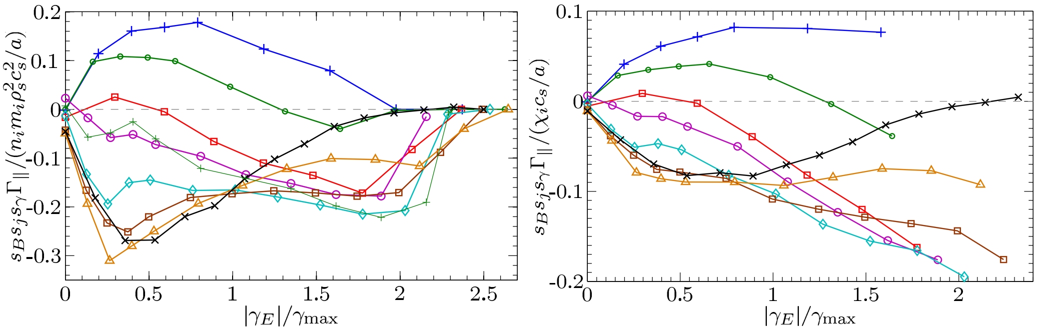

(a) Total momentum flux $\Gamma_\parallel = M_\parallel \gamma_E$.

(b) Normalised with heat diffusivity, $\Gamma_\parallel/\chi_i$.

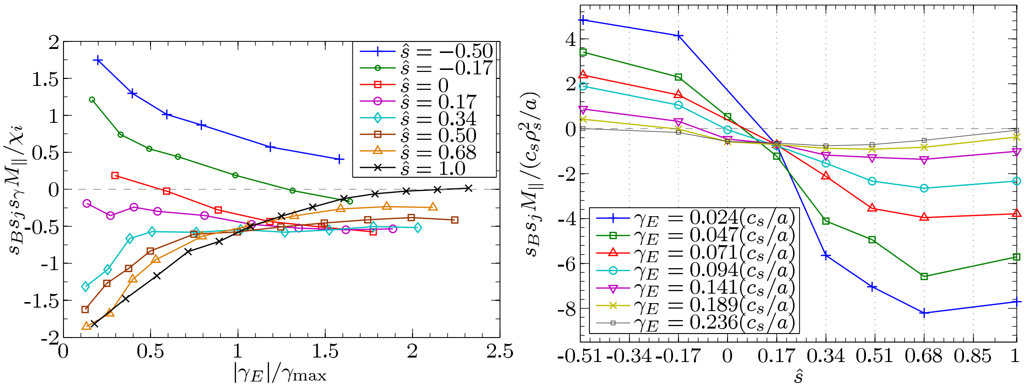

(c) Dimensionless ratio $M_\parallel/\chi_i$.

(d) Orthogonal view of $M_\parallel$.

Figure 5.3: Momentum transport due to $E\times B$ shear, showing the contribution for a number of different values of magnetic shear. The reversal of the sign of the flux with negative γ_E is exact, for all values of $\hat{s}$. The same legend is used for Figs. a), b) and c), and matches 4.13 and 4.14(a). The value of $\gamma_{\max}$ is the maximum linear growth rate at $\gamma_E = 0$ and is a constant for each curve; the values are given in Table 4.1.

turbulence and the rate of the shearing factored out. For $0 < \hat{s} < 0.5$, the value of $M_\parallel/\chi_i$ saturates at around -1 beyond $\gamma_E/\gamma_{\max} \approx 1$, but for larger $|\hat{s}|$ the value goes to zero. The conclusion drawn from Fig. 5.3(c) is that even after factoring out the quenching of turbulence, the dependence of the momentum transport on γ_E is weaker than linear, i.e the $E\times B$ suppression acts more effectively on the $E\times B$ momentum flux than on the heat flux. This clearly demonstrates the limitation of the heuristic linear model (Eq. (5.3)) in this regime.

The existence of a nonzero momentum flux for the $\hat{s} = 0$ case also demonstrates that the curvature drive asymmetry can also generate a flux, which is generally smaller at low γ_E, but comparable at larger γ_E where the untwisting mechanism appears to be less effective. Slicing orthogonally through the $(\hat{s}, \gamma_E)$ parameter space, we see that $M_\parallel$ is not exactly symmetric about $\hat{s} = 0$ (Fig. 5.3(d)), i.e. that the curvature drive asymmetry is present at all values of $\hat{s}$, although in most cases is

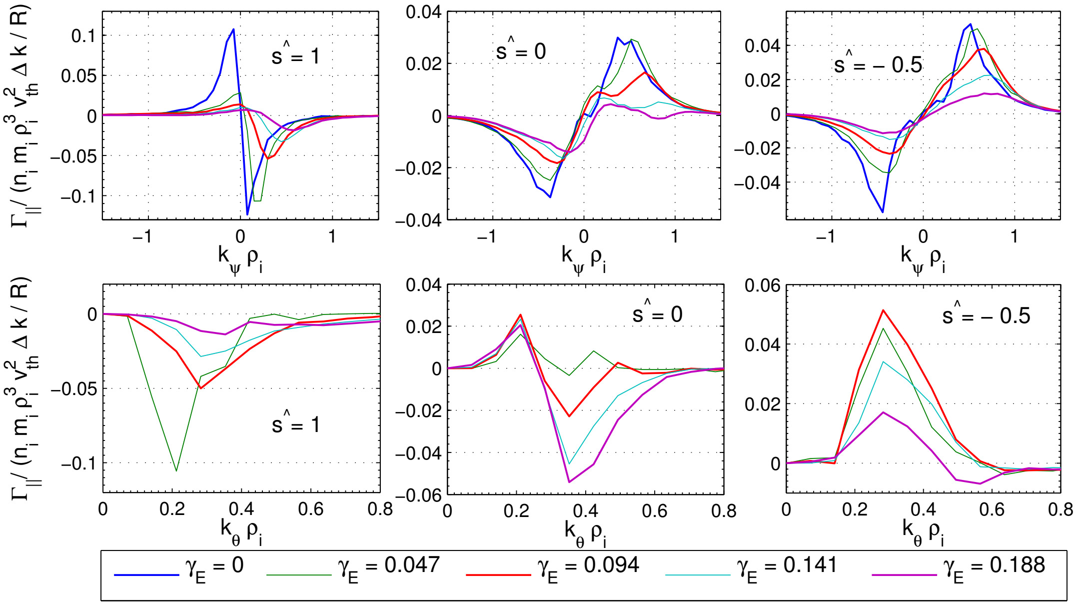

Figure 5.4: Radial and binormal spectra of $\Gamma_\parallel$ for the cases $\hat{s} = -0.5,\ 0,\ 1$. The shearing rate γ_E is in units of c_s/a. The legend is the same for each figure and the quantity plotted is the parallel velocity flux per mode.

dominated by the untwisting mechanism. The result is that $\hat{s} = 0.17$ is a stationary point where $M_\parallel$ is constant over a range of γ_E .

These trends can be better understood by examining the spectra of the parallel velocity flux for different values of $\hat{s}$ (Fig. 5.4). The symmetry in the k_ψ spectrum is clear for $\gamma_E = 0$. For $\hat{s} = \gamma_E = 0$, the sign of the flux has the natural dependence on $\mathbf{v}_E \cdot \nabla\psi \sim (\mathbf{b} \times \mathbf{k}) \cdot \nabla\psi$ that can be expected from the definition of the flux. For $\hat{s} = 1$, the ballooning coupling Eq. (5.7), results in an inversion of the k_ψ spectrum, which is also narrower due to ballooning localisation of the turbulence around $k_\psi = 0$.

For the results with $\gamma_E > 0$, different consequences of the symmetry breaking can be seen for each $\hat{s}$: For $\hat{s} = 1$, the localisation about $k_\psi = 0$ and the untwisting mechanism results in a strong shift towards $k_\psi > 0$ with almost complete removal of flux at $k_\psi < 0$. For $\hat{s} = -0.5$, the symmetry breaking appears as a slightly stronger suppression of the negative flux at $k_\psi < 0$. In the binormal spectrum, the contrasting trends in $M_\parallel/\chi_i$ are illuminated: For $\hat{s} = 1$, the greatest flux occurs at $k_\theta \rho_i \sim 0.2$ whilst the peak occurs at smaller scales $k_\theta \rho_i \sim 0.3$ for the lower shear cases. For all three cases, the peak in χ_i spectrum is at $k_\theta \rho_i \sim 0.25$, and since the largest scales are suppressed first by the $E{\times}B$ shear (Fig. 4.10) this can partly explain the unexpected central result of $M_\parallel/\chi_i \to 0$ as γ_E increases for the $\hat{s} = 1$ case. The k_ψ spectrum also illustrates that linearisation of the $E{\times}B$ symmetry breaking as a small perturbation is invalid even for fairly small γ_E.

For the $\hat{s} = 0$ case, the momentum flux changes sign as γ_E increases, which can be seen to be a result of opposing contributions at different k_θ scales. This can be explained by reference to Eq. (5.6) which shows that shift in the location of the maximum drive depends on k_θ. This could be numerically demonstrated by examining the asymmetric shift in the turbulence maximum for individual k_θ modes, which should be in a different direction at different scales. As the $E \times B$ shear quenches the largest scales, the total momentum flux becomes negative. These spectral results therefore demonstrate why the linearised decomposition of Eq. (5.3) does not hold in the nonlinear regime with $E \times B$ shearing.

The sign of the $E \times B$ contribution to the momentum flux reverses with each of s_B, s_j and s_γ. We emphasise that the definition of $u_\parallel$ is positive in the direction of $\mathbf{B}$, and that positive $\Gamma_\parallel$ is transport of cofield rotation radially outwards. In the laboratory frame, then, flipping the toroidal field does not alter the direction of the rotation resulting from the $E \times B$ contribution to momentum transport. If ∇E_r is radially outwards and $\hat{s} > 0.2$ the effect of the $E \times B$ momentum flux is to spin up the core counter to the plasma current. We note however, that flipping the sign of the plasma current will flip the sign of ∇E_r from toroidal rotation.

5.6 Interaction with diffusive transport

The terms in the heuristic breakdown of turbulent momentum transport (Eq. (5.3)) all depend on the background level of turbulence described by the quench rule (Eq. (4.42)). This most basic dependence can be removed by normalising each term with the ion heat diffusivity χ_i to give dimensionless ratios. However, even with this normalisation, the $E \times B$ driven term $M_\parallel/\chi_i$ is not constant, due to varying competition between shear quenching and symmetry breaking at different scales (as demonstrated in the previous section).

Parallel velocity shear $u'_\parallel$, in contrast, drives both turbulence (antiquench) and diffusive transport. In the linearised decomposition (Eq. (5.3)), it is implicitly assumed that the diffusive term $\chi_\parallel$ is independent of γ_E and u, and that $M_\parallel$ is independent of $u'_\parallel$ and u. In this section, we examine these assumptions with additional adiabatic simulations: A scan is performed over $(u'_\parallel, \gamma_E)$ parameter space (with $u = 0$) by holding a nonzero value of γ_E constant for a range of $u'_\parallel$ (this is distinct from the case of purely toroidal rotation which is discussed in Sec. 5.7). The resulting momentum fluxes therefore contain both the diffusive and $E \times B$ contributions to the momentum transport, from which the assumed dimensionless 'constants' can be calculated. The simulations in this section have $N_{\text{mod}} = 21$ and $k_\theta \rho_s$ up to 1.00.

If independence of the terms is assumed, the normalised diffusive term (pure

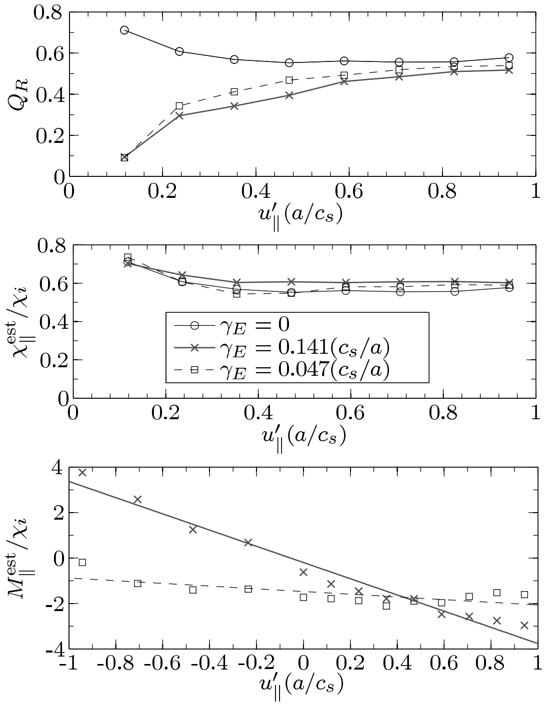

Figure 5.5: Dimensionless ratio Q_R (upper) converges to the value of estimated pure Prandtl number $P_R^{\text{est}} = 0.6$ (middle) as the diffusive term dominates the $E\times B$ term. The curve for $\gamma_E = 0$ (circles) is the same in the top 2 figures. The strength of the $E\times B$ term M_R (lower) is only independent of $u'_\parallel$ for small values of γ_E. The legend is the same for all 3 figures. The linear fits used in the bottom figure are $M_R = (-0.60, -3.57)u'_\parallel(a/c_s) - (1.47, 0.20)$ (dashed, solid).

Prandtl number) can be estimated from

$$P_R(u'_\parallel, \gamma_E) = \frac{\chi_\parallel^{\text{est}}}{\chi_i} = \frac{\Gamma_\parallel(u'_\parallel, \gamma_E) - \Gamma_\parallel(0, \gamma_E)}{u'_\parallel \chi_i(u'_\parallel, \gamma_E) n_i m_i}. \tag{5.8}$$

The values of P_R calculated using this formula are plotted in Fig. 5.5 (middle), and indicate that the pure Prandtl number is roughly constant over a range of both $u'_\parallel$ and γ_E . We also define the dimensionless number

$$Q_R = \frac{\Gamma_\parallel/u'_\parallel}{\chi_i} = \chi_\parallel^{\text{eff}}/\chi_i, \tag{5.9}$$

which is distinct from the pure Prandtl number P_R since the momentum transport in this case is not purely diffusive. We stress that our terminology here differs from most other literature; often Q_R is interpreted as the Prandtl number when the diffusive part and $E\times B$ part are combined (see next section). This can lead to confusion when comparing different quantities between works.

The normalised contribution of the $E\times B$ term alone (also dimensionless) can be estimated from

$$M_R(u'_\parallel, \gamma_E) = \frac{M_\parallel^{\text{est}}}{\chi_i} = \frac{\Gamma_\parallel(u'_\parallel, \gamma_E) - \Gamma_\parallel(u'_\parallel, 0)}{\gamma_E \chi_i(u'_\parallel, \gamma_E) n_i m_i}, \tag{5.10}$$

the calculated values for which are plotted in Fig. 5.5 (lower). The figure shows that for $\gamma_E \ll \gamma_{\max}$ the $E\times B$ contribution is independent of $u'_\parallel$, but this is not the case for larger $\gamma_E \sim \gamma_{\max}$, where the inclusion of parallel flow shear amplifies the $E\times B$ contribution to the momentum transport. For negative $u'_\parallel$, the sign of $M_\parallel$ is even found to invert. In the previous section it was demonstrated that the $E\times B$ contribution was quenched by γ_E more strongly than the heat flux quench rule; here we see the converse: The turbulence is driven by the destabilising parallel flow shear, and the $E\times B$ contribution is amplified. These two results both demonstrate that the $E\times B$ contribution has a stronger than linear dependence on the background level of turbulence, which is not captured by the heuristic breakdown.

The value of Q_R is plotted in Fig. 5.5 (upper). Despite the amplification of $M_\parallel$ with increasing $u'_\parallel$, the value of Q_R converges towards the pure Prandtl number $P_R \approx 0.6$ irrespective of γ_E (< 7% difference) (Fig. 5.5 (upper)), since the diffusive term still dominates the slower variation of $M_\parallel$ with $u'_\parallel$.

In Ref. [157], parallel and perpendicular flow shear were varied independently (i.e. not pure toroidal rotation) to identify null flow points ($\Gamma_\parallel = 0$). Keeping only the rotational terms (diffusive, $E\times B$ and Coriolis) of Eq. (5.3) without toroidal rotation coupling of $u'_\parallel$ and γ_E , locating null flow points requires expensive scans over $(u_\parallel, u'_\parallel, \gamma_E)$ parameter space. Using the assumption of independence of the terms in Eq. (5.3), valid for $\gamma_E \ll \gamma_{\max}$, we estimate the location of null flow points when $u = 0$. Using the value $P_R = 0.6$ for the Prandtl number determined above, and the results for $M_\parallel/\chi_i$ shown in Fig. 5.3(c), we estimate that for the $\hat{s} = 1$ case there is one example of a null flow point at $(u'_\parallel, \gamma_E) \approx (0.1, 0.04)(c_s/a)$, but none for $u'_\parallel > 0.14(c_s/a)$. In Ref. [157], slightly different null flow points were found for $u'_\parallel = 0.1, 0.2$ but not for $u'_\parallel = 0.3$ or greater, but there has since been a correction to these results [184]. For the case with $\hat{s} = 0.5$ we again find the pure Prandtl number $P_R \approx 0.6$ and a similar null flow point at $(u'_\parallel, \gamma_E) \approx (0.1, 0.05)(c_s/a)$.

Since the curve of $\Gamma_\parallel/\chi_i$ (Fig. 5.3(b)) for $\hat{s} = 0.5$ does not turn over, there may also exist null flow points at greater values of γ_E, which could be responsible for transport bifurcations. These null flow points cannot be estimated accurately using the linear assumptions since (as discussed above) $M_\parallel$ is enhanced for $\gamma_E \sim \gamma_{\max}$ with $u'_\parallel > 0$. Locating transport bifurcations accurately therefore requires detailed scans over parameter space (as in Ref. [138]).

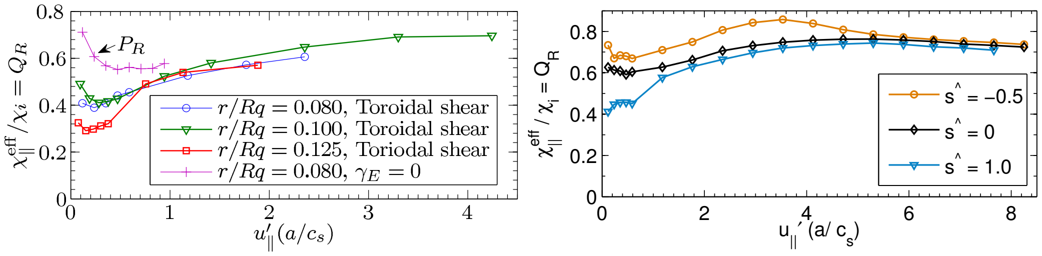

(a) Variation of toroidal coupling with $\epsilon = r/R_A$.

(b) Toroidal shear, variation with $\hat{s}$.

Figure 5.6: Effective Prandtl number $Q_R = \chi_\parallel^{\mathrm{eff}}/\chi_i$ for cases with purely toroidal rotation and safety factor $q = 2$. In a), the aspect ratio r/R_A is varied between $1/6, 1/5$, and $1/4$. In b), the magnetic shear is varied and $r/R_A = 0.16 \neq 1/6$.

5.7 Coupling for pure toroidal rotation

To examine the case of purely toroidal rotation, further simulations are presented including both the parallel shear and the perpendicular shear coupled for purely toroidal rotation (in the previous section, each was varied independently). As discussed in Sec. 4.5, in this case, the parallel and perpendicular flows are coupled such that the poloidal components cancel, which can be written as

$$u'_\parallel = s_B s_j (R_A|q|/r)\gamma_E, \tag{5.11}$$

in the $s - \alpha$ geometry model with $u_\parallel = 0$. In this thesis, the definition of $u_\parallel$ is positive in the direction of $\mathbf{B}$, with the result that a peaked toroidal flow profile has $s_\gamma s_B s_j = 1$.

Whilst $E \times B$ shear quenches transport, parallel velocity shear is destabilising. With the coupling of the parallel velocity shear drive, the turbulence can be sustained in the limit of large γ_E (Fig. 4.6), though this result is sensitive to specific parameters such as the coupling $R|q|/r$ and the temperature gradient [134, 138, 185]. Using the toroidal coupling Eq. (5.11), an effective momentum diffusivity can be defined including the $E \times B$ momentum transport as a correction

$$\chi_\parallel^{\mathrm{eff}} = \chi_\parallel + s_B s_j \frac{r}{R_A|q|} M_\parallel. \tag{5.12}$$

For the case of purely toroidal rotation only, our definition of $Q_R = \chi_\parallel^{\mathrm{eff}}/\chi_i$ can then be thought of as an effective Prandtl number. Again we note that much of the literature uses different terminology here; in most works the distinction between pure and effective Prandtl number is not made, and our 'effective momentum diffusivity' and 'effective Prandtl number' are often interpreted as simply momentum diffusivity and Prandtl number. Furthermore, 'effective momentum diffusivity' is often used in other work to include the Coriolis pinch with the diffusive term (e.g, Refs. [150, 186]).

For $\hat{s} > 0.17$, the $E \times B$ shear contribution to momentum transport has $\mathrm{sign}(\mathrm{M}_\parallel) = -\mathrm{s_B s_j}$, and thus always acts to reduce the effective diffusivity irrespective of the direction of plasma current and toroidal field, suggesting a more peaked rotation profile when this effect is included. Equivalently, the $E \times B$ contribution for $\hat{s} > 0.17$ always transports clockwise momentum in the direction of ∇E_r, which is determined by the direction of any existing peaked rotation profile. Since the size of the correction is partly determined by geometry parameters, the aspect ratio $\epsilon = r/R_A$ was varied and scans were conducted over $u'_\parallel$. The safety factor $q = 2$ was held constant. For the values of ϵ used (and for the other specific parameters of the GA-STD case), the correction to the diffusivity can be up to 50% (Fig. 5.6(a)). It is possible that for other cases (e.g. lower q or larger ϵ) the correction could dominate, resulting in null flow or a negative effective diffusivity. The convergence of Q_R as $u'_\parallel$ increases in Fig. 5.6(a) occurs slower than in Fig. 5.5 (upper), because in the toroidal shear case γ_E increases in tandem with $u'_\parallel$, increasing the $E \times B$ correction to the momentum transport.

For negative magnetic shear, the reversal of $M_\parallel$ results in an increased effective Prandtl number relative to the positive $\hat{s}$ cases (Fig. 5.6(b)). The effect is not as strong as might be expected from Fig. 5.3(c), because for the negative shear case the parallel drive is less effective in countering the turbulence suppression for $\gamma_E < 2\gamma_{\max}$ (i.e the minimum in Fig. 4.6a is more pronounced for $\hat{s} < 0$).

5.8 Kinetic electrons

We next examine the effect of kinetic electrons on the $E \times B$ driven momentum transport. In Fig. 5.7 (top) the momentum fluxes for $(u'_\parallel, \hat{s}) = (0, 1)$ are shown to be comparable with the adiabatic case once the increased turbulence due to the trapped electron drive is factored out. Comparing the parallel potential structure Fig. 5.7 (bottom), we see an similar asymmetric shift for the kinetic and adiabatic cases. This differs from the Coriolis pinch [45] in which the Coriolis drift generates an asymmetry in the parallel velocity structure, and the potential shift in response compensates (completely in the case of adiabatic electrons) the symmetry breaking of the Coriolis drift [155]. Here, no such 'compensation effect' occurs since the asymmetry in the solution is generated directly through the convection and effective shift of the ballooning angle.

Finally, we also investigated the $E \times B$ momentum transport in pure trapped electron mode turbulence in nonlinear simulations with $(u'_\parallel, \hat{s}) = (0, 1)$. This case,

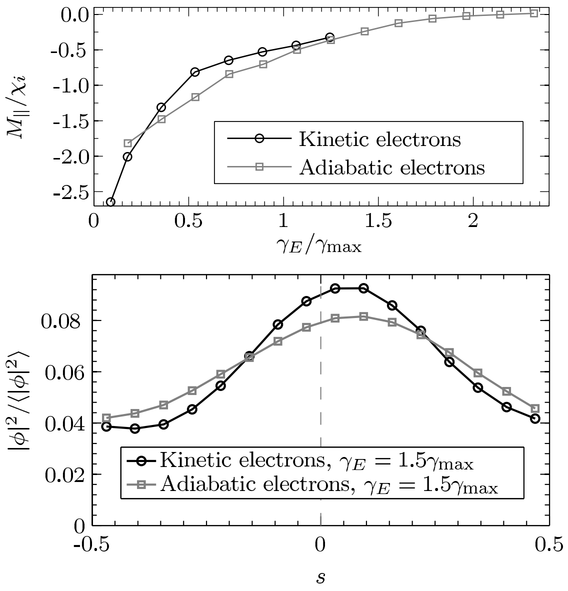

Figure 5.7: (Top) Comparison of M_R for the GA-STD case with kinetic electrons and adiabatic electrons. (Bottom) Parallel perturbed potential structures compared: The trapped electron drive is localised on the outboard side, but the asymmetric shift is equivalent.

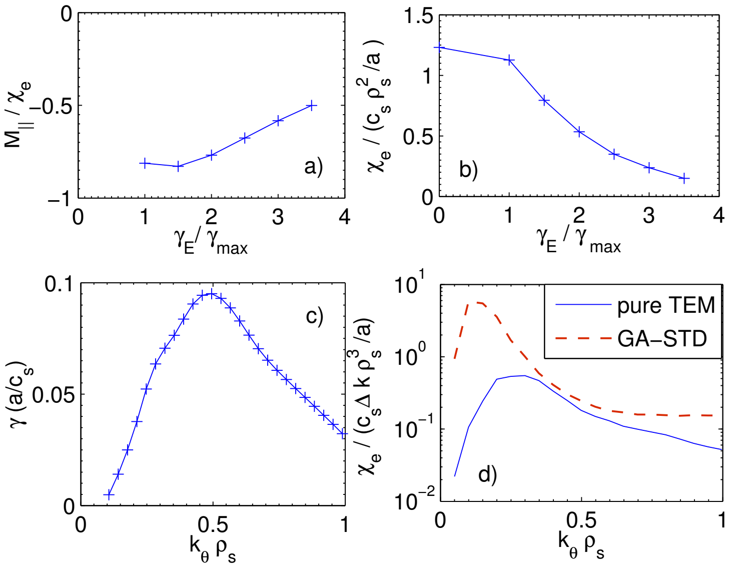

Figure 5.8: Trapped electron mode turbulence, PURE-TEM case: a) $E\times B$ induced momentum momentum transport dimensionless ratio, b) $E\times B$ suppression of electron heat flux, c) growth rate spectrum, d) nonlinear electron heat flux spectrum compared to GA-STD kinetic case.

which we label PURE-TEM has the same geometry parameters as the GA-STD case, but the electron temperature gradient is reduced to $R/L_{T_e} = 7$, the ion temperature gradient reduced to $R/L_{T_i} = 0$ and the ion temperature reduced to $T_i/T_e = 3/10$ to eliminate the smallest scale electron modes [34] and ensure a peaked growth rate spectrum (Fig. 5.8c). The modes all propagate in the electron diamagnetic direction, but the sign of the $E{\times}B$ driven momentum flux is unchanged (Fig. 5.8a), indicating no dependence on the mode propagation direction (a possibility suggested in Ref. [160]). For this case, the thermal transport is dominated by the electrons $\chi_e \gg \chi_i$, and normalising $M_\parallel$ with χ_E gives a dimensionless number of magnitude comparable to M_R for the GA-STD case (which is dominated by ion thermal transport with both kinetic and adiabatic electrons). The shift in the turbulence maximum is in the same direction as in Fig. 5.2a, and the sign and form of the $\Gamma_\parallel$ spectrum in k_ψ is the same as the $\hat{s} = 1$ case in Fig. 5.4. Investigation of the symmetry breaking in the drive for TEM turbulence is more difficult since we find no stable result for this TEM case for $\hat{s} = 0$.

The $E{\times}B$ suppression of turbulence still occurs for the pure TEM case, but at a higher normalised shearing rate $\gamma_E/\gamma_{\max}$. This is explained by the shift in the turbulence spectrum to smaller scales (Fig. 5.8d), since the $E{\times}B$ shear acts first to quench transport at the largest scales, as discussed above.

5.9 Summary

The nonlinear local gyrokinetic simulations presented in this chapter have confirmed and quantified the quasilinear slab prediction of parallel momentum transport due to background $E{\times}B$ shear [151]. The sheared $E{\times}B$ flow both quenches turbulence and drives a parallel asymmetry that produces anomalous parallel momentum transport. Given these competing effects, the turbulent momentum transport due to this term in isolation exhibits an extrema in the shearing rate γ_E (as predicted in Ref. [151]).

The simulations show that the $E{\times}B$ contribution to the momentum transport ($M_\parallel \gamma_E$) has a stronger quenching with γ_E than that observed for the heat diffusivity. The magnitude of the effect relative to the overall turbulence level is quantified by the dimensionless number $M_R = M_\parallel/\chi_i$, which is found to be a strong function of γ_E. This quantity is analogous to the turbulent Prandtl number (the ratio of momentum diffusivity $\chi_\parallel$ to thermal diffusivity χ_i), but unlike the Prandtl number shows significant sensitivity to plasma parameters.

The results presented in this chapter show that the $E{\times}B$ driven momentum flux interacts with the diffusive transport such that M_R also depends on $u'_\parallel$. It is likely that M_R will also vary with toroidal flow u, but this is left for later work.

The symmetry breaking mechanisms responsible for momentum transport therefore cannot be considered independent in the turbulent regime with background $E \times B$ shearing, which sets limits on the applicability of linearised decompositions with independent terms (Eq. (5.3)). When all the mechanisms are included together, nonlinear simulations are required for each point in parameter space to accurately quantify momentum transport, even in the local model.

The direction of the $E \times B$ induced momentum transport reverses with the sign of ∇E_r and $\hat{s}$, such that for positive magnetic shear, the tendency is to transport momentum inwards, enhancing any existing rotation gradient (for both ITG and TEM turbulence). The sign of the flux reverses for negative magnetic shear, and we also find that a weaker symmetry breaking mechanism generates momentum transport at zero magnetic shear. This mechanism will transport toroidal momentum towards a minimum in the q-profile when there is an existing peaked rotation profile. This local 'spin up' could play a role in the formation of some internal transport barriers, especially if (as indicated in Ref. [145]) the poloidal flows in the region of a transport barrier are elevated well above the neoclassical level.

For low parallel flow gradients, the size of the $E \times B$ contribution can be a significant correction to the diffusive momentum transport, under certain conditions resulting in null flow sustaining equilibrium rotation gradients. In the case of purely toroidal rotation, the effective momentum diffusivity can be significantly reduced at lower toroidal rotation gradients. Simulations of ITG turbulence with kinetic electrons have comparable M_R to those with adiabatic electrons, with no parallel mode structure compensation effect (as seen for the Coriolis pinch [155]) observed. Whilst the Coriolis pinch [45] requires a seed rotation, for the $E \times B$ driven momentum transport effect an initial gradient in the rotation must be present.

In summary, whilst the diffusive parallel momentum Prandtl number is roughly constant over a range of parameter space, the results of this chapter show that the equivalent dimensionless ratio for $E \times B$ induced momentum transport is a strong function of shearing rate, parallel flow gradient, and magnetic shear.

Chapter 6

Strong rotation

6.1 Introduction

Tokamak experiments operate with a rotating plasma, with toroidal velocity which may be driven externally but can also arise spontaneously. In a large aspect ratio tokamak, the deuterium Mach number is typically observed to be in the range $0.0-0.3$, and is expected to be low in a future reactor with lower relative momentum input from neutral beams. On this basis, rotational effects were not originally included in the gyrokinetic codes used to model turbulent transport. The observation of spontaneous plasma rotation in the absence of an external momentum source [41, 43] has led to a renewed interest in plasma rotation, and a focus on rotation measurement. Recent observations demonstrate that Mach numbers up to 0.7 can be reached in beam heated conventional aspect ratio devices [186], whilst spherical tokamaks have long been known to operate at Mach numbers approaching unity [187, 188]. Even at low bulk ion rotation, the Mach number for heavy impurities can reach supersonic values, with the result that the distribution and transport of these impurities are strongly influenced by inertial forces. Developing an understanding of impurity transport mechanisms will be of key importance for a successful future fusion reactor, since a buildup of impurities in the core would severely degrade fusion performance.

A number of studies have examined the effect of strong rotation on neoclassical transport [4, 189–194], but the influence of strong rotation on turbulent transport is largely unaddressed. A series of previous works [55, 57, 195] have extended the gyrokinetic formalism to the rotating frame of reference, in which rotational effects appear as inertial forces [57] or modified effective fields [196]. This formulation was used for the gyrokinetic equation derived in Chapter 2, and the implementation in GKW of the complete set of inertial terms was described in Chapter 3.

The Coriolis force is known to play an important role in the anomalous momentum transport that leads to spontaneous rotation [45], and its impact on heat and particle transport has also been studied [156]. The effect of the centrifugal force on particle and heat transport has been examined in a linear fluid model [156], but until now has not been examined using the full gyrokinetic model.

In this chapter, the effects of strong rotation are examined for the first time with a gyrokinetic code, with the inclusion of the centrifugal force in linear and nonlinear gyrokinetic simulations. The effect on the linear stability of the trapped electron mode (TEM) and the ion temperature gradient (ITG) mode is analysed, and consequences for particle and impurity transport are investigated. Nonlinear results for ITG and TEM turbulent transport are presented, and the geodesic acoustic mode (GAM) frequency and the residual zonal flow which affect turbulent saturation are also examined. Most of the results presented in this chapter were previously published in Ref. [89].

6.2 Framework

As discussed in Chapter 2, the centrifugal force must be kept in the local gyrokinetic formalism in the rotating frame when the rotational speed $R\Omega$ of the plasma is of the order of the thermal velocity. With this ordering, the Mach number $u = R\Omega/v_{\mathrm{th,i}}$ of the plasma is of order unity (definitions using c_s differ by a factor of $\sqrt{2}$). The formulation in the rotating frame leads to a number of inertial terms in the gyrokinetic equations, which for convenience we divide into three labelled categories:

1. (TR) All consequences arising from the parallel component of the centrifugal force, as expressed in the centrifugal potential Φ and the centrifugal energy $\mathcal{E}$. This includes the density variation in the Maxwellian (Eq. (2.60)) which also appears as additional terms in the source (Eq. (2.71)), the enhanced mirror force on the perturbed distribution $\mathbf{b} \cdot \nabla\mathcal{E}(\partial f/\partial v_\parallel)$ in Eq. (2.70), the drift $\mathbf{b} \times \nabla\Phi/B$ in Eq. (2.44), and the appearance of $\mathcal{E}$ in the polarisation in the Poisson equation in Eq. (2.82). For brevity we later refer to this group of effects as the 'centrifugal trapping terms'.

2. (CF) The centrifugal drift: $\mathbf{v}_{\mathrm{cf}} = -(m\Omega^2 R/ZeB)\mathbf{b} \times \nabla R$ in Eq. (2.44) arising from the perpendicular component of the centrifugal force.

3. (CO) The Coriolis drift: $\mathbf{v}_{\mathrm{co}} = (2mv_\parallel/ZeB)\boldsymbol{\Omega}_\perp$ in Eq. (2.44). The effect of this term (particularly with regards to momentum transport) has previously been discussed in detail [45, 155, 156, 172] and whilst included in these simulations is not discussed at length in this chapter.

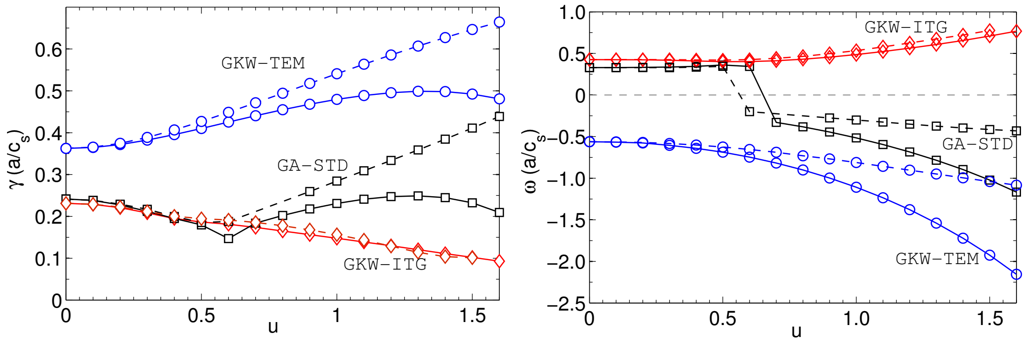

(a) Mode growth rate (b) Mode frequency (comoving frame)

Figure 6.1: Variation in linear properties with rotational Mach number for the GA-STD (squares), GKW-ITG (diamonds), and GKW-TEM $k_\theta \rho_s = 0.707$ (circles) cases, for both $R_0 = R_{\text{axis}}$ (solid) and $R_0 = R_{\text{LFS}}$ (dashed). In b), positive values of ω indicate propagation in the ion diamagnetic direction in the comoving frame. The GA-STD case clearly shows the transition from ITG mode to TEM.

The results presented are again based on the collisionless GA-STD case described in Sec. 4.6, and in addition we also examine two TEM cases (labelled GKW-TEM and PURE-TEM) and a pure ITG mode case (labelled GKW-ITG). The cases all based on the GA-STD case, and differ only in the following:

Case	$k_\theta \rho_s$	R/L_{T_i}	R/L_{T_e}	T_i/T_e
GA-STD	0.304	9.0	9.0	1
GKW-ITG	0.304	9.0	1.0	1
GKW-TEM	0.304 and 0.707	1.0	9.0	1
PURE-TEM	N/A	0.0	7.0	3/10

The wavenumber $k_\theta \rho_s = 0.304$ studied is the most unstable part of the ITG branch for zero rotation, whilst a higher wavenumber $k_\theta = 0.707$ is chosen for some scans of the GKW-TEM case, typical of the wavelengths at which trapped electron modes start to dominate ITG modes at zero rotation. The PURE-TEM case differs from the GKW-TEM case in that finer scale electron temperature gradient (ETG) modes are removed, allowing for a converged nonlinear simulation. All simulations are conducted with the density and its gradient held constant at $R_0 = R_{\text{LFS}}$ when scanning over rotation (see Sec. 2.7.1), with the exception of the indicated curves in Fig. 6.1(a) an Fig. 6.1(b).

Except where stated otherwise, the linear simulations are performed in $s - \alpha$ geometry for a single field line with 5 poloidal turns (equivalent to a single turn with 5 radial wavenumbers), and all calculations are performed with kinetic electrons. For the linear spectrum calculations of Fig. 6.2(a) and Fig. 6.2(b), the results presented are matched as closely as possible to the nonlinear cases presented later. These

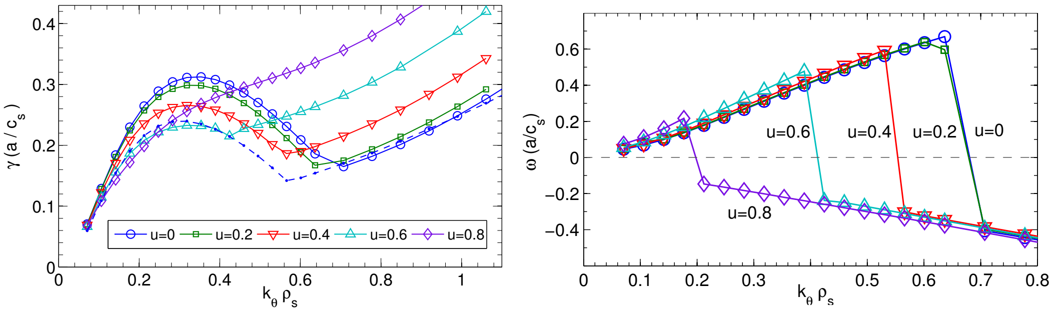

(a) Growth rate spectrum

(b) Dispersion relation

Figure 6.2: Linear properties of the most unstable mode for the kinetic GA-STD case at various bulk ion Mach numbers. The results shown use the circular geometry model with 25 poloidal turns. For comparison, the dashed line in a) is with $s-\alpha$ geometry and $u = 0.0$. In b), The TEM and ITG branches have been left artificially connected to highlight the shift of TEM dominance to longer wavelengths with increasing rotation. Positive values of ω indicate propagation in the ion diamagnetic direction and frequencies are evaluated in the comoving frame.

results therefore use the circular geometry model of Sec. 3.3.2 and Ref. [94] (for reasons made clear later), and a single field line with 25 poloidal turns.

6.3 Linear results

6.3.1 Stability analysis

In this section we examine the effect of the rotation on the linear stability and frequency of the ITG mode and TEM drift waves. First, we examine the growth rate of the modes for the first three cases (Fig. 6.1(a)). As expected, the effect of the inertial terms is small at low Mach numbers. The ITG mode instability is stabilised by higher Mach numbers whilst the TEM is enhanced. The enhancement of the TEM is due to the enhanced mirror force which adds to the trapping condition independently of position in $v_\perp$ space, widening the base of the trapping region. The increased phase space from which the mode can tap energy results in the increased growth rate. This can be clearly seen in the velocity space of the perturbed electron distribution for the GKW-TEM case (Fig. 2.3) which exactly matches the trapping condition of Eq. (2.72). The same destabilisation of the PURE-TEM case is seen in Fig. 6.9(b).

For the more physically realistic equal temperature gradients of the GA-STD case, the suppression of the ITG branch and the enhancement of the TEM branch leads to a transition threshold at around $u = 0.6$ after which the TEM becomes dominant over the ITG mode. At the transition, the direction of mode propagation

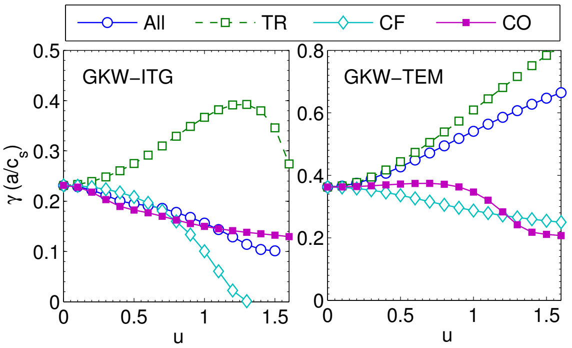

Figure 6.3: Effect of individual inertial terms for the GKW-ITG and GKW-TEM cases on mode growth rate: Centrifugal trapping and potential (TR), centrifugal drift (CF), Coriolis drift (CO).

reverses, as shown in the reversal of the mode frequency (Fig. 6.1(b)). From these results, it is clear that the choice of $R_0 = R_{\mathrm{axis}}$ or $R_0 = R_{\mathrm{LFS}}$ only is insignificant at low Mach numbers and is only of importance for the TEM branch. Previous work has shown that ITG mode stability (Fig 5a of Ref. [29]) is less sensitive to density and density gradient variations than TEM stability [34, 77], although the propagation frequencies of both show some variation with R/L_n.

The ITG mode is the dominant mode at larger wavelengths for zero rotation, but at shorter wavelengths the TEM is dominant. As the rotation increases the enhancement of the TEM alters the balance (Fig. 6.2(a)). The dominant branch at each scale can be easily identified from the dispersion relation (Fig. 6.2(b)). It is clear from Fig. 6.2(b) that the TEM instability becomes dominant at ever larger wavelengths with increasing rotation. Our results show that the transition threshold is sensitive to the geometry model. For converged results for the TEM (and hence the transition), a long field line is resolved and minimal parallel velocity dissipation used.

We next examine the effect of each of the inertial terms independently and in combination, in order to understand the suppression of the ITG branch with increasing Mach number. We divide the inertial terms into three categories as defined in Sec. 6.2. Simulations of the GKW-ITG and GKW-TEM cases were performed with each of the inertial terms artificially included or excluded (Fig. 6.3). For the ITG mode, the results show that the trapping and density redistribution in isolation destabilise the mode for $u < 1$. The Coriolis drift and the Centrifugal drift both have a stabilising influence at very high Mach number, through the modification of the phase shift between the potential and density perturbations occuring at different rates at different poloidal angles. Together, the inertial drifts are sufficient to overcome the destabilising effect of the trapping terms to result in the net ITG mode stabilisation when all rotational terms are kept. For the TEM, the effect of each of the individual terms is qualitatively similar. However, the stabilising influence of the centrifugal drift is outweighed by greater destabilisation in the trapping terms, with the result that the overall effect of all the rotational terms is to destabilise the mode.

For both the ITG mode and TEM, the Coriolis terms introduce an asymmetry in the parallel potential eigenfunction [156], but otherwise the eigenfunction is not strongly modified by the centrifugal terms. Perturbed density eigenfunctions are shown in Fig. 6.6, which for the bulk ions closely follow the potential eigenfunction.

6.3.2 Particle and impurity transport

Heavy impurity ions have higher relative Mach numbers due to their lower thermal velocity, and it is therefore expected that the centrifugal effects will be felt strongly by heavy impurities even at low Mach number u of the bulk ions. To investigate the effect of plasma rotation on particle and impurity transport, linear simulations with a number of trace ion species (which do not affect the properties of the mode solution) are conducted. The trace species do not contribute to the solution of the Poisson Eq. (2.82), with the result that the particle flux of the trace becomes exactly linear in the trace species gradients. The turbulent particle flux for each species can then be divided into four components

$$\Gamma_s = n_s D_s \left(\left.\frac{R}{L_n}\right|_{R_{LFS}} + C_T \frac{R}{L_T} + C_u u' + C_p \right), \tag{6.1}$$

which are the diffusive part, the thermodiffusive part, the rotodiffusive part and the convective part respectively [156, 197, 198]. This decomposition for particle transport has been developed under the assumption that all the gradient quantities in the equation are flux functions, with the fluxes and coefficients taken to be flux surface averages. This assumption is violated for strong rotation, and the redistribution of density over the flux surface leads to ambiguity in the definition of a diffusive term. A choice has been made here to extend Eq. (6.1) to the strongly rotating regime: By using $R/L_n|_{R_{LFS}}$ to define the diffusive term, ‘diffusive’ transport resulting from the centrifugal modification to the density gradient R/L_n^E (Fig. 2.1) is subsumed into the thermodiffusive and convective coefficients (R/L_T and $\partial\mathcal{E}/\partial\psi$ terms in Eq. (2.62) respectively). We note that other choices are possible, but proceed with this as the most natural choice: At fixed u, our choice preserves the exact linear dependence on the driving gradients in the diffusive and thermodiffusive terms. The second consequence of this choice is that as u is varied, D should be only a slowly varying function of the underlying turbulence, (c.f. ‘Pure Prandtl number’ in Chapter 5);

the same does not hold for C_T and C_p. In the results that follow, the trace species used to calculate the coefficients have a large $R/L_n|_{R_{LFS}}$ with $R/L_n|R_{LFS} \approx R/L_n^E$, in order to minimise differences in that might result from alternate definitions of D.

The magnitude of the particle fluxes can only be quantified by nonlinear simulations of the saturated turbulent state. In linear simulations, the fluxes grow exponentially, but variations in the dimensionless ratios C_p, C_T and C_u may be estimated without the nonlinear saturation of the fluxes. Since the cross-phase of the perturbed potential with density or temperature observed in nonlinear simulations shows similarity with that of linear simulations [34, 199], the dimensionless parameters for the bulk species are expected to follow the same trends in linear and nonlinear simulations. For trace species, the linearity of Eq. (6.1) is exact even in the nonlinear regime [200]. For a stationary plasma without any particle source, $\Gamma = 0$, so that in the case of negligible neoclassical transport $-C_T$, $-C_u$ and $-C_p$ give a measure of the steady state density gradient that may be sustained by each component.

The parameters for the bulk ions and electrons are those of the GKW-ITG and GKW-TEM cases, where the wavenumber for the GKW-TEM is modified to $k_\theta \rho_s = 0.304$, the same as for the GKW-ITG case. For the simulations presented in this section, the number of poloidal turns of the field line was increased to 9. The species simulated are Deuterium (D: $Z = 1, M_R = 1$), Helium (He: $Z = 2, M_R = 1.987$), Carbon (C: $Z = 6, M_R = 5.964$), and partially ionised Tungsten (W: $Z = 46, M_R = 91.28$). For each ion, three trace species $T1$, $T2$ and $T3$ are included with equilibrium gradients $(R/L_n|_{R_{LFS}},\ R/L_T,\ u') = \{(10,0,0),\ (0,0,0),\ (0,0,10)\}$, respectively. All species have the same temperature as the bulk ions, and rotate with the same velocity (neoclassical effects are neglected).

The coefficients C_p and C_u are then calculated as

$$C_p = \frac{10\ \Gamma_{T2}}{\Gamma_{T1} - \Gamma_{T2}}, \qquad C_u = \frac{\Gamma_{T3} - \Gamma_{T2}}{\Gamma_{T1} - \Gamma_{T2}}. \tag{6.2}$$

For the GKW-ITG case, the convective impurity pinch $-C_p$ increases with the rotation, more strongly with increasing impurity mass (Fig. 6.4(a)). For the GKW-TEM case, the inertial terms reduce the convective pinch, and there is less dependence on the impurity mass. For the rotodiffusive coefficient C_u, the behaviour for the tungsten impurity is qualitatively different to the other ions, this we attribute to the different charge to mass ratio of the partially ionised impurity (Fig. 6.5(a)). The results show that the rotodiffusive coefficient C_u is small compared to C_p for the GKW-ITG case, whilst in the GKW-TEM case, the magnitude of the effect is comparable to that for the convective part at higher Mach numbers. Inclusion of additional species with $R/L_T > 0$ indicates that the thermodiffusive part C_T (which

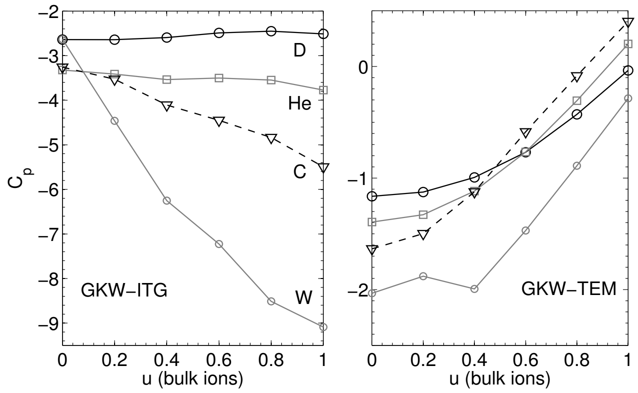

(a) GKW results

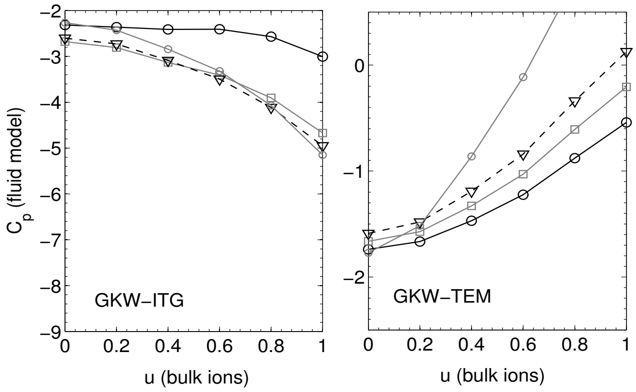

(b) Fluid model

Figure 6.4: Impurity transport coefficient C_p for trace species Deuterium, Helium, Carbon and Tungsten for GKW-ITG and GKW-TEM cases both with $k_\theta \rho_s = 0.304$. Symbols for each species are the same on all plots.

is unimportant for heavy impurities [198] in the absence of rotation) is small and not strongly affected by the rotation at realistic values of R/L_T.

The effect of the inertial terms on these convective coefficients can also be compared with the predictions of the low field side fluid model of Ref. [156]. In this model, there are no poloidal variations, but the effect of the Centrifugal drift is kept and appears as an ‘effective mode frequency’ which accounts for the modified phase relation between density and potential (distinct from the modification of the real mode frequency due to the centrifugal drift in the gyrokinetic simulations). The fluid model is not closed, and predicts trace impurity transport only for a given mode structure.

Using the mode structure ($k_\parallel$, $k_\parallel^2$ and ω) obtained from the gyrokinetic simulations, Eqs. (26) and (27) of Ref. [156] can be evaluated and compared to the full gyrokinetic results which contain the additional effects of centrifugal trapping

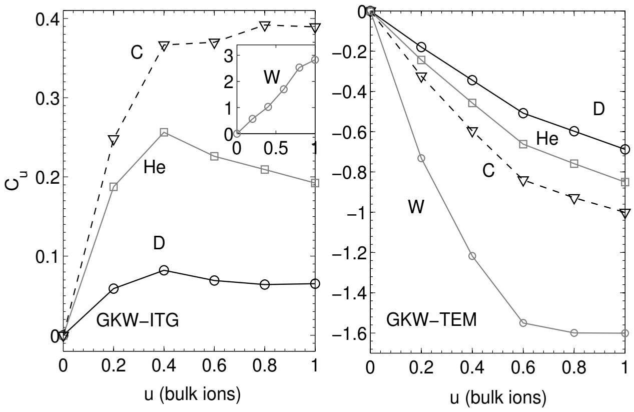

(a) GKW results

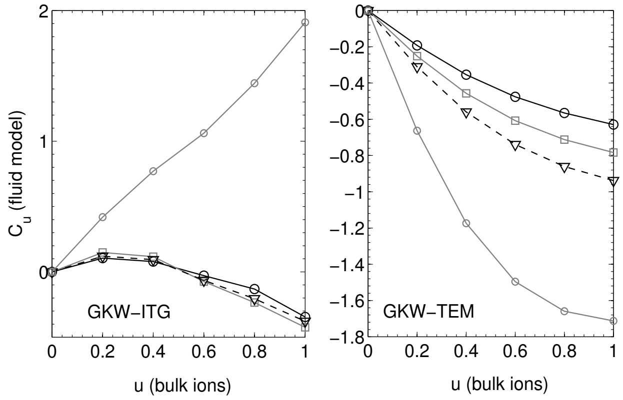

(b) Fluid model

Figure 6.5: Impurity transport coefficient C_u for trace species Deuterium, Helium, Carbon and Tungsten for GKW-ITG and GKW-TEM cases both with $k_\theta \rho_s = 0.304$. Symbols for each species are the same on all plots.

and flux surface density variation. The parallel mode structure of the potential and bulk ions (Fig. 6.6) are largely unaffected by the centrifugal terms, and trace impurities play no role in the potential eigenfunction. Asymmetry arising from the Coriolis drift results in a small $k_\parallel$ in the potential eigenfunction, but its impact on particle transport is small. It was verified that the alteration in mode structure $k_\parallel$ and $k_\parallel^2$ due to the centrifugal force are small enough not to affect the results of the fluid model. The comparison with the gyrokinetic results (Fig. 6.4(b) and Fig. 6.5(b)), therefore reveals any dependence on poloidal variation and centrifugal trapping. The results show that for the TEM the two models give very close agreement, whilst discrepancies of up to 100% are evident for the ITG mode.

For the heavier impurities, the gyrokinetic results find a larger $-C_p$ for the GKW-ITG case due to the effects of poloidal variation not included in the fluid model of Ref. [156]. This is in agreement with a different recent fluid model [201] which

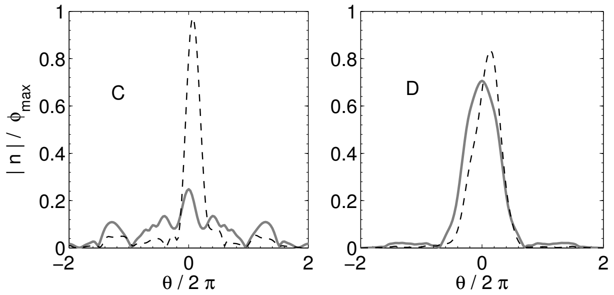

Figure 6.6: Perturbed ion density parallel eigenfunctions for the GA-STD case with $u = 0$ (solid) and $u = 0.6$ (bulk ions) (dashed) for Carbon and Deuterium traces.

has shown that the poloidal variation in the magnetic drift frequencies can cause an inward (outward) flux for ITG (TEM) modes when the greater density is at the low field side. In our decomposition, this effect is incorporated into C_p and increases with the asymmetry (and hence impurity mass). This effect depends subtly on the mode structure and does not appear to be significant for the GKW-TEM case. The centrifugal modification to the trapping and velocity space structure (Fig. 2.3) also play a role in determining the particle transport [156, 198], with the trapped impurity ions contributing an inward flux (outward) flux for the ITG (TEM) case [202]. Future work should isolate each of these effects methodically in the strongly rotating case to quantify the importance of each mechanism.

For C_u, the comparison shows almost exact agreement for the GKW-TEM case, whilst for the GKW-ITG case the trends and magnitudes are in approximate agreement (Fig. 6.5(b)) given the small magnitude.

The results presented in this section should be interpreted with caution: They make preliminary predictions about the variation with rotation of the convective and rotodiffusive particle fluxes as they have been defined in Eq. (6.1), but extrapolation to predictions of zero flux impurity gradients is complicated due to the strong divergence between flux surfaces and surfaces of constant density for heavy impurities in a rotating plasma. Furthermore, these results are for a single linear mode, and in general the contributions to the particle flux can vary with scale. For quantitative determination, a quasilinear [203, 204] or fully nonlinear approach is required. Future progress will require careful thought on how best to extend Eq. (6.1) so that the diffusive coefficient can be defined and determined independently of variations in the density gradients in rotating plasmas. Determination of realistic equilibrium impurity distributions in two dimensions (ψ, θ) could be achieved by searching for zero flux states on multiple flux surfaces, and may need to include both collisions and neoclassical transport in nonlinear simulations.

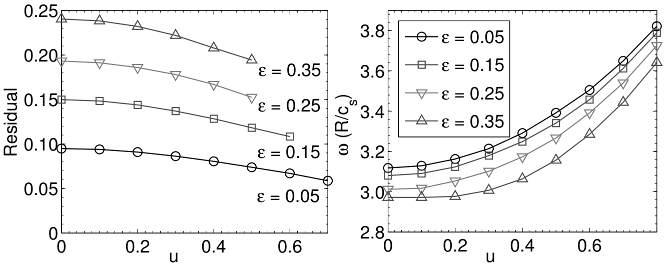

Figure 6.7: Zonal flow residual $\phi(t=\infty)/\phi(t=0)$ and geodesic acoustic mode frequency for $q = 1.1$.

6.3.3 Zonal flow response

In the drift wave zonal flow paradigm (introduced in Sec. 1.7), gyrokinetic turbulence is regulated by zonal flows driven through nonlinear interactions [29, 30, 33]. The $E \times B$ shear of these zonal flows acts to break apart the largest scale structures, creating a self regulating feedback which determines the level of transport. Accurate calculation of the zonal flow response is therefore vital for determining the correct turbulence saturation level [31]. At low q, an initial perturbation in a zonal mode is kinetically damped to a nonzero residual zonal flow that is independent of the initial perturbation [27].

The inertial terms are expected to modify the zonal flow response at high rotation since the centrifugal drift modifies mode oscillation frequencies [57]. To investigate this, simulations with adiabatic electrons were used to calculate the zonal flow residual for the electrostatic collisionless case with $q = 1.1$, $k_\psi \rho_s = 0.0525$, for a range of ϵ and u. Rather large grid sizes are used to avoid the recurrence problem [112]. Also for reasons of numerical stability, the circular geometry model of Ref. [94] was used, since we find it addresses some deficiencies of the standard $s-\alpha$ model which contribute to a numerical instability for the zonal modes at higher Mach number.

The results show that the residual zonal flow decreases with increasing rotation (Fig. 6.7), which may indicate that the zonal flows regulating turbulent fluctuations will decrease with strong rotation.[1] Numerical experimentation by switching off the trapping terms and drift terms independently indicates that the reduction in the residual is due to the inertial drifts, whilst the trapping terms increase the residual by a smaller amount. The choice of $R_0 = R_{\text{LFS}}$ or $R_0 = R_{\text{axis}}$ makes no difference to the final result of Fig. 6.7. The frequency of the GAM is found to increase with rotation, due to the influence of the centrifugal drift. This agrees with previous

---

[1] The saturation mechanism in nonlinear gyrokinetic turbulence is an area of active research and its dependence on the zonal flow residual is open to debate

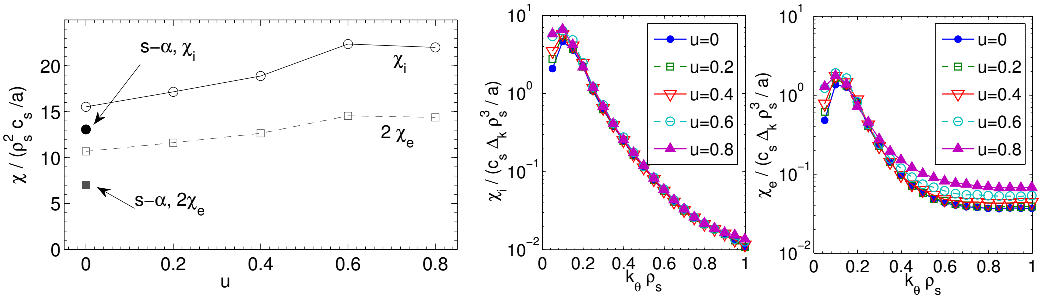

(a) Turbulent thermal diffusivities

(b) Thermal diffusivity spectra

Figure 6.8: Ion and electron heat diffusivities for the GA-STD case. In a), the filled points show the equivalent result in the $s-\alpha$ geometry.

work which calculated the influence of the inertial terms on the GAM frequency [205]; further work to analytically calculate the zonal flow residual in the presence of strong rotation would also be of interest for comparison. An additional GAM branch driven by strong rotation with also identified in Ref. [205], identification of this mode in GKW is left for a later work.

6.4 Nonlinear results

6.4.1 Thermal transport

Nonlinear kinetic simulations are presented for the GA-STD and PURE-TEM cases. In the nonlinear phase, the GA-STD case is an ITG dominated case, with an additional drive from the trapped electrons, a scenario typical for many tokamak operating regimes. The parameters for the PURE-TEM case represent an alternate experimental regime dominated by electron turbulence (for example in plasmas with strong density peaking, $E\times B$ shear or radio frequency wave heating).

The simulations were performed with $N_{\mathrm{mod}} = 21$ binormal modes and $N_x = 167$ radial modes with a perpendicular simulation domain of extent $[L_{\mathrm{radial}}, L_{\mathrm{binormal}}] = [120, 126]\rho_s$. The maximum resolved wavevector has binormal wavenumber $k_\theta\rho_s = 1.0$, The number of grid points in parallel velocity, magnetic moment, and along the field line are $N_{v\parallel} = 48$, $N_\mu = 8$ and $N_s = 21$ respectively. The $v_\parallel$ and s resolutions are slightly higher than those in Sec. 4.6, in order to more accurately resolve the trapped-passing boundary, required for an accurate determination of the particle flux and centrifugal trapping effects. These grid sizes have proved sufficient to resolve the diffusivities presented here, which are averaged for $t_{av} = 550(a/c_s)$ after the saturated state was reached. The circular geometry model [94] was used, to prevent numerical instabilities developing in the zonal mode.

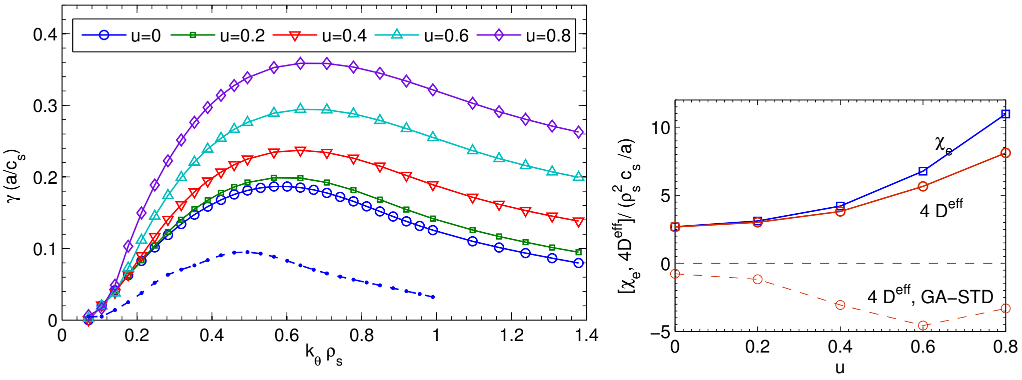

(a) Growth rate spectra

(b) Turbulent diffusivities

Figure 6.9: Results for PURE-TEM case in circular geometry. In a) the dashed line represents the spectrum in $s-\alpha$ geometry. In b), the effective particle diffusivity is calculated as $D_{\text{eff}} = \Gamma/\{R/L_n^E\}$ and the dashed line is the comparable result for the GA-STD case.

The results for the GA-STD case show a moderate increase in ion heat diffusivity with rotation (Fig. 6.8(a)), reaching 40% at $u = 0.6$. We attribute this increase primarily to the increased trapped electron drive, but perhaps also to a decreased stabilising response of the zonal flow. As rotation increases, we find that the magnitude of the perturbation in the zonal modes becomes less relative to the other modes. The increase in heat transport comes from the largest scales modes (Fig. 6.8(b)) which are stabilised most by the zonal flow. The promotion of the trapped electron modes shown in the linear results leads to an increase in electron heat transport at smaller scales (Fig. 6.8(b)), but since these scales contribute little to overall transport, the result is that the electron heat transport shows no more increase than the ion heat transport.

Comparing the linear mode frequencies (Fig. 6.2(b)) directly against the transport spectrum (Fig. 6.8(b)), we note that mode propagation is in the ion direction at the scales which the dominate the transport for all values of rotation simulated. We also investigated a case with reduced $R/L_{T_i} = 7.7$, in which the dominant linear mode was in the electron diamagnetic direction at all scales once $u > 0.5$. Nonlinear results for this case, however, did not show an increase in electron heat transport with increasing rotation, with the ITG turbulence more robust in the nonlinear regime. This is an example of the more general result that transitions between TEM and ITG in nonlinear turbulence occur gradually and are associated with a drop in electron transport [206], and need not occur at the same point in parameter space as the transition to the dominant linear mode. Similarly, in the GA-STD case, the robustness of the ITG is such that even when the smaller scale

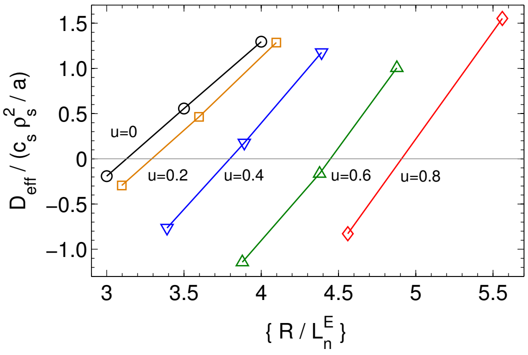

Figure 6.10: Location of zero particle flux state for GA-STD case with effective particle diffusivity calculated as $D_{\text{eff}} = \Gamma/\{R/L_n^E\}$.

electron modes have the largest growth rate at high Mach number, the nonlinear spectrum still peaks at ITG scales and no upturn is visible at smaller scales in the spectrum (Fig. 6.8(b)).

For the PURE-TEM case, the destabilisation of the linear modes by the enhanced centrifugal trapping leads directly to an increase in electron heat transport $\propto u^2$ (Fig. 6.9(b)). The particle flux also increases proportionally with the turbulence level, unlike in the GA-STD case in which an inward particle flux increases more strongly than the gradual increase in turbulence (discussed below).

It is necessary to point out that in practice an increased toroidal rotation will often be associated with an increased toroidal rotation gradient, which is not included in the present simulations. The stabilising effect of the $E\times B$ shear from the perpendicular component competes against the destabilising effect of the parallel velocity shear [44] and is sensitive to geometry parameters q and ϵ. For the GA-STD case, the parallel shear drive prevents turbulence quenching (Sec. 4.6, and Refs. [56, 133]), but for other cases the stabilising effect of $E\times B$ shear can dominate [134] and would counter the increased transport predicted by Fig. 6.8(a).

6.4.2 Particle transport

When investigating the effect of rotation on particle transport, it is particularly important to be mindful of the previously discussed coupling of the rotation and density gradient. In order to examine a quantity with physical meaning that is independent of definitions of the density gradient, we searched for the null particle flux state ($\Gamma = 0$), varying $R/L_n|_{R_{LFS}}$ between 3 and 4. The results in Fig. 6.10 are plotted against the flux surface average $\{R/L_n^E\}$ since it is independent of the R_0 used, and is most relevant in determining the central density linked to fusion performance. The total particle flux is determined by the balance between an inward contribution from low energy trapped electrons, and an outward contribution from higher energy trapped electrons [198]. These results indicate that for the GA-STD case (ITG turbulence dominated), the increased fraction of low energy trapped electrons (Fig. 2.3) due to the centrifugal trapping lead to an increase in the steady state $\{R/L_n^E\}$ with increasing rotation.

Collisions are also known to play a role in determining particle transport by similarly altering the balance between trapped and passing electrons [198]. Preliminary nonlinear simulations with collisions in the GA-STD case show that the increase in the inward particle flux persists at the same magnitude, and the addition of heavier impurities confirm the linear result that the inward convection increases with impurity mass and Mach number. Full nonlinear investigation of particle and impurity transport with collisions we leave for a later work.

6.5 Summary

The gyrokinetic equations formulated in a comoving frame that rotates with the plasma allow for natural inclusion of the centrifugal and Coriolis forces in a local flux tube model (Chapter 2). This chapter presents the first gyrokinetic simulations including the centrifugal force, relevant to the case of a strongly rotating plasma.

The parallel component of the centrifugal force redistributes equilibrium density over the flux surface and causes an enhanced mirror force which enlarges the trapped particle region in velocity space (Fig. 2.3). The enlarged trapping region alters the threshold for the trapped electron mode, promoting it over the ion temperature gradient mode at intermediate scales (Fig. 6.2(b)). The perpendicular component of the centrifugal force results in the centrifugal drift, which modifies the mode frequency, and reduces the residual of the zonal flow response (Fig. 6.7).

Nonlinear simulations of ion temperature gradient (ITG) mode dominated turbulent transport indicate a moderate increase in the ion heat diffusivity with strong rotation (Fig. 6.8(a)) due to the increased trapped electron drive and reduced regulation from the zonal flow. For pure trapped electron mode turbulence, a stronger increase in electron heat diffusivity is found, since the destabilisation due to the enhanced trapping effects occurs at the dominant transport scales. These simulations considered rotation, but did not include the stabilising effect of rotational shear discussed in Chapter 4.

Increased numbers of slow trapped electrons enhance the convective particle pinch [197] in the nonlinear simulations, resulting in an increased steady state density gradient with rotation (Fig. 6.10). These results suggest that strong rotation could impact core particle density, with possible benefits for fusion performance. Linear investigations into trace impurity transport for the ITG mode show a stronger convective pinch for heavy impurities due to their strong centrifugal trapping (Fig. 6.4(a)). For heavy impurities, the redistribution of equilibrium density over the flux surface due to the centrifugal force is extreme, resulting in strong modifications to the diffusive particle flux. Determination of steady state impurity gradients in the presence of rotation will require further investigation, with nonlinear simulations including the effect of collisions needed to quantify the behaviour of turbulent impurity transport in a rotating plasma.

Chapter 7

Conclusions

In the last twenty years of development, gyrokinetic models of turbulent transport in tokamak plasmas have become increasingly sophisticated, with increased computational power allowing many new physical effects to be included. This thesis extends the local gyrokinetic code GKW to the regime of strongly rotating plasmas, through the inclusion of the centrifugal force in the frame that corotates with the plasma. In Chapter 2, the gyrokinetic equations containing all the inertial terms were derived in the local limit, and the implementation of these equations in GKW was described in Chapter 3. In Chapter 6, the consequences of the new centrifugal terms for heat, particle, and impurity transport were examined in linear and nonlinear simulations.

Gradients in plasma rotation can both drive and suppress plasma turbulence, which makes their inclusion in the model an additional necessity if rotating plasmas are to be accurately simulated. In Chapter 4, methods for implementing a sheared background rotation in a local code were investigated, and the implementation and benchmark of the method chosen for GKW was described.

The rotation in a tokamak may be driven externally, as in beam heated plasmas, but is also observed to arise spontaneously in plasmas with no external torque. This observation has motivated much recent theoretical attention on mechanisms which break the symmetry of the gyrokinetic equation and lead to turbulent momentum transport. In addition to suppressing turbulence, sheared background flow is one such mechanism that breaks the symmetry, and the first detailed quantitative gyrokinetic study of the resulting momentum transport is the subject of Chapter 5.

7.1 Results

The nonlinear benchmark of background shear flow in Chapter 4 demonstrated that GKW and GYRO give very similar values, giving good confidence in the quantitative results of both codes. A detailed convergence study with GKW in the region of critical shear (complete turbulence quenching) has illustrated how to obtain meaningful results in this region. Nonlinear simulations of turbulence suppression due to background $E{\times}B$ shear found that the quench rule for ITG turbulence does not depend strongly on magnetic shear, and is expected to be insensitive to other gradual changes in plasma parameters that do not change the nature of turbulence. However, fundamentally different turbulence regimes (for example pure ITG and pure TEM) can have different shear quench rules if the dominant turbulent transport occurs at different scales.

In Chapter 5, the background perpendicular shear was treated independently from the parallel velocity shear to examine a nondiffusive, nonpinch contribution to the parallel momentum flux. It was found that the strength of this symmetry breaking mechanism depends strongly on the magnetic shear, with the sign reversing for negative magnetic shear. Since perpendicular shear flows are responsible for both symmetry breaking and suppression of turbulence, this contribution to the momentum transport exhibits a maximum in the shearing rate. Furthermore, even when the $E\times B$ induced momentum transport is normalised with the background turbulence level, it is found to be quenched by increasing flow shear more strongly than the linear quench rule for turbulent heat diffusivity. The results of Chapter 5 also demonstrate significant cross coupling between symmetry breaking mechanisms in the nonlinear phase with $E\times B$ shear. This suggests that accurate prediction of experimental rotation profiles will require nonlinear simulations incorporating all the effects simultaneously.

The effects of the centrifugal force, examined in Chapter 6, are felt as a centrifugal drift and an enhanced mirror force. The enhanced mirror force redistributes density over a flux surface, and modifies the trapping condition, destabilising trapped electron modes. For pure trapped electron mode (TEM) turbulence, a strong increase in the thermal diffusivity (proportional to the square of the Mach number) is found, since the turbulence drive is increased at all scales. In some cases, the linear eigenmodes can be switched from ITG to TEM by the presence of strong rotation, but examining one such case in the nonlinear state reveals a resilience in the ion transport due to the gradual nature of the transition to the TEM regime.

For nonlinear ion temperature gradient (ITG) mode dominated turbulence, increased trapped electron drive and reduced zonal flow lead to a moderate increase in ion thermal diffusivity if the strong rotation is not accompanied by rotational shear stabilisation. An increased fraction of slow trapped electrons enhances the convective particle pinch, leading to an increase in the steady state density gradient with strong rotation. The steady state density gradient for the case of pure TEM turbulence remains to be examined.

For heavy trace impurities, linear (and preliminary nonlinear) ITG mode results show an increased inward convection due to strong centrifugal impurity trapping. For the TEM mode a reduced inward convection is attributable to the centrifugal drift, since this result closely agrees with a previous fluid model in which the drift was the only centrifugal effect. The TEM investigated has both density and temperature gradient drive, and previous results in the literature indicate that isolating the drive mechanisms could reveal different behaviour for each case.

As is to be expected, new questions arise directly from these results: For momentum transport the next step will be a more detailed examination of the interaction between symmetry breaking mechanisms in nonlinear simulations (in particular, the interaction of the Coriolis pinch with $E\times B$ shear still needs to be examined). The persistence of $E\times B$ symmetry breaking even at zero magnetic shear could be further clarified by an analytic model. The Coriolis pinch arises from an interaction between parallel velocity and density mode structure, and could be modified at strong rotation since both are modified by the centrifugal trapping.

The effects of strong rotation on particle and impurity transport should be systematically investigated in the linear regime so that different mechanisms can be isolated and compared for modes with each of the three primary drives. This investigation is already underway, and is being completed in parallel with comparison to experimental datasets. In the future, predictive modelling capability for impurity transport will require quasilinear or nonlinear studies including strong rotation, collisions, and neoclassical transport.

Another natural follow-up is the study of the strong rotation effects together with $E\times B$ shear, relevant to the situation in a spherical tokamak. Here, the $E\times B$ shear may suppress the ITG modes whilst the strong rotation enhances the trapped electron modes, but this remains to be demonstrated in nonlinear simulations.

7.2 Outlook

Heat and particle transport were the original focus of gyrokinetic simulations, and the study of momentum transport is a relative latecomer to the field. The results in this thesis contribute one piece to the puzzle of momentum transport, and also initiate examination of the consequences of strong rotation on turbulent transport. All the mechanisms which contribute to momentum transport in the local limit have now been identified by the systematic study of the symmetries of the gyrokinetic equation, but quantitative evaluation of these effects and comparison with experiment is only just beginning.

The Coriolis pinch and $E\times B$ shear contributions can together act against diffusive momentum transport to sustain a rotation gradient even in the absence of an external torque. However, these mechanisms cannot explain the origin the initial rotation, and since both depend on the direction of the existing rotation, they cannot determine a preference for rotation in a specific direction. Up-down asymmetry of the flux surface is the only symmetry breaking in the local model which can contribute this seed, and its greatest impact is in the outer core. Given that the former mechanisms can transport momentum inwards to the core, a understanding of momentum buildup in the edge and scrape-off-layer is vital for predicting core rotation. In these regions, models different to that presented in this work are used, and additional atomic physics is needed.

It is likely that some of the seed rotation arises from mechanisms that only appear in global gyrokinetic models. A leading candidate is the effect of profile shearing that gives a poloidal rotation to the most unstable mode, which generates momentum transport analogously to the $E\times B$ effect examined in this thesis [179]. Careful work is required to disentangle and evaluate the contributions to momentum transport in a global model, this should be a prerequisite to building accurate simplified transport models for momentum. These transport models could be built from local results, with an ‘a priori’ input of a seed rotation from a global model. In the long term, global models well calibrated against the local models may be the best tool to calculate the evolution of intrinsic rotation on the transport timescale.

The models of anomalous momentum transport are now sufficiently advanced that there is scope for combining the mechanisms identified so far in experimentally relevant simulations. Diagnostic progress in charge exchange recombination spectroscopy is leading to increasingly accurate determination of rotation profiles [143, 207], and experiments with perturbed momentum injection [150] provide a route to direct measurement of effective momentum diffusivity. With these experimental advances, pieces of the theory are already starting to be validated [145, 147, 149, 174].

The effects of the centrifugal force on underlying turbulence may be more difficult to observe in experiment, since it is difficult to vary rotation as an independent parameter in experiment. Even if the rotation can be controlled cleanly (perhaps by applying braking from increased magnetic ripple), it will be difficult to isolate centrifugal effects from the effects of rotational shear. For ITG turbulence, an increase in density peaking with rotation may be observable. Experiments dominated by TEM turbulence typically have less external momentum input, so in these cases it may be difficult to actively control the rotation to search for a dependence. Impurity measurement is also challenging, and measurements of density distributions in 2D are very limited. However, the effects of the centrifugal force on heavy impurities are large enough that by comparing simulations with and without it for experimental parameters, its effect on density peaking should be evident, and initial investigations are already underway.

Given the reversal of the $E \times B$ driven momentum transport with the magnetic shear, it is natural to consider its role in the formation of transport barriers associated with a minimum in the q-profile. Following the results presented in Chapter 5, extensive parameter scans in local simulations have recently identified possible bifurcations in transport near zero magnetic shear [138]. However, the δf local model used in this thesis is unable to study evolution on transport timescales without an additional layer of transport equations [208, 209]. A fully consistent treatment of barrier formation will require rotation profiles calculated consistently with the turbulent toroidal momentum transport, should include background $E \times B$ shearing from neoclassical poloidal flows consistent with these profiles, and might also require calculation of the turbulent poloidal momentum transport [151, 210].

A general feature of the results in this thesis is that they force us to think carefully about the linearised decompositions of independent mechanisms in particle and momentum transport as the models are extended to include new effects. The paradigm of the transport matrix, whilst useful, has its limitations: It cannot include effects such residual stress due to flux surface shaping, and the definition of independent matrix elements becomes ambiguous for both strong rotation and for momentum transport with $E \times B$ shear. These complications imply that extrapolations from linear dependencies should be done with caution in quantitative comparisons with experiments, with nonlinear simulation of the specific parameter set preferable where possible. After theoretical identification of mechanisms from simplified models has been completed, new physics can still be identified from extensive numerical scans over parameter space. Whilst expensive, these studies can be used to fine tune more efficient quasilinear models, and provide one part of the transition from abstract theory to methodical engineering. This transition is necessary if predictive transport models for future fusion reactors are to be constructed.

Given the Mach numbers expected in a future reactor, it is likely that the important consequences of the centrifugal force will be for impurity transport. Whilst rotation may be desirable for accessing improved confinement regimes, these need to be developed with an understanding of the consequences for impurity buildup in the core. Since there are a number of competing mechanisms for impurity transport, it is possible that configurations may exist that efficiently confine heat whilst rapidly expelling impurities. Finding these scenarios will require an understanding of both barrier formation and the sensitivities of impurity transport in different regimes. The results of this thesis underline that rotation must be considered for both problems.

Bibliography

[1] D. Meade, Nucl. Fusion **50**, 014004 (2010).

[2] *EFDA-JET*, http://www.jet.efda.org/.

[3] V. D. Pustovitov, Plasma Physics Reports **29**, 105 (2003).

[4] F. L. Hinton and S. K. Wong, Phys. Fluids **28**, 3082 (1985).

[5] J. Wesson, Nucl. Fusion **37**, 577 (1997).

[6] W. Horton, Rev. Mod. Phys. **71**, 735 (1999).

[7] W. Dorland, PhD in physics, Princeton University (1993).

[8] J. Weiland, *Collective Modes in Inhomogeneous Plasma* (IOP, 2000), 1st ed.

[9] A. A. Vlasov, Soviet Physics Uspekhi **10**, 721 (1968).

[10] L. Landau, J. Phys. USSR **10** (1946), English translation in JETP 16, 574.

[11] E. A. Frieman and L. Chen, Phys. Fluids **25**, 502 (1982).

[12] J. Weiland, A. Jarmn, and H. Nordman, Nucl. Fusion **29**, 1810 (1989).

[13] P. K. Shukla and J. Weiland, Phys. Rev. A **40**, 341 (1989).

[14] J. Weiland and A. Hirose, Nucl. Fusion **32**, 151 (1992).

[15] W. Dorland and G. W. Hammett, Phys. Fluids B-Plasma **5**, 812 (1993).

[16] G. W. Hammett, M. A. Beer, W. Dorland, et al., Plasma Phys. Contr. F. **35**, 973 (1993).

[17] M. A. Beer, PhD in physics, Princeton University (1995).

[18] M. A. Beer and G. W. Hammett, Phys. Plasmas **3**, 4018 (1996).

[19] D. Strintzi and B. Scott, Phys. Plasmas **11**, 5452 (2004).

[20] B. D. Scott, Phys. Plasmas **12**, 102307 (2005).

[21] M. Kotschenreuther, W. Dorland, M. A. Beer, et al., Phys. Plasmas **2**, 2381 (1995).

[22] R. E. Waltz, G. M. Staebler, W. Dorland, et al., Phys. Plasmas **4**, 2482 (1997).

[23] G. Bateman, A. H. Kritz, J. E. Kinsey, et al., Phys. Plasmas **5**, 1793 (1998).

[24] G. M. Staebler, J. E. Kinsey, and R. E. Waltz, Phys. Plasmas **12**, 102508 (2005).

[25] G. M. Staebler, J. E. Kinsey, and R. E. Waltz, Phys. Plasmas **14**, 055909 (2007).

[26] J. E. Kinsey, G. M. Staebler, and R. E. Waltz, Phys. Plasmas **15**, 055908 (2008).

[27] M. N. Rosenbluth and F. L. Hinton, Phys. Rev. Lett. **80**, 724 (1998).

[28] H. Biglari, P. H. Diamond, and P. W. Terry, Phys. Fluids B-Plasma **2**, 1 (1990).

[29] R. E. Waltz, G. D. Kerbel, and J. Milovich, Phys. Plasmas **1**, 2229 (1994).

[30] Z. Lin, T. S. Hahm, W. W. Lee, et al., Science **281**, 1835 (1998).

[31] A. M. Dimits, G. Bateman, M. A. Beer, et al., Phys. Plasmas **7**, 969 (2000).

[32] K. Itoh, S. Itoh, P. H. Diamond, et al., Phys. Plasmas **13**, 055502 (2006).

[33] P. H. Diamond, S. Itoh, K. Itoh, et al., Plasma Phys. Contr. F. **47**, 35 (2005).

[34] T. Dannert and F. Jenko, Phys. Plasmas **12**, 072309 (2005).

[35] S. C. Cowley, R. M. Kulsrud, and R. Sudan, Phys. Fluids B-Plasma **3**, 2767 (1991).

[36] G. Plunk, Phys. Plasmas **14**, 112308 (2007).

[37] R. C. Wolf, Plasma Phys. Contr. F. **45**, R1 (2003).

[38] J. Connor, T. Fukuda, X. Garbet, et al., Nucl. Fusion **44**, R1 (2004).

[39] P. W. Terry, Rev. Mod. Phys. **72**, 109 (2000).

[40] F. Wagner, G. Becker, K. Behringer, et al., Phys. Rev. Lett. **49**, 1408 (1982).

[41] L.-G. Eriksson, E. Righi, and K.-D. Zastrow, Plasma Phys. Contr. F. **39**, 27 (1997).

[42] J. Rice, M. Greenwald, I. Hutchinson, et al., Nucl. Fusion **38**, 75 (1998).

[43] J. Rice, A. Ince-Cushman, J. deGrassie, et al., Nucl. Fusion **47**, 1618 (2007).

[44] A. G. Peeters and C. Angioni, Phys. Plasmas **12**, 072515 (2005).

[45] A. G. Peeters, C. Angioni, and D. Strintzi, Phys. Rev. Lett. **98**, 265003 (2007).

[46] Y. Camenen, A. G. Peeters, C. Angioni, et al., Phys. Rev. Lett. **102**, 125001 (2009).

[47] J. Wesson, *Tokamaks* (Oxford Science, 2004), 3rd ed.

[48] J. P. Freidberg, *Plasma Physics and Fusion Energy* (Cambridge University Press, 2007).

[49] R. D. Hazeltine and J. D. Meiss, *Plasma Confinement* (Dover, 2003).

[50] K. Miyamoto, *Controlled Fusion and Plasma Physics* (Taylor & Francis, 2007).

[51] M. Shimada, D. Campbell, V. Mukhovatov, et al., Nucl. Fusion **47**, S1 (2007).

[52] A. H. Boozer, Rev. Mod. Phys. **76**, 1071 (2005).

[53] P. J. Catto, W. M. Tang, and D. E. Baldwin, Plasma Physics **23**, 639 (1981).

[54] A. J. Brizard and T. S. Hahm, Reviews of Modern Physics **79**, 421 (2007).

[55] A. J. Brizard, Phys. Plasmas **2**, 459 (1995).

[56] F. J. Casson, A. G. Peeters, Y. Camenen, et al., Phys. Plasmas **16**, 092303 (2009).

[57] A. G. Peeters, D. Strintzi, Y. Camenen, et al., Phys. Plasmas **16**, 042310 (2009).

[58] A. G. Peeters, Y. Camenen, F. J. Casson, et al., Comp. Phys. Commun. **180**, 2650 (2009).

[59] A. G. Peeters, Y. Camenen, F. J. Casson, et al., *GKW How and Why*, http://www.gkw.org.uk/tikiwiki/Manual, GKW manual, expanded from Comp. Phys. Comm, **180**, 2650.

[60] F. L. Hinton and R. D. Hazeltine, Reviews of Modern Physics **48**, 239 (1976).

[61] E. Mazzucato, S. H. Batha, M. Beer, et al., Phys. Rev. Lett. **77**, 3145 (1996).

[62] G. McKee, R. Ashley, R. Durst, et al., Rev. Sci. Instr. **70**, 913 (1999).

[63] G. R. McKee, M. Murakami, J. A. Boedo, et al., Phys. Plasmas **7**, 1870 (2000).

[64] R. Nazikian, K. Shinohara, G. J. Kramer, et al., Phys. Rev. Lett. **94**, 135002 (2005).

[65] G. McKee, C. Petty, R. Waltz, et al., Nucl. Fusion **41**, 1235 (2001).

[66] P. Hennequin, Comptes Rendus Physique **7**, 670 (2006).

[67] S. Hirshman and D. Sigmar, Nucl. Fusion **21**, 1079 (1981).

[68] T. S. Hahm, Phys. Plasmas **3**, 4658 (1996).

[69] R. G. Littlejohn, Phys. Fluids **24**, 1730 (1981).

[70] R. G. Littlejohn, J. Plasma. Phys. **29**, 111 (1983).

[71] H. Sugama, Phys. Plasmas **7**, 466 (2000).

[72] B. Scott and J. Smirnov, Phys. Plasmas **17**, 112302 (2010).

[73] J. B. Taylor, Phys. Fluids **7**, 767 (1964).

[74] T. Vernay, S. Brunner, L. Villard, et al., J. Phys. Conf. Series **260**, 012021 (2010).

[75] T. Vernay, S. Brunner, L. Villard, et al., Phys. Plasmas **17**, 122301 (2010).

[76] R. E. Waltz, G. D. Kerbel, J. Milovich, et al., Phys. Plasmas **2**, 2408 (1995).

[77] A. G. Peeters, C. Angioni, M. Apostoliceanu, et al., Phys. Plasmas **12**, 022505 (2005).

[78] R. E. Waltz and R. L. Miller, Phys. Plasmas **6**, 4265 (1999).

[79] E. J. Synakowski, S. H. Batha, M. A. Beer, et al., Phys. Plasmas **4**, 1736 (1997).

[80] C. Bourdelle, W. Dorland, X. Garbet, et al., Phys. Plasmas **10**, 2881 (2003).

[81] A. J. Brizard, Phys. Plasmas **7**, 4816 (2000).

[82] R. Hatzky, T. M. Tran, A. Konies, et al., Phys. Plasmas **9**, 898 (2002).

[83] L. Villard, P. Angelino, A. Bottino, et al., Plasma Phys. Contr. F. **46**, B51 (2004).

[84] J. C. Kniep, J. G. Leboeuf, and V. K. Decyk, Comp. Phys. Commun. **164**, 98 (2004).

[85] J. Candy, R. E. Waltz, S. E. Parker, et al., Physics of Plasmas **13**, 074501 (2006).

[86] W. W. Lee, Phys. Fluids **26**, 556 (1983).

[87] P. J. Morrison, Phys. Plasmas **12**, 058102 (2005).

[88] A. G. Peeters, D. Strintzi, Y. Camenen, et al., Phys. Plasmas **16**, 042310 (2009).

[89] F. J. Casson, A. G. Peeters, C. Angioni, et al., Phys. Plasmas **17**, 102305 (2010).

[90] S. Hamada, Nucl. Fusion **2**, 23 (1962).

[91] B. Scott, Phys. Plasmas **5**, 2334 (1998).

[92] B. Scott, Phys. Plasmas **8**, 447 (2001).

[93] J. W. Connor, R. J. Hastie, and J. B. Taylor, Phys. Rev. Lett. **40**, 396 (1978).

[94] X. Lapillonne, S. Brunner, T. Dannert, et al., Phys. Plasmas **16**, 032308 (2009).

[95] H. Lütjens, A. Bondeson, and O. Sauter, Comp. Phys. Commun. **97**, 219 (1996).

[96] B. McMillan, X. Lapillonne, S. Brunner, et al., Phys. Rev. Lett. **105**, 155001 (2010).

[97] A. Burckel, O. Sauter, C. Angioni, et al., J. Phys. Conf. Series **260**, 012006 (2010).

[98] M. A. Beer, S. C. Cowley, and G. W. Hammett, Phys. Plasmas **2**, 2687 (1995).

[99] N. Crouseilles, M. Mehrenberger, and H. Sellama, Commun. Comp. Phys. **8**, 484 (2010).

[100] J. T. M. Antonsen, J. F. Drake, P. N. Guzdar, et al., Phys. Plasmas **3**, 2221 (1996).

[101] R. L. Dewar and A. H. Glasser, Phys. Fluids **26**, 3038 (1983).

[102] J. W. Connor, J. B. Taylor, and H. R. Wilson, Phys. Rev. Lett. **70**, 1803 (1993).

[103] J. Y. Kim and M. Wakatani, Phys. Rev. Lett. **73**, 2200 (1994).

[104] F. Jenko, Comp. Phys. Commun. **125**, 196 (2000).

[105] J. Y. Kim, Y. Kishimoto, M. Wakatani, et al., Phys. Plasmas **3**, 3689 (1996).

[106] Y. Kishimoto, J.-Y. Kim, W. Horton, et al., Plasma Phys. Contr. F. **41**, A663 (1999).

[107] A. Bottino, PhD in physics, Universita degli Studi di Torino, EPFL, Lausanne (2004).

[108] A. A. Schekochihin, S. C. Cowley, W. Dorland, et al., Plasma Phys. Contr. F. **50**, 124024 (2008).

[109] T. Tatsuno, W. Dorland, A. A. Schekochihin, et al., Phys. Rev. Lett. **103**, 015003 (2009).

[110] M. Frigo and S. Johnson, Proc. IEEE **93**, 216 (2005).

[111] W. Dorland, F. Jenko, M. Kotschenreuther, et al., Phys. Rev. Lett. **85**, 5579 (2000).

[112] J. Candy and R. Waltz, Journal of Computational Physics **186**, 545 (2003).

[113] P. G. Drazin and W. H. Reid, *Hydrodynamic stability* (Cambridge University Press, 2004).

[114] R. E. Waltz, R. L. Dewar, and X. Garbet, Physics of Plamas **5**, 1784 (1998).

[115] P. J. Catto, Phys. Fluids **16**, 1719 (1973).

[116] J. Rice, A. Ince-Cushman, J. deGrassie, et al., Nucl. Fusion **47**, 1618 (2007).

[117] A. Peeters, C. Angioni, A. Bortolon, et al., Nucl. Fusion **51** (2011), Overview of toriodal momentum transport (submitted).

[118] R. L. Miller and R. E. Waltz, Phys. Plasmas **1**, 2835 (1994).

[119] F. Baron, PhD in physics, Univ. Pierre et Marie Curie, Paris, France (1982).

[120] U. Schumann, in *Lecture Notes in Physics, Berlin Springer Verlag* (1985), vol. 218, 492–496.

[121] T. Gerz, U. Schumann, and S. E. Elghobashi, Journal of Fluid Mechanics Digital Archive **200**, 563 (1989).

[122] T. Görler, PhD in physics, Universität Ulm (2009).

[123] R. S. Rogallo, NASA STI/Recon Technical Report N **81**, 31508 (1981).

[124] T. A. Zang, Applied Numerical Mathematics **7**, 27 (1991).

[125] A. Pumir, Phys. Fluids **8**, 3112 (1996).

[126] J. Schumacher and B. Eckhardt, EPL (Europhysics Letters) **52**, 627 (2000).

[127] K. A. Brucker, J. C. Isaza, T. Vaithianathan, et al., J. Comp. Phys. **225**, 20 (2007).

[128] G. W. Hammett, W. Dorland, N. F. Loureiro, et al., in *48th Annual Meeting of the Division of Plasma Physics, Philadelphia, (APS)* (2006), VP1.136.

[129] T. S. Hahm and K. H. Burrell, Phys. Plasmas **2**, 1648 (1995).

[130] K. H. Burrell, Phys. Plasmas **4**, 1499 (1997).

[131] W. M. Nevins, A. M. Dimits, B. I. Cohen, et al., in *Proceedings of the Eighteenth IAEA Fusion Energy Conference, Sorrento* (2000), THP1/03.

[132] R. E. Waltz, J. M. Candy, and M. N. Rosenbluth, Phys. Plasmas **9**, 1938 (2002).

[133] J. E. Kinsey, R. E. Waltz, and J. Candy, Phys. Plasmas **12**, 062302 (2005).

[134] C. M. Roach, I. G. Abel, R. J. Akers, et al., Plasma Phys. Contr. F. **51**, 124020 (2009).

[135] B. D. Scott, Physical Review Letters **65**, 3289 (1990).

[136] B. D. Scott, Physics of Fluids B: Plasma Physics **4**, 2468 (1992).

[137] B. D. Scott, Phys. Plasmas **12**, 062314 (2005).

[138] E. G. Highcock, M. Barnes, A. A. Schekochihin, et al., Phys. Rev. Lett. **105**, 215003 (2010).

[139] J. Candy and R. E. Waltz, Phys. Plasmas **13**, 032310 (2006).

[140] F. Merz and F. Jenko, Phys. Rev. Lett. **100**, 035005 (2008).

[141] I. H. Hutchinson, J. E. Rice, R. S. Granetz, et al., Phys. Rev. Lett. **84**, 3330 (2000).

[142] J. Rice, W. Lee, E. Marmar, et al., Nucl. Fusion **44**, 379 (2004).

[143] A. Bortolon, B. P. Duval, A. Pochelon, et al., Phys. Rev. Lett. **97**, 235003 (2006).

[144] J. S. deGrassie, J. E. Rice, K. H. Burrell, et al., Phys. Plasmas **14**, 056115 (2007).

[145] T. Tala, Y. Andrew, K. Crombe, et al., Nucl. Fusion **47**, 1012 (2007).

[146] W. M. Solomon, K. H. Burrell, J. S. deGrassie, et al., Plasma Phys. Contr. F. **49**, B313 (2007).

[147] T. Tala, K.-D. Zastrow, J. Ferreira, et al., Phys. Rev. Lett. **102**, 075001 (2009).

[148] S. Kaye, W. Solomon, R. Bell, et al., Nucl. Fusion **49**, 045010 (2009).

[149] G. Tardini, J. Ferreira, P. Mantica, et al., Nucl. Fusion **49**, 085010 (2009).

[150] P. Mantica, T. Tala, J. S. Ferreira, et al., Phys. Plasmas **17**, 092505 (2010).

[151] R. R. Dominguez and G. M. Staebler, Phys. Fluids B-Plasma **5**, 3876 (1993).

[152] X. Garbet, Y. Sarazin, P. Ghendrih, et al., Phys. Plasmas **9**, 3893 (2002).

[153] A. G. Peeters and D. Strintzi, Phys. Plasmas **11**, 3748 (2004).

[154] A. G. Peeters, C. Angioni, A. Bottino, et al., Plasma Phys. Contr. F. **48**, B413 (2006).

[155] A. G. Peeters, C. Angioni, Y. Camenen, et al., Phys. Plasmas **16**, 062311 (2009).

[156] Y. Camenen, A. G. Peeters, C. Angioni, et al., Phys. Plasmas **16**, 012503 (2009).

[157] R. E. Waltz, G. M. Staebler, J. Candy, et al., Phys. Plasmas **14**, 122507 (2007).

[158] O. D. Gürcan, P. H. Diamond, T. S. Hahm, et al., Phys. Plasmas **14**, 042306 (2007).

[159] O. D. Gürcan, P. H. Diamond, and T. S. Hahm, Phys. Rev. Lett. **100**, 135001 (2008).

[160] P. H. Diamond, C. J. McDevitt, O. D. Gürcan, et al., Phys. Plasmas **15**, 012303 (2008).

[161] D. Strintzi, A. G. Peeters, and J. Weiland, Phys. Plasmas **15**, 044502 (2008).

[162] J. Weiland, R. Singh, H. Nordman, et al., Nucl. Fusion **49**, 065033 (2009).

[163] Y. Camenen, A. G. Peeters, C. Angioni, et al., Phys. Plasmas **16**, 062501 (2009).

[164] T. S. Hahm, P. H. Diamond, O. D. Gürcan, et al., Phys. Plasmas **15**, 055902 (2008).

[165] A. G. Peeters, C. Angioni, and D. Strintzi, Phys. Plasmas **16**, 034703 (2009).

[166] I. Holod and Z. Lin, Phys. Plasmas **15**, 092302 (2008).

[167] W. X. Wang, T. S. Hahm, S. Ethier, et al., Phys. Rev. Lett. **102**, 035005 (2009).

[168] F. I. Parra and P. J. Catto, Phys. Plasmas **17**, 056106 (2010).

[169] F. I. Parra, M. Barnes, and P. J. Catto, preprint arXiv:1102.4613 (2011), (submitted to Nuc. Fusion).

[170] F. I. Parra, M. Barnes, and A. G. Peeters, preprint arXiv:1102.3717 (2011), (submitted to Nuc. Fusion).

[171] N. Mattor and P. H. Diamond, Phys. Fluids **31**, 1180 (1988).

[172] N. Kluy, C. Angioni, Y. Camenen, et al., Phys. Plasmas **16**, 122302 (2009).

[173] M. A. Mahmood, A. Eriksson, and J. Weiland, Phys. Plasmas **17**, 122310 (2010).

[174] Y. Camenen, A. Bortolon, B. P. Duval, et al., Phys. Rev. Lett. **105**, 135003 (2010).

[175] Y. Camenen, A. Bortolon, B. P. Duval, et al., Plasma Phys. Contr. F. **52**, 124037 (2010).

[176] C. J. McDevitt, P. H. Diamond, O. D. Gürcan, et al., Phys. Plasmas **16**, 052302 (2009).

[177] C. J. McDevitt, P. H. Diamond, O. D. Gürcan, et al., Phys. Rev. Lett. **103**, 205003 (2009).

[178] O. D. Gürcan, P. H. Diamond, P. Hennequin, et al., Phys. Plasmas **17**, 112309 (2010).

[179] Y. Camenen, Y. idomura, S. Jolliet, et al., Nucl. Fusion **51** (2011), Momentum transport by ion-scale turbulence in global and local gyrokinetic simulations (submitted).

[180] F. I. Parra and P. J. Catto, Plasma Phys. Contr. F. **52**, 045004 (2010).

[181] F. L. Waelbroeck and L. Chen, Phys. Fluids B-Plasma **3**, 601 (1991).

[182] J. B. Taylor and H. R. Wilson, Plasma Phys. Contr. F. **38**, 1999 (1996).

[183] J. W. Connor and T. J. Martin, Plasma Phys. Contr. F. **49**, 1497 (2007).

[184] R. E. Waltz, G. M. Staebler, J. Candy, et al., Phys. Plasmas **16**, 079902 (2009).

[185] M. Barnes, F. I. Parra, E. G. Highcock, et al., Phys. Rev. Lett. **106**, 175004 (2011).

[186] P. de Vries, M. Hua, D. McDonald, et al., Nucl. Fusion **48**, 065006 (2008).

[187] R. J. Akers, J. W. Ahn, G. Y. Antar, et al., Plasma Phys. Contr. F. **45**, A175 (2003).

[188] S. Kaye, W. Solomon, R. Bell, et al., Nucl. Fusion **49**, 045010 (2009).

[189] S. K. Wong, Phys. Fluids **30**, 818 (1987).

[190] P. J. Catto, I. B. Bernstein, and M. Tessarotto, Phys. Fluids **30**, 2784 (1987).

[191] H. Sugama and W. Horton, Phys. Plasmas **4**, 2215 (1997).

[192] R. D. Hazeltine and F. L. Hinton, Phys. Plasmas **12**, 102506 (2005).

[193] K. G. McClements and R. J. McKay, Plasma Phys. Contr. F. **51**, 115009 (2009).

[194] E. A. Belli and J. Candy, Plasma Phys. Contr. F. **51**, 075018 (2009).

[195] M. Artun and W. M. Tang, Phys. Plasmas **1**, 2682 (1994).

[196] A. Thyagaraja and K. G. McClements, Phys. Plasmas **16**, 092506 (2009).

[197] C. Angioni and A. G. Peeters, Phys. Rev. Lett. **96**, 095003 (2006).

[198] C. Angioni, J. Candy, E. Fable, et al., Phys. Plasmas **16**, 060702 (2009).

[199] F. Jenko, T. Dannert, and C. Angioni, Plasma Phys. Contr. F. **47**, B195 (2005).

[200] C. Angioni, A. Peeters, G. Pereverzev, et al., Nucl. Fusion **49**, 055013 (2009).

[201] T. Fülöp and S. Moradi, Phys. Plasmas **18**, 030703 (2011).

[202] C. Angioni, private communication (2010).

[203] C. Bourdelle, X. Garbet, F. Imbeaux, et al., Phys. Plasmas **14**, 112501 (2007).

[204] E. Fable, C. Angioni, and O. Sauter, Plasma Phys. Contr. F. **52**, 015007 (2010).

[205] C. Wahlberg, Phys. Rev. Lett. **101**, 115003 (2008).

[206] F. Merz and F. Jenko, Nucl. Fusion **50**, 054005 (2010).

[207] N. J. Conway, P. G. Carolan, J. McCone, et al., Rev. Sci. Instr. **77**, 10F131 (2006).

[208] M. Barnes, I. G. Abel, W. Dorland, et al., Phys. Plasmas **17**, 056109 (2010).

[209] M. Barnes, PhD in physics, University of Maryland (2008).

[210] P. H. Diamond and Y.-B. Kim, Phys. Fluids B-Plasma **3**, 1626 (1991).

[211] J. D. Huba, *NRL plasma formulary* (Naval Research Lab., Washington DC, 2007).

Appendix A

Vector Identities

Taken from Ref. [211], relisted here for reference.

$$\begin{aligned}
\mathbf{A}\times(\mathbf{B}\times\mathbf{C}) &= (\mathbf{A}\cdot\mathbf{C})\mathbf{B}-(\mathbf{A}\cdot\mathbf{B})\mathbf{C} && \text{(A.1)}\\
\nabla\times(\mathbf{A}\times\mathbf{B}) &= \mathbf{A}(\nabla\cdot\mathbf{B})-\mathbf{B}(\nabla\cdot\mathbf{A})+(\mathbf{B}\cdot\nabla)\mathbf{A}-(\mathbf{A}\cdot\nabla)\mathbf{B} && \text{(A.2)}\\
\nabla(\mathbf{A}\cdot\mathbf{B}) &= \mathbf{A}\times(\nabla\times\mathbf{B})+\mathbf{B}\times(\nabla\times\mathbf{A})+(\mathbf{A}\cdot\nabla)\mathbf{B}+(\mathbf{B}\cdot\nabla)\mathbf{A} && \text{(A.3)}
\end{aligned}$$

Abbreviations and symbols

A list commonly used abbreviations and mathematical symbols is provided here; most of these are also defined in the text.

Acronym	Long Form	Description
GKW	Gyrokinetics at Warwick	A gyrokinetic computer code
GYRO	Unknown	A gyrokinetic computer code
GENE	Unknown	A gyrokinetic computer code
GS2	Unknown	A gyrokinetic computer code
MHD	Magnetohydrodynamics	Set of plasma equations
FLR	Finite (nonzero) Larmor radius	
TEM	Trapped electron mode	Drift wave plasma instability
ITG	Ion temperature gradient (mode)	Drift wave plasma instability
ITER	No longer considered an acronym (see footnote on page 1)	Future tokamak experiment
GA-STD	Label for set of simulation parameters	Defined in Chapter 4
GKW-ITG	Label for set of simulation parameters	Defined in Chapter 6
GKW-TEM	Label for set of simulation parameters	Defined in Chapter 6
PURE-TEM	Label for set of simulation parameters	Defined in Chapter 5
Fig.	Figure	
Eq.	Equation	
Ref.	Reference	
Sec.	Section	
A.U.	Arbitrary Units	
Mag.	Magnetic	

For species quantities a subscript e or i indicates electrons or ions respectively. Many results are presented in the standard gyro-Bohm units where a is the plasma outer minor radius, $c_s = \sqrt{T_e/m_i} = \sqrt{2}v_{th,i}$ is the ion sound speed, $\rho_s = c_s/\omega_{ci}$ is the ion-sound Larmor radius, and $\omega_{ci} = eB/m_i$ is the ion cyclotron frequency evaluated on the magnetic axis. Where used, $\rho_i = \sqrt{2}\rho_s$. Vector quantities resolved into parallel and perpendicular components with respect to magnetic field are denoted with $\|$ and $\perp$ subscripts respectively.

Symbol	Description	Notes
T	Temperature in units of energy	$T = k_B T_K$
k_B	Boltzmann's constant	$1.38 \times 10^{-23} m^2$ kg $s^{-2} K^{-1}$
ϵ_0	Electric permittivity of free space	$8.85 \times 10^{-12} m^{-3}$ kg^{-1} $s^4 A^2$
μ_0	Magnetic permeability of free space	$1.26 \times 10^{-6} m$ kg $s^{-2} A^{-2}$
v_{th}	Thermal velocity	$v_{\text{th}} = \sqrt{2T/m}$
μ	Magnetic moment, adiabatic invariant	$\mu = mv_\perp^2/2B$
e	Charge of an electron (magnitude)	$1.60 \times 10^{-19} C$
Z	Species charge in units of e	
R_A	Major radius of magnetic axis	
R_0	Major radius at which n_{R_0} is defined	Can be $R_0 = R_{\text{axis}}$ or $R_0 = R_{\text{LFS}}$
r	Minor radius of local flux surface	Label for circular flux surfaces
a	Minor radius of last closed flux surface	
ϵ	Inverse aspect ratio	$\epsilon = r/R_A$
m	Species mass	
$\tilde{n}$	Perturbed density	Time dependant
$\bar{n}$	Perturbed density amplitude	Chapter 1 only
n_0, n	Background density	Function of θ when $u \sim 1$.
n_{R_0}	Background density at R_0	
N	Total density (Chapter 1 only)	
$\mathbf{B}$	Magnetic field vector	
$\mathbf{E}$	Electric field vector	
$\mathbf{J}$	Current density vector	
β	Ratio of kinetic to magnetic pressure	$\beta = \frac{p_{\text{central}}}{B^2_{\text{edge}}/2\mu_0}$
θ	Poloidal angle coordinate	Zero at low field side, $\mathbf{e}_\theta \times \mathbf{e}_\varphi = \mathbf{e}_\psi$
θ_0	Poloidal angle of mode maximum	
$\tilde{\phi}, \phi$	Perturbed electrostatic potential	
Φ, $\bar{\Phi}$	Background electrostatic potential	
	Continued overleaf...	

Symbol	Description	Notes
φ	Toroidal angle coordinate	Clockwise from above
ψ	Dimensionless radial coordinate	Generalised flux surface label, $\perp$
s	Dimensionless parallel coordinate	$\mathbf{b}\cdot\nabla = \partial/\partial s$
ζ	Dimensionless binormal coordinate	Axisymmetric, perpendicular
s_{B}	Direction of toroidal field ± 1	Relative to $\nabla\varphi$
s_{j}	Direction of plasma current ± 1	Relative to $\nabla\varphi$
$\mathbf{x}$	Particle position vector	
$\mathbf{X}$	Gyrocentre position vector	
$\mathbf{k}$	Perturbation wavevector	
k_θ	Poloidal component of wavevector	Evaluated at low field side
t	Time	
$\alpha, \alpha_{\theta,s,r,x,vp}$	Numerical hyperdissipation coeffcients	
α_E	Shear quench parameter	
ω	Mode frequency (angular)	
ω_c	Gyrofrequency (cyclotron frequency)	$\omega_c = eB/m$
ω_φ	Plasma rotation frequency (angular)	
Ω	Frame rotation frequency (angular)	
u	Mach number of bulk ions	$u = R_A\Omega/v_{th,i}$
γ	Mode growth rate	
$\gamma_E,\ (\omega_s)$	Shearing rate, (in simplified problem)	$\gamma_E \approx \frac{dv_s}{dr}$
$\mathcal{E},\ (\mathcal{E}_R)$	Centrifugal energy, (normalised)	$\mathcal{E}(\theta) = Ze\Phi - \frac{1}{2}m\Omega^2(R^2 - R_0^2)$
ρ	Gyroradius (Larmor radius)	$\rho = v_{th}/\omega_c$ with ω_c at R_A
ρ_*	Small expansion parameter	$\rho_* = \rho_i/R_A$
ρ_s	Ion sound Larmor radius	$\rho_s = c_s/\omega_{ci}$ with ω_c at R_A
c_s	Ion sound speed	$c_s = \sqrt{T_e/m_i} = \sqrt{2}v_{th,i}$
$\mathbf{v}_D$	Any or all perpendicular drifts	
$\mathbf{v}_E$	$E\times B$ drift	$\mathbf{v}_E = \frac{\mathbf{b}\times\nabla\phi}{B}$
$\mathbf{v}_d, \mathbf{v}_i$	Curvature drifts, Inertial drifts	
$\mathcal{O}(\rho_*)$	Terms of order $\sim \rho_*$	
Q_s	Heat flux of species s	
Γ_s	Particle flux of species s	
χ_s	Thermal diffusivity of species s	$\chi_s = \frac{Q_s}{n\lvert\nabla T_s\rvert}$
D_s	Particle diffusivity of species s	$D_s = \frac{\Gamma_s}{\lvert\nabla n_s\rvert}$
$\Gamma_\parallel$	Ion parallel momentum flux	$\Gamma_\parallel \approx \Gamma_\varphi \approx \Pi_\varphi/R_A$
Π_φ	Toroidal angular momentum flux	